Title: Recruitment of bifunctional regulator thermospermine to methylated ribosomes directs xylem fate

Authors: Donghwi Ko[1,3]†, Raili Ruonala[1,2,3,]†, Alexandre Faille[4]†*, Eva Hellmann[3,5]†, Hanna Help[1], Huili Liu[10], Ronni Nielsen[6], Anders Haakonsson[6]‡, Nuria De Diego[18], Anja Paatero[2], Mariia V. Shcherbii[2], Karolina Stefanowicz[9], Sanja Ćavar Zeljković[18], Tine Drud Lundager Rasmussen[6], Ondrej Novak[12], Zsuzsanna Bodi[13], Gugan Eswaran[1, 2]§, Brecht Wybouw[1,2], Matthieu Bourdon[3]¶, Cristina Urbez[14], Xiaonan Liu[2], Kari Salokas[2], Tiina Öhman[2], Tanya Waldie[3], Petri Törönen[2], Sedeer el-Showk[1], Martin Balcerowicz[19], Fabrice Besnard[15], Xiaomin Liu[3], Patrick Perkins[16], Serina Mazzoni-Putman[17], Julia P. Vainonen[1], Maija Sierla[1], Mikko J. Frilander[2], Susanne Mandrup[6], Teva Vernoux[15], Karin Ljung[11], Alejandro Ferrando[14], Miguel A. Blazquez[14], Liisa Holm[1, 2], Rupert Fray[13], Markku Varjosalo[2], Ottoline Leyser[3]#, Ville O. Paavilainen[2], Ari Pekka Mähönen[1,2], Anna Stepanova[17], Jose Alonso[17], Steffen Heber[16], Robert Malinowski[9], Finn Kirpekar[6]*, Alan J. Warren[4,7,8]*, Ykä Helariutta[1,2,3,20]*

Affiliations:

[1] Organismal and Evolutionary Biology Research Programme, Faculty of Biological and Environmental Sciences, University of Helsinki; 00790 Helsinki, Finland

[2] Institute of Biotechnology, HiLIFE, University of Helsinki; 00790 Helsinki, Finland

[3] The Sainsbury Laboratory, University of Cambridge; Cambridge, CB2 1LR, United Kingdom

[4] Cambridge Institute for Medical Research, Cambridge; CB2 0XY United Kingdom

[5] Department of Geography, University of Cambridge; CB2 3EN, Cambridge, United Kingdom

[6] Department of Biochemistry and Molecular Biology, University of Southern Denmark; 5230 Odense, Denmark

[7]Department of Haematology, University of Cambridge, Cambridge, United Kingdom

[8] Stem Cell Institute, University of Cambridge, Cambridge, CB2 0AW, United Kingdom

[9] Department of Integrative Plant Biology, Institute of Plant Genetics of the Polish Academy of Sciences; 60-479 Poznań, Poland

[10]College of Life Sciences, South China Agricultural University, Guangzhou, 510642, China

[11] Department of Forest Genetics and Plant Physiology, Umeå Plant Science Centre, Swedish University of Agricultural Sciences; 901 83 Umeå, Sweden

[12]Laboratory of Growth Regulators, Institute of Experimental Botany, Czech Academy of Sciences and Faculty of Science, Palacký University, Slechtitelu 27, CZ-77900 Olomouc, Czech Republic

[13] Plant Sciences Division, University of Nottingham; Sutton Bonington, LE12 5RD, United Kingdom

[14] Instituto de Biología Molecular y Celular de Plantas, Consejo Superior de Investigaciones Científicas-Universitatd Politè cnica de València; 46022 Valencia, Spain

[15] Laboratoire Reproduction et Développement des Plantes, Univ Lyon, ENS de Lyon, CNRS, INRAE; 69342 Lyon, France

[16] Department of Computer Science, North Carolina State University; Raleigh, NC 27695, USA

[17] Department of Plant and Microbial Biology, North Carolina State University; Raleigh, NC 27695, USA

[18] Czech Advanced Technology and Research Institute (CATRIN), Palacký University Olomouc; Olomouc, Czech Republic.

[19] Division of Plant Sciences, University of Dundee; Dundee, DD2 5DA, United Kingdom

[20] Institute of Bioengineering, University of Tartu; Nooruse 1, Tartu 50411, Estonia

*Corresponding authors. Email: yrjo.helariutta@helsinki.fi, ajw1000@cam.ac.uk, f.kir@bmb.sdu.dk, raf58@cam.ac.uk

‡ Present address: Odense University Hospital, Denmark

§ Present address: Head of R&D, DeepScan Diagnostics Oy, Helsinki, Finland

¶ Present address: Friedrich Miescher Institute for Biomedical Research, Basel, Switzerland

Present address: Department of Plant Sciences, University of Cambridge, Downing Street, Cambridge, CB2 3EA

Abstract:

Polyamines are often associated with ribosomes and thought to stabilize their integrity. In *Arabidopsis*, the polyamine thermospermine affects xylem cell fate. Thermospermine induces translation of SUPPRESSOR-OF-ACAULIS51 (SAC51) and SAC51-LIKEs (SACLs), which inhibit heterodimerization of xylem development proteins, LONESOME-HIGHWAY (LHW) and TARGET-OF-MONOPTEROS5. Here, we report a methyltransferase, OVERACHIEVER, that methylates the peptidyl transferase center of the 25S rRNA. Residue m^3U2952 promotes functional thermospermine binding to a specific site connecting the P-site tRNA with rRNA residues in the peptidyl transferase center. This interaction enhances translation of SACLs but inhibits that of LHW. Our study uncovers the dependency between a conserved rRNA base methylation and a polyamine in orchestrating cell fate decisions, highlighting a role for the ribosome chemical landscape in translational regulation.

Main Text

Introduction

The intricate chemical landscape of the ribosome has been brought into focus at a structurally high resolution (*1–8*). Typically, rRNA modifications such as pseudouridylation, 2'-*O*-ribose methylation and various base modifications exhibit heterogeneity and dynamic behavior, suggesting that these alterations have specific, context-dependent roles (*9*). Another critical factor shaping the chemical landscape of ribosomes is the presence of ribosome-associated small

molecules. Antibiotics, amino acids, and sucrose bind to the peptidyl transferase center or nascent polypeptide exit tunnel and regulate translation of specific mRNAs by interacting with their nascent peptides (*10–12*). Up to 15% of cellular polyamines such as spermidine, cadaverine or putrescine, are associated with ribosomes, from humans to bacteria (*13–18*), mediated at least in part via binding to the rRNA (*19*). However, no specific cellular functions have yet been attributed to ribosome-bound polyamines despite their roles in diverse biological processes, including the regulation of cell proliferation, differentiation, autophagy, and aging (*20*, *21*).

OVAC writes m^{3}U2952 in the 25S rRNA

In an ethyl methanesulfonate screen for factors involved in vascular development in *Arabidopsis thaliana* (fig. S1 and supplementary text), we isolated the *overachiever* (*ovac-1*) mutant. *ovac-1* carries a nonsense mutation in the gene *At5g19300* and exhibits an increased number of secondary xylem vessels at the expense of procambial and parenchyma cells, starting from the onset of secondary development (6 days after sowing) throughout all subsequent stages examined (Fig. 1, A to D, Fig. 4A, fig. S22, A and B). The cause of the OVAC phenotype was confirmed by a second allele, the T-DNA insertion mutant *ovac-2*. *ovac* plants are stunted and more branched, but they show no other obvious morphological differences (Fig. 1E).

Homology modeling of the OVAC protein sequence suggested that it is structurally homologous to the bacterial rRNA m^{3}U methyltransferase yggj_haein (Protein Data Bank ID, 1nxz), a member of the SPOUT superfamily of methyltransferases (*22*, *23*). Therefore, we investigated whether OVAC is involved in rRNA m^{3}U modification in *Arabidopsis*. The OVAC protein localizes to the nucleus in root tips and leaves, preferentially in the nucleolus (fig. S2, A and B), consistent with proteomics analysis of *Arabidopsis* cell culture (*24*) and suggesting that OVAC may target rRNA. To test this, we designed an RNA-sequencing (RNA-seq)-based method to search primarily for m^{3}U harboring residues in rRNA that would be absent in *ovac*. We identified U2952 in the peptidyl transferase center of 25S rRNA, which had a decreased read count only in wild type (fig. S2D). Based on RNA modification databases and publications (*25–28*), the equivalent rRNA site in human, fruit fly, tomato, tobacco and in the Archaea *Haloarcula marismortui* harbors an m^{3}U residue (Data S1). Mass spectrometry analysis using MALDI MS and tandem MS of *Arabidopsis* 25S rRNA (Fig. 1, F and G, fig. S2, E and F), and primer extension mapping (fig. S3, A and B) confirmed that this uridine is indeed methylated (and thus protected from RNase A cleavage in wild type), although a small fraction of non-methylated fragments was

also detected in the wild-type total cellular RNA (Fig. 1, F and G, fig. S2, E and F, and Data S2). In *ovac*, there was no trace of m^3U2952 (leaving the site sensitive to RNase A cleavage), while modifications to the neighboring residues were 100% complete and identical to wild type (Fig. 1, F and G, fig. S2E, S3B, and Data S2). The relative intensity of the m/z 1625.2 (RNase T1-digestion product harboring m^3U2952) was approximately five times higher compared to the m/z 1611.2 (U2952) (fig. S2, E and F), indicating that in wild type, the U2952 position is at least 80% methylated in various tissues (Fig. 1, F and G, fig. S2, E and F).

Introducing point mutations that substitute the conserved residues R127 and T310 in the OVAC methyltransferase domain with alanine did not compromise its protein expression but abolished methyltransferase activity in *Arabidopsis* (fig. S4, A and B). Consequently, expression of the mutated OVAC (mOVAC) failed to rescue the vascular and shoot developmental defects observed in the *ovac* mutant (fig. S4, C to E). In vitro analyses (*29*, *30*) identified the bacterially produced recombinant *Arabidopsis* OVAC protein and the methyl group donor *S*-adenosyl methionine (SAM) as the minimal components required for the methylation of the U2952 residue of a synthetic rRNA transcript (Fig. 1, H and I). Taking these data together, we conclude that OVAC is an rRNA methyltransferase responsible for the m^3U2952 base modification specifically in the peptidyl transferase center of 25S rRNA in *Arabidopsis*.

m^3U2952 enhances bifunctional translational regulation by thermospermine

Next, we addressed the role of m^3U2952 in *Arabidopsis*. In eukaryotic ribosomes, the 25S or 28S rRNAs are central components of 60S subunits. The relatively healthy phenotype of the *ovac* mutant is distinct among the many growth-impaired or embryonic-lethal mutants for ribosomal functions (*31–33*) (Fig. 1E). Given that it is a mutation in a single-copy gene, we speculated that OVAC may have a specific regulatory role rather than a housekeeping function.

To understand how OVAC-mediated rRNA methylation affects ribosome function, we analyzed translation efficiency by performing ribosome footprinting and transcriptome analyses on wild-type and *ovac* roots (*34*) (fig. S5 and Materials and Methods). Genome wide analysis of ribosomal occupancy on mRNA species revealed 99.84% of transcripts were translated in a similar way between wild type and *ovac*, indicating a similar overall translation efficiency between wild type and *ovac* (fig. S6A). Consistent with this, mass spectrometry analysis of polysome fraction identified only four proteins enriched in the *ovac* mutant relative to wild type, none of them ribosomal (Data S3), indicating that *ovac* does not have a major effect on the ribosomal protein

components. The *ovac* mutation impacted the translation of only a small subset of transcripts: 15 nuclear genes were significantly translationally upregulated, while another 15 genes were downregulated in an edgeR analysis (fig S6, A to C, and Data S4). Among these 30 genes, we prioritized those with known functions in vessel formation to account for the xylem differentiation phenotype observed in *ovac* mutants (Fig. 1, C and D). Based on this criterion, we first focused on *SACL3* (Fig. 2A, fig S6, B and C, and Data S4).

SACL3 together with its paralogs SACL1, SACL2, and SAC51 (SACLs) inhibit vessel differentiation by competing with TARGET-OF-MONOPTEROS5 for interaction with LHW (*35–37*). The plant-specific polyamine, thermospermine, generated by ACAULIS5 (ACL5) promotes translation of *SACL*s by alleviating repression from conserved upstream open reading frames (uORFs), but how thermospermine mediates this translational control remains elusive (*36–40*). Consequently, we conducted ribosome footprinting and transcriptome analysis with and without thermospermine treatment to explore the genome-wide translational effects of thermospermine and m^3U2952 in *Arabidopsis* roots (fig. S6 and Data S4 to S7). In the wild type, 222 genes were significantly regulated at the translational level by thermospermine (fig. S6, B and D, and Data S5). Among these, we identified 6 uORF-containing transcripts whose translation efficiency was enhanced and 20 where it was inhibited in response to thermospermine in the wild type but not in *ovac* (Data S8). Among these genes, translation of *SAC51*, *SACL2*, and *SACL3* was upregulated (fig. S6, B to F). We also observed that the translation of *LHW* was downregulated in the wild type by thermospermine (Fig. 2A, fig. S6, B to F, Data S5 and S8). We validated these expression profiles using reporter genes (supplementary text and Fig. 2, B to E, and fig. S7).

We next carried out a detailed analysis of ribosome occupancy along the *SAC51, SACL3, SACL2,* and *LHW* mRNAs. This analysis suggested that the OVAC-dependent rRNA methylation is required for thermospermine-dependent release of ribosome stalling at the uORFs of *SACL*s and induction of ribosome stalling at the uORF of *LHW*, respectively (fig. S8, S9 and S10). The ribosome stalling uORFs are conserved within each group but not between the SACLs and LHW (fig. S11A). We further observed that the *ovac* mutant phenotypes can be rescued by genetic mutations in the *SACL* uORFs or in the genes encoding *LHW* or *LARGE SUBUNIT RIBOSOMAL PROTEIN 4* (*RPL4*), which suppress *acl5* mutant phenotypes (*36*, *41*) (supplementary text and fig. S11, A to I). By swapping the uORFs between SAC51 and LHW 5' leaders, we determined that the uORFs were sufficient for the positive or negative effect conferred by the bifunctional thermospermine (fig. S12). Taken together, we conclude that thermospermine requires the OVAC-

mediated m^3U2952 modification to exert its bifunctional uORF-dependent translational regulation – promoting *SACL*s translation while inhibiting that of *LHW*.

Thermospermine connects P-site tRNA with rRNA residues in the peptidyl transferase center

We hypothesized that residue m^3U2952 might directly interact with thermospermine on the ribosome to modulate translation. We purified actively translating ribosomes (Materials and Methods) and determined their structure using cryo-electron microscopy (cryo-EM). By high-resolution visualization of ribosomes (*8*), we first generated a 1.82 Å map of the wild-type *Arabidopsis* 80S ribosome carrying a bound P-site tRNA in the absence of thermospermine supplementation (tSpm-) (fig. S13A and Data S9). Although we could readily model water molecules and ions, we identified only a single thermospermine molecule, more than 50 Å from m^3U2952 (fig. S14, A and D).

We next generated a 2.2 Å map of purified wild-type *Arabidopsis* 80S ribosomes pre-incubated with 100 μM thermospermine (tSpm+) for 10 min at 25 °C prior to cryo-EM grid preparation (Fig. 3, A and B, and fig. S13B), identifying 26 additional putative thermospermine binding sites compared to the tSpm- particles, 20 in the 60S subunit and 6 in the 40S subunit body (fig. S14A). The thermospermine molecules were all stabilized by electrostatic and hydrogen bonding interactions with the rRNA, mostly involving phosphate groups and water (fig. S14, B to D). We identified one thermospermine molecule in the peptidyl transferase center, in a groove between the entrance to the nascent polypeptide exit tunnel and the CCA-end of the P-site tRNA (Fig. 3, C and D and fig. S14A-molecule '*'). Like the thermospermine molecules identified elsewhere in the ribosome, this thermospermine molecule replaced water molecules observed in the tSpm- particles (fig. S15A) and made electrostatic interactions with the phosphate groups of rRNA residues C2403, C2404, A2807, U2953 (which is directly linked to m^3U2952) and A2969 (Fig. 3, C and D). To the best of our knowledge, this binding site has not been reported for any ligand other than water molecules. Thermospermine binding therefore bridges the P-site tRNA with the OVAC substrate m^3U2952 in the peptidyl transferase center by interacting with the phosphate groups of residues C75 and A76 at the CCA-end of the bound P-site tRNA (Fig. 3, C and D).

m^3U2952 promotes functional binding of thermospermine to ribosome

We resolved the structure of 80S ribosomes purified from *ovac* mutant plants (+/- tSpm) at a resolution of 2.2 Å (fig. S13, C and D). Compared to wild-type tSpm+ ribosomes, all the thermospermine molecules in the *ovac* mutant tSpm+ particles were bound in an identical manner, apart from the thermospermine located in the peptidyl transferase center which adopted a distinct binding mode in which the interaction between the primary amine of thermospermine and the phosphate group of residue m^3U2952 was disrupted (Fig. 3, E to H). The signal for thermospermine in this map was also less clearly defined, likely due to the altered hydrogen-bonding network with the net loss of two hydrogen bonds. Overall, this suggests that thermospermine binds more weakly to *ovac* ribosomes compared to wild-type ribosomes.

We identified additional structural differences in the peptidyl transferase center of wild-type compared to *ovac* mutant ribosomes (both tSpm+ and tSpm-). In the *ovac* ribosomes, a hydrogen bond was established between the N3 atom of residue U2952 and a potassium ion-coordinated water molecule, altering the position of the base of U2952 due to the loss of its 3'-methyl modification with an associated rotation of the base of U2953 at the entrance to the polypeptide exit tunnel (fig. S15, B and C). In addition, the conformation of the phosphate group linking C75 to the ribose moiety of A76 in the P-site tRNA differed between wild-type and *ovac* mutant ribosomes (fig. S15D). These structural data indicate that the OVAC-dependent U2952 base methylation functionalizes thermospermine binding. To estimate the dependence of thermospermine binding efficiency on m^3U2952, we determined the half maximal effective concentration (EC_{50}) for *SAC51* translation (fig. S16), and the half maximal inhibitory concentration (IC_{50}) for *LHW* translation and vessel differentiation (fig. S17). The *ovac* mutant exhibited a 16.5-fold increase in the EC_{50} for *SAC51* translation (fig. S16C), a 12.5-fold increase in the IC_{50} for *LHW* translation and a 16.8-fold increase in the IC_{50} for vessel differentiation (fig. S17, C and D). The data further indicate that the cooperative interaction between thermospermine and OVAC-dependent methylation in regulating *SACL* and *LHW* mRNA translation is mediated by a direct molecular interaction between thermospermine and the methylated base m^3U2952 in the peptidyl transferase center.

Thermospermine binding to the methylated ribosome switches cell fates

To understand the impact of context-dependent modulation of thermospermine binding to ribosomes on xylem development, we first analyzed endogenous levels of thermospermine in wild type and *ovac* plants and then pharmacologically modified thermospermine levels. Consistent with

the idea of homeostatic control in hormonal circuits (*42*), we found a significantly higher thermospermine content in *ovac* compared to wild type, along with elevated transcript abundance of the thermospermine biosynthesis gene *ACL5* (fig. S18, A and B). This aligns with the higher IC_{50} and increased resistance to thermospermine-induced inhibition of vessel differentiation in *ovac* compared to wild type (fig. S16, S17, and S18, C to E), indicating that methylation-dependent binding of thermospermine to the ribosome is the principal mode of action for thermospermine in inhibiting vessel differentiation during xylem development.

On the other hand, treatment with the thermospermine biosynthesis inhibitor xylemin (*43*), resulted in an additive *ovac* phenotype, with a 4.4-fold increase in the number of xylem vessels per cross-section area compared to similarly treated wild type (Fig 4, A and B, and supplementary text). By comparing the extent of xylem differentiation between *ovac* and wild type on the one hand, and between *ovac*, xylemin-treated *ovac,* and methyltransferase inactive OVAC (mOVAC) on the other, we observed that, in the absence of the methylation, thermospermine can still exert residual xylem inhibitory activity albeit at a low level (Fig 4, A and B, and fig. S4, C and D). We interpret this supports the concept of methylation-dependent functional binding of thermospermine.

Analogous to the enhanced thermospermine levels in *ovac*, the thermospermine-deficient mutant *acl5* showed increased *OVAC* transcript and m^3U2952 levels compared to wild type (fig. S18, F to H). Because the *acl5* phenotype is weaker than that of the xylemin-treated *ovac* (Fig. 4, A and B) and *SAC51* translation in *acl5* still occurs but is reduced (*38*), it seems plausible that m^3U2952 itself may contribute to *SACL* and *LHW* translation that suppresses vessel differentiation, possibly via structural alterations in the peptidyl transferase center (Fig. 3H and fig. S15, B to D). Consistently, loss of the m^3U modification in animals results in defects in translation and lethality (*30*, *44*)

Finally, to examine vessel differentiation phenotypes in the context of our ribosome footprinting data, we examined the expression of various fluorescent translational reporters during secondary root development. Thermospermine-dependent *SAC51* translation was reduced below detection level in xylemin-treated *ovac* (Fig. 4C, fig. S19, A to D, and supplementary text). Conversely, the steady-state translation levels of *LHW* were increased in *ovac* and *acl5* compared to wild type, while xylemin treatment further increased *LHW* translation efficiency in *ovac* and in the wild type (Fig 4D, fig. S20, A to I, and supplementary text). In both cases, the decreased *SAC51* and enhanced *LHW* translation levels are in line with the extreme xylem vessel differentiation

phenotypes, in which almost all procambial cells differentiated as xylem vessel (Fig 4, A and B, and supplementary text). To investigate the impact of elevated *LHW* translation on xylem differentiation, an *lhw* mutation (*36*) was introduced into the *ovac* background. It partially but significantly rescued excessive xylem vessel differentiation induced by xylemin (fig. S21). Furthermore, expression of *LHW* without its uORF enhanced the *ovac* phenotype to a level similar to *acl5* (fig. S22, C to E, and supplementary text), highlighting the need for *LHW* downregulation (identified here), in addition to *SACL* upregulation (*36*, *37*, *45*) to inhibit vessel differentiation. Together, these findings demonstrate that optimal bifunctional regulation of *SACL* and *LHW* translation depends on functional binding of thermospermine to the OVAC-methylated ribosome (Fig. 4E).

Discussion

In microorganisms, cooperative interactions between the peptidyl transferase center, the nascent peptide and the exit tunnel wall can regulate the translational activity of the ribosome by leveraging arrest peptides that cause the ribosomes that translate them to stall in response to specific metabolites (*12*). Supporting such a role for thermospermine, the effect of the *ovac* mutation on translational regulation can be suppressed by a missense mutation in the RPL4 “tentacle” domain that reaches into the exit tunnel wall constriction region (*41*) (fig. S11, B, G and H). Similarly, RPL4 mutations can release the translational arrest caused by ribosomal stalling in several other regulatory peptide sequences (*41*). However, the m^3U2952-associated thermospermine binding site identified here in *Arabidopsis* is distinct from those of other well-characterized peptidyl transferase center-binding molecules, that typically block translation by competing with tRNA or sensing arrest peptides within the exit tunnel (*12*). Thermospermine binds to a position adjacent to these sites that bridges rRNA residues with tRNA, suggesting a distinct (potentially allosteric) mode of action based on structural determinants characteristic for thermospermine activity (*46*).

Given that even in wild-type plants, approximately 20% of rRNAs remain unmethylated at U2952 (fig. S2, D and E), and that thermospermine production is tightly regulated and spatially restricted (*35*, *47*, *48*), it is possible that plants fine-tune the translational regulation of *SACL*s and *LHW* by integrating methylation status and thermospermine distribution. In this scenario, it is possible that the heterogeneity is cell-dependent, such that some cell types may be immune to thermospermine. Understanding how these regulatory dynamics influence differential cell fate decisions - whether in enhancing resilience to abiotic stresses (*49*) or in toggling between the fleshy

xylem tissues of edible storage organs and the woody growth characteristic of trees during xylem development - represents an important direction for future research.

References

1. S. K. Natchiar, A. G. Myasnikov, H. Kratzat, I. Hazemann, B. P. Klaholz, Visualization of chemical modifications in the human 80S ribosome structure. *Nature* **551**, 472–477 (2017).
2. M. Taoka, Y. Nobe, Y. Yamaki, Y. Yamauchi, H. Ishikawa, N. Takahashi, H. Nakayama, T. Isobe, The complete chemical structure of Saccharomyces cerevisiae rRNA: partial pseudouridylation of U2345 in 25S rRNA by snoRNA snR9. *Nucleic Acids Res* **44**, 8951 (2016).
3. P. V Sergiev, N. A. Aleksashin, A. A. Chugunova, Y. S. Polikanov, O. A. Dontsova, Structural and evolutionary insights into ribosomal RNA methylation. *Nat Chem Biol* **14**, 226–235 (2018).
4. V. Stojković, A. G. Myasnikov, I. D. Young, A. Frost, J. S. Fraser, D. G. Fujimori, Assessment of the nucleotide modifications in the high-resolution cryo-electron microscopy structure of the Escherichia coli 50S subunit. *Nucleic Acids Res* **48**, 2723–2732 (2020).
5. N. R. Genuth, M. Barna, The Discovery of Ribosome Heterogeneity and Its Implications for Gene Regulation and Organismal Life. *Mol Cell* **71**, 364–374 (2018).
6. Z. Shi, K. Fujii, K. M. Kovary, N. R. Genuth, H. L. Rö St, M. N. Teruel, M. B. Correspondence, Heterogeneous Ribosomes Preferentially Translate Distinct Subpools of mRNAs Genome-wide. *Mol Cell* **67**, 71–83 (2017).
7. W. Li, F. R. Ward, K. F. McClure, S. T. L. Chang, E. Montabana, S. Liras, R. G. Dullea, J. H. D. Cate, Structural basis for selective stalling of human ribosome nascent chain complexes by a drug-like molecule. *Nat Struct Mol Biol* **26**, 501–509 (2019).
8. A. Faille, K. C. Dent, S. Pellegrino, P. Jaako, A. J. Warren, The chemical landscape of the human ribosome at 1.67 Å resolution. *bioRxiv*, 2023.02.28.530191 (2023).
9. I. Milenkovic, E. M. Novoa, Dynamic rRNA modifications as a source of ribosome heterogeneity. *Trends Cell Biol*, doi: 10.1016/J.TCB.2024.10.001 (2024).
10. A. Herrero del Valle, B. Seip, I. Cervera-Marzal, G. Sacheau, A. C. Seefeldt, C. A. Innis, Ornithine capture by a translating ribosome controls bacterial polyamine synthesis. *Nat Microbiol* **5**, 554–561 (2020).
11. S. van der Horst, R. Englmeier, J. Hanson, S. Smeekens, F. Förster, Sucrose-mediated translational stalling involves a conserved ribosomal pocket. *bioRxiv*, 2023.08.27.554957 (2023).
12. A. Bhattacharya, T. T. Renault, C. Axel Innis, The ribosome as a small-molecule sensor. *Curr Opin Microbiol* **77**, 102418 (2024).
13. S. S. COHEN, J. LICHTENSTEIN, Polyamines and ribosome structure. *J Biol Chem* **235**, 2112–2116 (1960).
14. S. Holvec, C. Barchet, A. Lechner, L. Fréchin, S. N. T. De Silva, I. Hazemann, P. Wolff, O. von Loeffelholz, B. P. Klaholz, The structure of the human 80S ribosome at 1.9 Å resolution reveals the molecular role of chemical modifications and ions in RNA. *Nature Structural & Molecular Biology 2024 31:8* **31**, 1251–1264 (2024).
15. M. Holm, S. K. Natchiar, E. J. Rundlet, A. G. Myasnikov, Z. L. Watson, R. B. Altman, H. Y. Wang, J. Taunton, S. C. Blanchard, mRNA decoding in human is kinetically and structurally distinct from bacteria. *Nature 2023 617:7959* **617**, 200–207 (2023).
16. J. Noeske, M. R. Wasserman, D. S. Terry, R. B. Altman, S. C. Blanchard, J. H. D. Cate, High-resolution structure of the Escherichia coli ribosome. *Nature Structural & Molecular Biology 2015 22:4* **22**, 336–341 (2015).
17. Z. L. Watson, F. R. Ward, R. Méheust, O. Ad, A. Schepartz, J. F. Banfield, J. H. D. Cate, Structure of the bacterial ribosome at 2 Å resolution. *Elife* **9**, 1–62 (2020).
18. F. Wiechert, A. Unbehaun, T. Sprink, H. Seibel, J. Bürger, J. Loerke, T. Mielke, C. A. Diebolder, M. Schacherl, C. M. T. Spahn, Visualizing the modification landscape of the human 60S ribosomal subunit at close to atomic resolution. *Nucleic Acids Res* **53** (2025).
19. H. L. Lightfoot, J. Hall, Endogenous polyamine function--the RNA perspective. *Nucleic Acids Res* **42**, 11275–11290 (2014).
20. K. Igarashi, K. Kashiwagi, Functional roles of polyamines and their metabolite acrolein in eukaryotic cells. *Amino Acids* **53**, 1473–1492 (2021).
21. T. M. Stewart, C. E. Holbert, Jr. Robert A. Casero, Helping the helpers: polyamines help maintain helper T-cell lineage fidelity. *Immunometabolism (Cobham (Surrey, England)* **4**, e00002 (2022).

22. K. L. Tkaczuk, S. Dunin-Horkawicz, E. Purta, J. M. Bujnicki, Structural and evolutionary bioinformatics of the SPOUT superfamily of methyltransferases. *BMC Bioinformatics* **8**, 73 (2007).
23. G. N. Basturea, K. E. Rudd, M. P. Deutscher, Identification and characterization of RsmE, the founding member of a new RNA base methyltransferase family. *RNA* **12**, 426 (2006).
24. D. Palm, S. Simm, K. Darm, B. L. Weis, M. Ruprecht, E. Schleiff, C. Scharf, Proteome distribution between nucleoplasm and nucleolus and its relation to ribosome biogenesis in *Arabidopsis thaliana*. *RNA Biol* **13**, 441–454 (2016).
25. S. Dunin-Horkawicz, A. Czerwoniec, M. J. Gajda, M. Feder, H. Grosjean, J. M. Bujnicki, MODOMICS: a database of RNA modification pathways. *Nucleic Acids Res* **34** (2006).
26. D. D. Piekna-Przybylska, W. A. Decatur, M. J. Fournier, The 3D rRNA modification maps database: With interactive tools for ribosome analysis. *Nucleic Acids Res* **36** (2008).
27. P. Cottilli, Y. Itoh, Y. Nobe, A. S. Petrov, P. Lisón, M. Taoka, A. Amunts, Cryo-EM structure and rRNA modification sites of a plant ribosome. *Plant Commun* **3**, 100342 (2022).
28. J. Smirnova, J. Loerke, G. Kleinau, A. Schmidt, J. Bürger, E. H. Meyer, T. Mielke, P. Scheerer, R. Bock, C. M. T. Spahn, R. Zoschke, Structure of the actively translating plant 80S ribosome at 2.2 Å resolution. *Nat Plants* **9**, 987–1000 (2023).
29. D. Bar-Yaacov, I. Frumkin, Y. Yashiro, T. Chujo, Y. Ishigami, Y. Chemla, A. Blumberg, O. Schlesinger, P. Bieri, B. Greber, N. Ban, R. Zarivach, L. Alfonta, Y. Pilpel, T. Suzuki, D. Mishmar, Mitochondrial 16S rRNA Is Methylated by tRNA Methyltransferase TRMT61B in All Vertebrates. *PLoS Biol* **14**, e1002557 (2016).
30. J. Chen, Y. Bai, Y. Huang, M. Cui, Y. Wang, Z. Gu, X. Wu, Y. Li, Y. S. Rong, The Ptch/SPOUT1 methyltransferase deposits an m ^{3} U modification on 28 *S* rRNA for normal ribosomal function in flies and humans. *Sci Adv* **10**, 1743 (2024).
31. D. Palm, D. Streit, T. Shanmugam, B. L. Weis, M. Ruprecht, S. Simm, E. Schleiff, Plant-specific ribosome biogenesis factors in Arabidopsis thaliana with essential function in rRNA processing. *Nucleic Acids Res* **47**, 1880–1895 (2019).
32. B. L. Weis, S. Missbach, J. Marzi, M. T. Bohnsack, E. Schleiff, The 60S associated ribosome biogenesis factor LSG1-2 is required for 40S maturation in Arabidopsis thaliana. *The Plant Journal* **80**, 1043–1056 (2014).
33. G. Horiguchi, A. Mollá-Morales, J. M. Pérez-Pérez, K. Kojima, P. Robles, M. R. Ponce, J. L. Micol, H. Tsukaya, Differential contributions of ribosomal protein genes to Arabidopsis thaliana leaf development. *The Plant Journal* **65**, 724–736 (2011).
34. N. T. Ingolia, Ribosome Footprint Profiling of Translation throughout the Genome. *Cell* **165**, 22–33 (2016).
35. L. Muñiz, E. G. Minguet, S. K. Singh, E. Pesquet, F. Vera-Sirera, C. L. Moreau-Courtois, J. Carbonell, M. A. Blázquez, H. Tuominen, ACAULIS5 controls Arabidopsis xylem specification through the prevention of premature cell death. *Development* **135**, 2573–82 (2008).
36. F. Vera-Sirera, B. De Rybel, C. Úrbez, E. Kouklas, M. Pesquera, J. C. Álvarez-Mahecha, E. G. Minguet, H. Tuominen, J. Carbonell, J. W. Borst, D. Weijers, M. A. Blázquez, A bHLH-Based Feedback Loop Restricts Vascular Cell Proliferation in Plants. *Dev Cell* **35**, 432–443 (2015).
37. H. Katayama, K. Iwamoto, Y. Kariya, T. Asakawa, T. Kan, H. Fukuda, K. Ohashi-Ito, A negative feedback loop controlling bHLH complexes is involved in vascular cell division and differentiation in the root apical meristem. *Current Biology* **25**, 3144–3150 (2015).
38. A. Imai, Y. Hanzawa, M. Komura, K. T. Yamamoto, Y. Komeda, T. Takahashi, The dwarf phenotype of the Arabidopsis ac15 mutant is suppressed by a mutation in an upstream ORF of a bHLH gene. *Development* **133**, 3575–3585 (2006).
39. Y. Hanzawa, T. Takahashi, Y. Komeda, ACL5: an Arabidopsis gene required for internodal elongation after flowering. *The Plant Journal* **12**, 863–874 (1997).
40. M. Saraumi, T. Tanaka, D. Koyama, Y. Nishi, Y. Takahashi, H. Motose, T. Takahashi, RNA processing/modifying enzymes play key roles in the response to thermospermine in Arabidopsis thaliana. *The Plant Journal* **123**, e70476 (2025).
41. J. I. Kakehi, E. Kawano, K. Yoshimoto, Q. Cai, A. Imai, T. Takahashi, Mutations in Ribosomal Proteins, RPL4 and RACK1, Suppress the Phenotype of a Thermospermine-Deficient Mutant of Arabidopsis thaliana. *PLoS One* **10**, e0117309 (2015).
42. M. Riefler, O. Novak, M. Strnad, T. Schmülling, Arabidopsis Cytokinin Receptor Mutants Reveal Functions in Shoot Growth, Leaf Senescence, Seed Size, Germination, Root Development, and Cytokinin Metabolism. *Plant Cell* **18**, 40–54 (2006).

43. K. Yoshimoto, H. Takamura, I. Kadota, H. Motose, T. Takahashi, Chemical control of xylem differentiation by thermospermine, xylemin and auxin. *Sci Rep* **6**, 21487 (2016).
44. T. Wang, K. Birsoy, N. W. Hughes, K. M. Krupczak, Y. Post, J. J. Wei, E. S. Lander, D. M. Sabatini, Identification and characterization of essential genes in the human genome. *Science (1979)* **350**, 1096–1101 (2015).
45. Q. Cai, H. Fukushima, M. Yamamoto, N. Ishii, T. Sakamoto, T. Kurata, H. Motose, T. Takahashi, The *SAC51* Family Plays a Central Role in Thermospermine Responses in Arabidopsis. *Plant Cell Physiol* **57**, 1583–1592 (2016).
46. J. I. Kakehi, Y. Kuwashiro, H. Motose, K. Igarashi, T. Takahashi, Norspermine substitutes for thermospermine in the control of stem elongation in Arabidopsis thaliana. *FEBS Lett* **584**, 3042–3046 (2010).
47. S. Baima, V. Forte, M. Possenti, A. Peñalosa, G. Leoni, S. Salvi, B. Felici, I. Ruberti, G. Morelli, Negative Feedback Regulation of Auxin Signaling by ATHB8/ACL5–BUD2 Transcription Module. *Mol Plant* **7**, 1006–1025 (2014).
48. D. W. Kim, K. Watanabe, C. Murayama, S. Izawa, M. Niitsu, A. J. Michael, T. Berberich, T. Kusano, Polyamine oxidase5 regulates arabidopsis growth through thermospermine oxidase activity. *Plant Physiol* **165**, 1575–1590 (2014).
49. S. Shinohara, T. Okamoto, H. Motose, T. Takahashi, Salt hypersensitivity is associated with excessive xylem development in a thermospermine-deficient mutant of Arabidopsis thaliana. *Plant Journal* **100**, 374–383 (2019).
50. J. W. S. Brown, G. P. Clark, D. J. Leader, C. G. Simpson, T. Lowe, Multiple snoRNA gene clusters from Arabidopsis. *RNA* **7**, 1817–1832 (2001).
51. M. Higuchi, M. S. Pischke, A. P. Mähönen, K. Miyawaki, Y. Hashimoto, M. Seki, M. Kobayashi, K. Shinozaki, T. Kato, S. Tabata, Y. Helariutta, M. R. Sussman, T. Kakimoto, In planta functions of the Arabidopsis cytokinin receptor family. *Proc Natl Acad Sci U S A* **101**, 8821–8826 (2004).
52. T. Murashige, F. Skoog, A Revised Medium for Rapid Growth and Bio Assays with Tobacco Tissue Cultures. *Physiol Plant* **15**, 473–497 (1962).
53. D. I. Pcurar, M. L. Păcurar, N. Street, J. D. Bussell, T. I. Pop, L. Gutierrez, C. Bellini, A collection of INDEL markers for map-based cloning in seven Arabidopsis accessions. *J Exp Bot* **63**, 2491–2501 (2012).
54. M. M. Neff, E. Turk, M. Kalishman, Web-based primer design for single nucleotide polymorphism analysis. *Trends Genet* **18**, 613–615 (2002).
55. P. Somervuo, L. Holm, SANSparallel: interactive homology search against Uniprot. *Nucleic Acids Res* **43**, W24–W29 (2015).
56. L. Holm, Using Dali for Protein Structure Comparison. *Methods Mol Biol* **2112**, 29–42 (2020).
57. J. M. Engreitz, A. Pandya-Jones, P. McDonel, A. Shishkin, K. Sirokman, C. Surka, S. Kadri, J. Xing, A. Goren, E. S. Lander, K. Plath, M. Guttman, The Xist lncRNA exploits three-dimensional genome architecture to spread across the X chromosome. *Science* **341** (2013).
58. S. Schwartz, D. A. Bernstein, M. R. Mumbach, M. Jovanovic, R. H. Herbst, B. X. León-Ricardo, J. M. Engreitz, M. Guttman, R. Satija, E. S. Lander, G. Fink, A. Regev, Transcriptome-wide mapping reveals widespread dynamic-regulated pseudouridylation of ncRNA and mRNA. *Cell* **159**, 148–162 (2014).
59. B. Langmead, S. L. Salzberg, Fast gapped-read alignment with Bowtie 2. *Nature Methods 2012 9:4* **9**, 357–359 (2012).
60. Z. W. Dong, P. Shao, L. T. Diao, H. Zhou, C. H. Yu, L. H. Qu, RTL-P: a sensitive approach for detecting sites of 2′-O-methylation in RNA molecules. *Nucleic Acids Res* **40**, e157–e157 (2012).
61. S. Douthwaite, F. Kirpekar, Identifying Modifications in RNA by MALDI Mass Spectrometry. *Methods Enzymol* **425**, 1–20 (2007).
62. A. Alekseenko, D. Barrett, Y. Pareja-Sanchez, R. J. Howard, E. Strandback, H. Ampah-Korsah, U. Rovšnik, S. Zuniga-Veliz, A. Klenov, J. Malloo, S. Ye, X. Liu, B. Reinius, S. J. Elsässer, T. Nyman, G. Sandh, X. Yin, V. Pelechano, Direct detection of SARS-CoV-2 using non-commercial RT-LAMP reagents on heat-inactivated samples. *Sci Rep* **11**, 1–10 (2021).
63. A. Shapiguzov, J. P. Vainonen, K. Hunter, H. Tossavainen, A. Tiwari, S. Järvi, M. Hellman, F. Aarabi, S. Alseekh, B. Wybouw, K. van der Kelen, L. Nikkanen, J. Krasensky-Wrzaczek, N. Sipari, M. Keinänen, E. Tyystjärvi, E. Rintamäki, B. De Rybel, J. Salojärvi, F. van Breusegem, A. R. Fernie, M. Brosché, P. Permi, E. M. Aro, M. Wrzaczek, J. Kangasjärvi, Arabidopsis RCD1 coordinates chloroplast and mitochondrial functions through interaction with ANAC transcription factors. *Elife* **8** (2019).
64. M. E. Zanetti, I. F. Chang, F. Gong, D. W. Galbraith, J. Bailey-Serres, Immunopurification of polyribosomal complexes of Arabidopsis for global analysis of gene expression. *Plant Physiol* **138**, 624–635 (2005).

65. S. Chen, Y. Zhou, Y. Chen, J. Gu, fastp: an ultra-fast all-in-one FASTQ preprocessor. *Bioinformatics* **34**, i884–i890 (2018).
66. A. Dobin, C. A. Davis, F. Schlesinger, J. Drenkow, C. Zaleski, S. Jha, P. Batut, M. Chaisson, T. R. Gingeras, STAR: ultrafast universal RNA-seq aligner. *Bioinformatics* **29**, 15–21 (2013).
67. J. Ou, M. Hoye, ribosomeProfilingQC: Ribosome Profiling Quality Control. [Preprint] (2025). https://doi.org/doi:10.18129/B9.bioc.ribosomeProfilingQC.
68. M. D. Robinson, D. J. McCarthy, G. K. Smyth, edgeR: a Bioconductor package for differential expression analysis of digital gene expression data. *Bioinformatics* **26**, 139–140 (2010).
69. H. Y. L. Wu, Q. Ai, R. T. Teixeira, P. H. T. Nguyen, G. Song, C. Montes, J. M. Elmore, J. W. Walley, P. Y. Hsu, Improved super-resolution ribosome profiling reveals prevalent translation of upstream ORFs and small ORFs in Arabidopsis. *Plant Cell* **36**, 510–539 (2024).
70. A. Punjani, J. L. Rubinstein, D. J. Fleet, M. A. Brubaker, cryoSPARC: algorithms for rapid unsupervised cryo-EM structure determination. *Nature Methods 2017 14:3* **14**, 290–296 (2017).
71. S. H. W. Scheres, RELION: Implementation of a Bayesian approach to cryo-EM structure determination. *J Struct Biol* **180**, 519–530 (2012).
72. S. Q. Zheng, E. Palovcak, J. P. Armache, K. A. Verba, Y. Cheng, D. A. Agard, MotionCor2: anisotropic correction of beam-induced motion for improved cryo-electron microscopy. *Nature Methods 2017 14:4* **14**, 331–332 (2017).
73. A. Rohou, N. Grigorieff, CTFFIND4: Fast and accurate defocus estimation from electron micrographs. *J Struct Biol* **192**, 216–221 (2015).
74. E. D. Zhong, T. Bepler, B. Berger, J. H. Davis, CryoDRGN: reconstruction of heterogeneous cryo-EM structures using neural networks. *Nature Methods 2021 18:2* **18**, 176–185 (2021).
75. J. L. Rubinstein, M. A. Brubaker, Alignment of cryo-EM movies of individual particles by optimization of image translations. *J Struct Biol* **192**, 188–195 (2015).
76. D. Asarnow, E. Palovcak, Y. Cheng, asarnow/pyem: UCSF pyem v0.5. doi: 10.5281/ZENODO.3576630.
77. P. Emsley, B. Lohkamp, W. G. Scott, K. Cowtan, Features and development of Coot. *urn:issn:0907-4449* **66**, 486–501 (2010).
78. K. Yamashita, C. M. Palmer, T. Burnley, G. N. Murshudov, Cryo-EM single-particle structure refinement and map calculation using Servalcat. *Acta Crystallogr D Struct Biol* **77**, 1282–1291 (2021).
79. P. V. Afonine, B. K. Poon, R. J. Read, O. V. Sobolev, T. C. Terwilliger, A. Urzhumtsev, P. D. Adams, Real-space refinement in PHENIX for cryo-EM and crystallography. *Acta Crystallogr D Struct Biol* **74**, 531 (2018).
80. E. C. Meng, T. D. Goddard, E. F. Pettersen, G. S. Couch, Z. J. Pearson, J. H. Morris, T. E. Ferrin, UCSF ChimeraX: Tools for structure building and analysis. *Protein Science* **32**, e4792 (2023).
81. J. Cox, M. Y. Hein, C. A. Luber, I. Paron, N. Nagaraj, M. Mann, Accurate proteome-wide label-free quantification by delayed normalization and maximal peptide ratio extraction, termed MaxLFQ. *Molecular and Cellular Proteomics* **13**, 2513–2526 (2014).
82. D. Binns, E. Dimmer, R. Huntley, D. Barrell, C. O'Donovan, R. Apweiler, QuickGO: a web-based tool for Gene Ontology searching. *Bioinformatics* **25**, 3045–3046 (2009).
83. F. Yu, S. E. Haynes, G. C. Teo, D. M. Avtonomov, D. A. Polasky, A. I. Nesvizhskii, Fast Quantitative Analysis of timsTOF PASEF Data with MSFragger and IonQuant. *Molecular and Cellular Proteomics* **19**, 1575–1585 (2020).
84. R. P. Hellens, A. C. Allan, E. N. Friel, K. Bolitho, K. Grafton, M. D. Templeton, S. Karunairetnam, A. P. Gleave, W. A. Laing, Transient expression vectors for functional genomics, quantification of promoter activity and RNA silencing in plants. *Plant Methods* **1**, 1–14 (2005).
85. G. Jach, E. Binot, S. Frings, K. Luxa, J. Schell, Use of red fluorescent protein from Discosoma sp. (dsRED) as a reporter for plant gene expression. *The Plant Journal* **28**, 483–491 (2001).
86. R. Siligato, X. Wang, S. R. Yadav, S. Lehesranta, G. Ma, R. Ursache, I. Sevilem, J. Zhang, M. Gorte, K. Prasad, M. Wrzaczek, R. Heidstra, A. Murphy, B. Scheres, A. P. Mähönen, MultiSite Gateway-Compatible Cell Type-Specific Gene-Inducible System for Plants. *Plant Physiol* **170**, 627–641 (2016).
87. M. Karimi, A. Bleys, R. Vanderhaeghen, P. Hilson, Building Blocks for Plant Gene Assembly. *Plant Physiol* **145**, 1183–1191 (2007).
88. A. P. Rideau, C. Gooding, P. J. Simpson, T. P. Monie, M. Lorenz, S. Hüttelmaier, R. H. Singer, S. Matthews, S. Curry, C. W. J. Smith, A peptide motif in Raver1 mediates splicing repression by interaction with the PTB RRM2 domain. *Nat Struct Mol Biol* **13**, 839–848 (2006).
89. E. Weber, C. Engler, R. Gruetzner, S. Werner, S. Marillonnet, A modular cloning system for standardized assembly of multigene constructs. *PLoS One* **6** (2011).

90. S. J. Clough, A. F. Bent, Floral dip: a simplified method for Agrobacterium-mediated transformation of Arabidopsis thaliana. *Plant J* **16**, 735–743 (1998).
91. T. L. Shimada, T. Shimada, I. Hara-Nishimura, A rapid and non-destructive screenable marker, FAST, for identifying transformed seeds of Arabidopsis thaliana. *Plant J* **61**, 519–528 (2010).
92. S. D. Yoo, Y. H. Cho, J. Sheen, Arabidopsis mesophyll protoplasts: a versatile cell system for transient gene expression analysis. *Nature Protocols 2007 2:7* **2**, 1565–1572 (2007).
93. R. Ogura, N. Matsuo, N. Wako, T. Tanaka, S. Ono, K. Hiratsuka, Dual luciferase reporter assay : An advanced co-reporter technology integrating firefly and renilla luciferase assays. *Promega Notes* **57**, 2- (1996).
94. K. Norkunas, R. Harding, J. Dale, B. Dugdale, Improving agroinfiltration-based transient gene expression in Nicotiana benthamiana. *Plant Methods* **14**, 1–14 (2018).
95. W. Kim, S. Ć. Zeljković, U. Piskurewicz, C. Megies, P. Tarkowski, L. Lopez-Molina, polyamine uptake transporter 2 (put2) and decaying seeds enhance phyA-mediated germination by overcoming PIF1 repression of germination. *PLoS Genet* **15**, e1008292 (2019).
96. C. F. Marchetti, L. Ugena, J. F. Humplík, M. Polák, S. Ćavar Zeljković, K. Podlešáková, T. Fürst, N. De Diego, L. Spíchal, A Novel Image-Based Screening Method to Study Water-Deficit Response and Recovery of Barley Populations Using Canopy Dynamics Phenotyping and Simple Metabolite Profiling. *Front Plant Sci* **10**, 1252 (2019).
97. B. Scheres, H. Wolkenfelt, V. Willemsen, M. Terlouw, E. Lawson, C. Dean, P. Weisbeek, Embryonic origin of the Arabidopsis primary root and root meristem initials. *Development* **120**, 2475–2487 (1994).
98. A. P. Mähönen, M. Bonke, L. Kauppinen, M. Riikonen, P. N. Benfey, Y. Helariutta, A novel two-component hybrid molecule regulates vascular morphogenesis of the Arabidopsis root. *Genes Dev* **14**, 2938–2943 (2000).
99. R. Ursache, T. G. Andersen, P. Marhavý, N. Geldner, A protocol for combining fluorescent proteins with histological stains for diverse cell wall components. *Plant J* **93**, 399–412 (2018).
100. K. Miyawaki, M. Matsumoto-Kitano, T. Kakimoto, Expression of cytokinin biosynthetic isopentenyltransferase genes in Arabidopsis: tissue specificity and regulation by auxin, cytokinin, and nitrate. *Plant J* **37**, 128–138 (2004).
101. O. Smetana, R. Mäkilä, M. Lyu, A. Amiryousefi, F. Sánchez Rodríguez, M. F. Wu, A. Solé-Gil, M. Leal Gavarrón, R. Siligato, S. Miyashima, P. Roszak, T. Blomster, J. W. Reed, S. Broholm, A. P. Mähönen, High levels of auxin signalling define the stem-cell organizer of the vascular cambium. *Nature* **565**, 485–489 (2019).
102. J. Schindelin, I. Arganda-Carreras, E. Frise, V. Kaynig, M. Longair, T. Pietzsch, S. Preibisch, C. Rueden, S. Saalfeld, B. Schmid, J. Y. Tinevez, D. J. White, V. Hartenstein, K. Eliceiri, P. Tomancak, A. Cardona, Fiji: an open-source platform for biological-image analysis. *Nature Methods 2012 9:7* **9**, 676–682 (2012).
103. C. Stringer, T. Wang, M. Michaelos, M. Pachitariu, Cellpose: a generalist algorithm for cellular segmentation. *Nat Methods* **18**, 100–106 (2021).
104. J. H. Rowe, A. Rizza, A. M. Jones, Quantifying Phytohormones in Vivo with FRET Biosensors and the FRETENATOR Analysis Toolset. *Methods in Molecular Biology* **2494**, 239–253 (2022).
105. J. Rowe, M. Grangé-Guermente, M. Exposito-Rodriguez, R. Wimalasekera, M. O. Lenz, K. N. Shetty, S. R. Cutler, A. M. Jones, Next-generation ABACUS biosensors reveal cellular ABA dynamics driving root growth at low aerial humidity. *Nature Plants 2023 9:7* **9**, 1103–1115 (2023).
106. R. Ruonala, D. Ko, Y. Helariutta, Genetic Networks in Plant Vascular Development. *Annu Rev Genet* **51**, 335–359 (2017).
107. A. P. Mähönen, A. Bishopp, M. Higuchi, K. M. Nieminen, K. Kinoshita, K. Törmäkangas, Y. Ikeda, A. Oka, T. Kakimoto, Y. Helariutta, Cytokinin signaling and its inhibitor AHP6 regulate cell fate during vascular development. *Science* **311**, 94–8 (2006).
108. B. E. H. Maden, Mapping 2′-O-Methyl Groups in Ribosomal RNA. *Methods* **25**, 374–382 (2001).
109. M. L. Guerrero-González, M. Rodríguez-Kessler, J. F. Jiménez-Bremont, UORF, a regulatory mechanism of the Arabidopsis polyamine oxidase 2. *Mol Biol Rep* **41**, 2427–2443 (2014).
110. T. Kamada-Nobusada, M. Hayashi, M. Fukazawa, H. Sakakibara, M. Nishimura, A Putative Peroxisomal Polyamine Oxidase, AtPAO4, is Involved in Polyamine Catabolism in Arabidopsis thaliana. *Plant Cell Physiol* **49**, 1272–1282 (2008).
111. A. Imai, M. Komura, E. Kawano, Y. Kuwashiro, T. Takahashi, A semi-dominant mutation in the ribosomal protein L10 gene suppresses the dwarf phenotype of the *acl5* mutant in *Arabidopsis thaliana*. *The Plant Journal* **56**, 881–890 (2008).

112. H. W. Wu, E. Fajiculay, J. F. Wu, C. C. S. Yan, C. P. Hsu, S. H. Wu, Noise reduction by upstream open reading frames. *Nature Plants 2022 8:5* **8**, 474–480 (2022).
113. J. T. Robinson, H. Thorvaldsdóttir, W. Winckler, M. Guttman, E. S. Lander, G. Getz, J. P. Mesirov, Integrative genomics viewer. *Nature Biotechnology 2011 29:1* **29**, 24–26 (2011).
114. H.-Y. L. Wu, I. D. Kaufman, P. Y. Hsu, The ggRibo single-gene viewer reveals insights into translatome and other nucleotide-resolution omics data. *Genome Res* **35**, gr.280480.125 (2025).
115. A. Sklias, S. Cruciani, V. Marchand, M. Spagnuolo, G. Lavergne, V. Bourguignon, A. Brambilla, R. Dreos, S. J. Marygold, E. M. Novoa, Y. Motorin, J. Y. Roignant, Comprehensive map of ribosomal 2′-O-methylation and C/D box snoRNAs in Drosophila melanogaster. *Nucleic Acids Res* **52**, 2848–2864 (2024).

Acknowledgments

We thank Miriam Llorian and Christopher WJ Smith for their valuable comments and experimental supports, K. Kainulainen, M. Herpola, K. Blajecka, A. Diez and E. Thomas for technical support, B. De Rybel and T. Takahashi for transgenic and mutant plants.

Funding: Y.H. was financially supported by the Center of Excellence in Tree Biology by the Academy of Finland (346139) and Academy Professor by the Academy of Finland (336727).

Y.H.'s laboratory was funded by the Gatsby Foundation (GAT3395/PR3); the National Science Foundation Biotechnology and Biological Sciences Research Council grant (BB/N013158/1); University of Helsinki (award 7999920 91), the European Research Council Advanced Investigator Grant SYMDEV (No. 323052).

M. J. F. was supported by Academy of Finland (341477).

D.K. was funded by an EMBO long-term fellowship ALTF 305-2017.

K.L. was supported by grants from the Knut and Alice Wallenberg Foundation (KAW 2016.0352, KAW 2020.0240) and the Swedish Research Council (VR 2021-04938).

J.A., S.H. and A.S. laboratories were supported by the US National Science Foundation (award No.1444561).

R.M. and K.S. were funded by the National Science Centre Poland grant (2022/47/B/NZ9/00558).

N.D.D. and S.C.Z. were funded by the project TowArds Next GENeration Crops, reg. no. CZ.02.01.01/00/22_008/0004581 of the ERDF Programme Johannes Amos Comenius.

T.V. was funded by the ANR-2018-CE13-0019 (ReinitiaTOR) grant.

V.O.P was supported by Academy of Finland (338836 and 314672), the Sigrid Juselius Foundation and the Jane and Aatos Erkko Foundation.

G.E., B.W. and A.P.M. were supported by European Research Council (ERC-CoG CORKtheCAMBIA, agreement 819422).

A.J.W. was supported by Cancer Research UK DRCNPG-Jun24/100002, UK Medical Research Council (MR/T012412/1 and UKRI1443), the European Cooperation in Science and Technology (COST) Action Translacore CA21154, and Rosetrees Trust (PGL22/100032).

R.N., A.H. and S.M. were supported by the Danish Independent Research Council | Natural Sciences (#12-125524) and the Villum Foundation.

P.T. was supported by Academy of Finland (357350).

R.F. and Z.B. were supported by Biological Sciences Research Council grant (BB/M008606/1).

M.S. was supported by the Research Council of Finland (333703, 358161, 346140 and 364180).

Author contributions: Conceptualization: D.K., R.R., E.H., A.Faille, A.P.M., R.M., A.J.W., F.K., Y.H.;

Data curation: A.Faille, A.H., R.N., S.H.;

Formal analysis: D.K., A.Ferrando, M.A.B., S.e-S., L.H., G.E., P.P., A.Faille, A.H., R.N., S.H., F.K.;

Funding acquisition: Y.H., A.J.W.;

Investigation: P.T., L.H., X.L., F.B., M.Balcerowicz, T.Ö., C.U., M.Bourdon, B.W., Z.B., A.P., M.V.S., V.O.P., S.M-P., T.D.L.R., S.C.Z., K.S., N.D.D., A.Ferrando, A.Faille, R.N., H.L., H.H., E.H., R.R., D.K., F.K., J.P.V., Xiaonan L., K. Salokas.;

Methodology: M.V., A.P., V.O.P., S.M-P., O.N., N.D.D., A.Ferrando, A.Faille, R.N., E.H., R.R., M.J.F., D.K., F.K., Y.H.;

Project administration: R.R., Y.H.;

Resources: S.M., K.L., T.V., M.A.B., M.V., L.H., R.F., O.N., A.J.W., R.M., S.H., J.A., A.S., A.P.M., F.K., Y.H.;

Software: L.H., A.H., S.H.;

Supervision: M.S., K.L., T.W., M.L., O.L., Z.B., R.F., R.N., A.P.M., F.K., Y.H.;

Validation: A.Ferrando, F.B., S.H., E.H., D.K., R.R., Y.H.;

Visualisation: D.K., R.R., E.H., H.L., A.H., A.Ferrando, M.A.B., A.Faille, H.H., F.B., R.M., F.K., Y.H.;

Writing – original draft: R.R., D.K., E.H., Y.H.;

Writing – reviewing & editing: D.K., R.R., E.H., T.V., M.J.F., A.Ferrando, M.A.B., T.W., O.L., V.O.P., A.Faille, A.J.W, J.A., A.S., R.M., A.P.M., F.K., Y.H.

Competing Interests: Ville O. Paavilainen is a shareholder of Avenue Biosciences who optimize bioproduction methods for therapeutic proteins. This does not form a financial conflict of interest with this study. Ville O. Paavilainen is an advisor and paid consultant for Gate Biosciences who are developing therapeutic client-selective protein secretion inhibitors. This does not form a financial conflict of interest with this study. Ottoline Leyser was the Chief Executive Officer of UK Research and Innovation from 06.2020 until 06.2025.

Data and materials availability: All materials used in this study are available upon request. The RNA-seq data generated in this study to identify putative m^3U sites in the rRNA were deposited in the Sequence Read Archive under BioProject PRJNA1196919. The ribosome footprinting and RNA-seq data produced in this study were deposited in the SRA under BioProject PRJNA1348229. Cryo-EM maps and models were deposited at the Electron Microscopy Data Bank and RCSB Protein Data Bank, respectively, under the following accession codes: EMD-51820, 9H3G (WT tSpm-); EMD-51899, 9H6I (WT tSpm+); EMD-52299, 9HMW (*ovac* tSpm-); EMD-52095, 9HES (*ovac* tSpm+).

Supplementary Materials

Materials and Methods

Supplementary Text

Figs. S1 to S22

Data S1 to S11

Main Figures

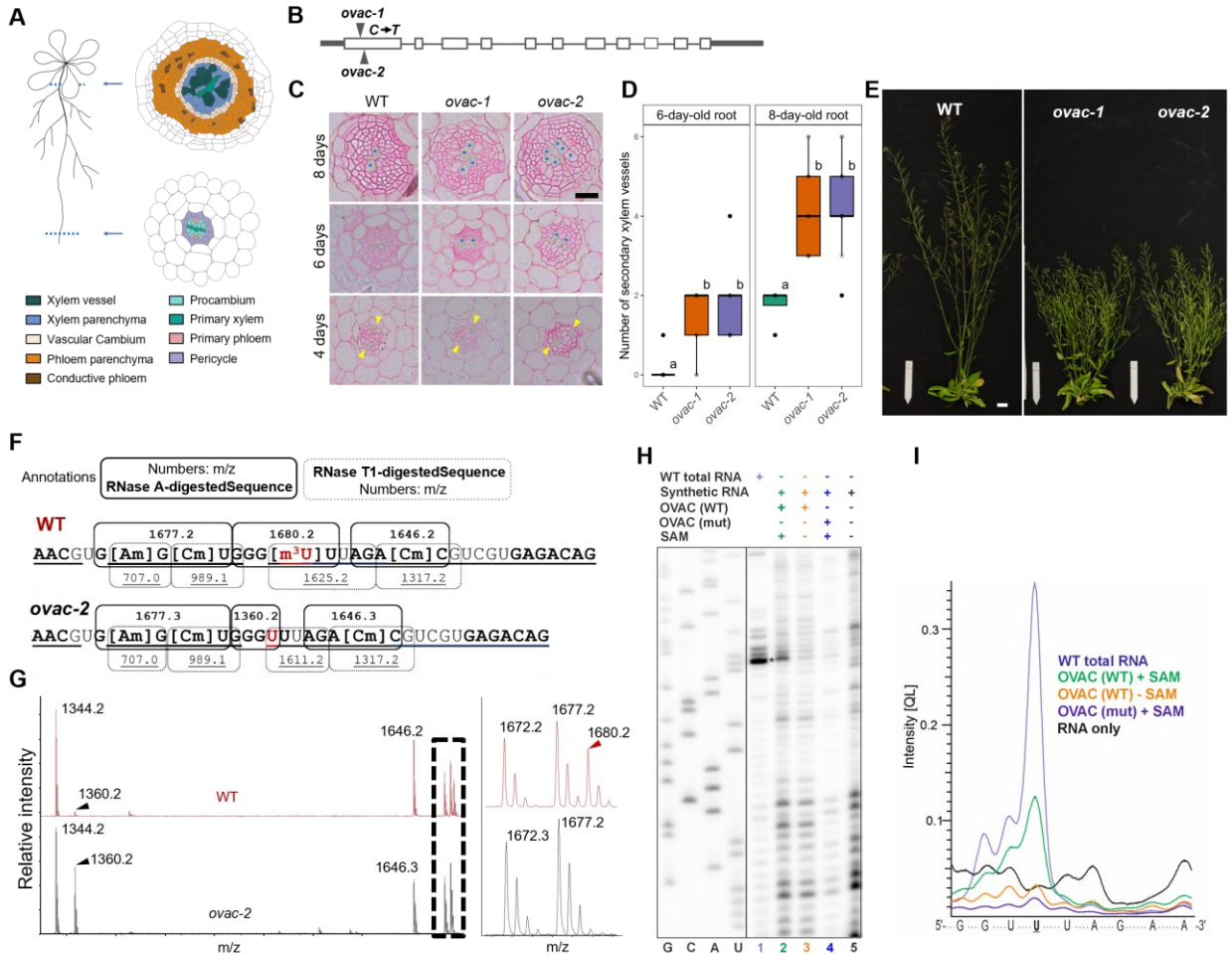


Fig. 1. OVERACHIEVER writes m^{3}U2952 in the 25S rRNA. (**A**) Primary (bottom) and secondary (top) vascular development in *Arabidopsis*. (**B**) *OVAC* gene structure with mutation sites. (**C**) Root cross-sections stained with ruthenium red showing primary (4 days) and secondary (6, 8 days) development. Yellow arrowheads, primary xylem axis; blue asterisks, secondary xylem vessels. Scale bars, 20 μm. (**D**) Quantification of the secondary xylem vessels (n = 8~13, **P ≤ 0.01, ***P ≤ 0.001, ****P ≤0.0001, Kruskal-Wallis with post-hoc Dunn's test) from (C). (**E**) 7-week-old wild type Col-0 (WT), *ovac-1,* and *ovac-2* plants. Scale bar, 2 cm. (**F**) Interpretation of RNase A (boxed) and T1 (underlined) digestion fragments from 25S rRNA from WT and *ovac-2*. m^{3}U/U2952 is marked in red. (G) Mass spectrometric analysis of RNase A-digested 25S rRNA. Red and black arrowheads indicate methylated (red) and unmethylated (black) forms. Zoomed view highlights the dot-boxed region. The ribose methylations align with (*50*). (**H**) Primer extension analysis of *in vitro* methylation reactions; sequencing ladder, lane 1: wild type total RNA, lanes 2-4: reactions using indicated conditions. (**I**) Densitometric analysis of the primer extension stop near U2952 in (H); The asterisk (H) and the bold, underlined 'U' (I) indicate the primer extension stop preceding m^{3}U2952.

A

AGI number	Gene name	*ovac* mock/WT mock		*ovac* tSpm/*ovac* mock		WT tSpm/WT mock		*ovac* tSpm/WT tSpm	
		logFC	FDR	logFC	FDR	logFC	FDR	logFC	FDR
AT5G64340	SAC51	-1.15	1.81E-01	0.93	2.13E-01	2.04	1.10E-11	-2.23	1.63E-17
AT5G09460	SACL1	-1.03	9.02E-01	-0.83	8.24E-01	0.84	6.46E-01	-2.68	1.10E-02
AT5G50010	SACL2	-0.12	1.00E+00	0.65	7.16E-01	2.30	1.93E-03	-1.75	1.73E-03
AT1G29950	SACL3	-2.53	2.63E-02	1.21	5.60E-01	1.25	4.78E-02	-2.54	5.85E-09
AT2G27230	LHW	0.02	1.00E+00	-0.42	3.87E-01	-1.24	3.14E-06	0.86	5.43E-02
AT1G06150	LHL1	-0.72	5.05E-01	-0.30	8.26E-01	-1.10	5.95E-02	0.09	1.00E+00
AT2G31280	LHL2	-0.44	9.82E-01	0.18	9.63E-01	-0.36	8.87E-01	0.14	1.00E+00
AT1G64625	LHL3/LL1	n.d	n.d	n.d	n.d	n.d	n.d	n.d	n.d

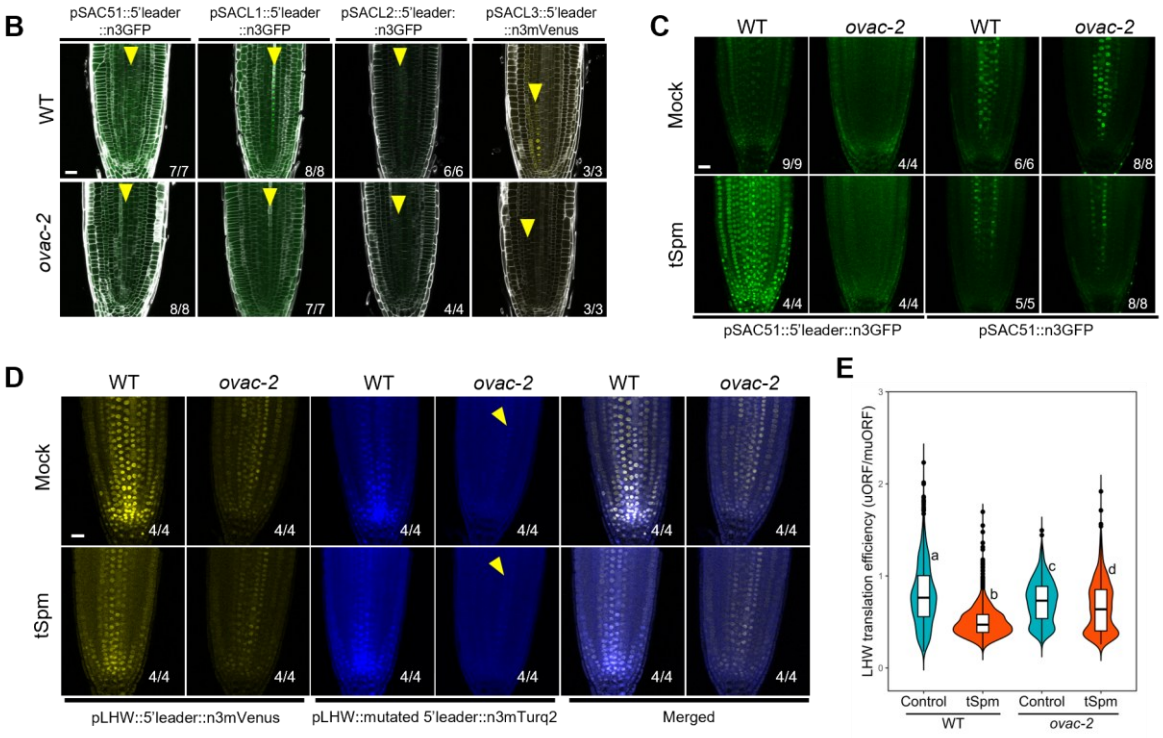


Fig. 2. m^{3}U2952 enhances bifunctional translational regulation by thermospermine (tSpm). (**A**) Translation efficiency of *SACL* and *LHW* mRNAs in the *ovac-2* mutant under steady-state conditions, and upon tSpm treatment, compared to WT. The fold change (logFC) and the associated False Discovery Rate (FDR) are shown. n.d, not detected. Red indicates significant upregulation; blue indicates significant downregulation. (**B**) *SACL* translational reporter expression in 7-day-old root apical meristems (n = 7-10). Arrowheads indicate reporter-expressing cell lineages. *SAC51*: metaxylem, *SACL3*: protoxylem, S*ACL1*: protophloem, *SACL2*: procambium. Scale bar, 20 µm. (**C**) SAC51 translation (*pSAC51*::*5'leader*::*n3GFP*) or transcription (*pSAC51*::*n3GFP)* in 8-day-old root apical meristems with/without 50 µM tSpm. Scale bar, 20 µm. (**D**) *LHW* translational (p*LHW*::*5'leader*::*n3mVenus*) and transcriptional (p*LHW*::*mutated 5'leader*::*n3mTurq2*) reporters in 8-day-old meristems treated with 50 µM tSpm. Arrowheads: the weak LHW transcriptional reporter expression in *ovac-2*. (**E**) *LHW* translation efficiency from (D) (n = 4, 1303-2249 nuclei, Wilcoxon rank-sum test with Bonferroni correction).

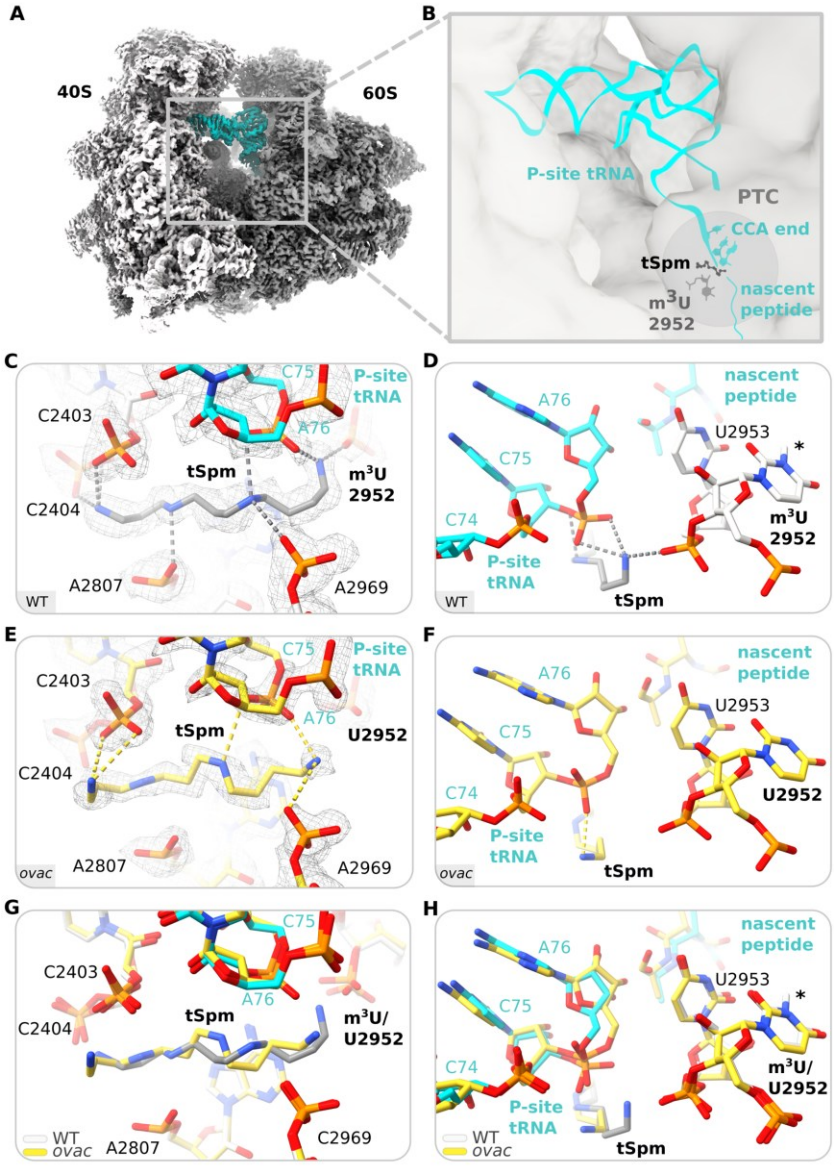


Fig. 3. m^{3}U2952 promotes functional binding of thermospermine (tSpm) to the ribosome.

(**A**) Cryo-EM map of *Arabidopsis* WT 80S ribosome with bound P-site tRNA (cyan). (**B**) Schematic of the peptidyltransferase center (PTC), with the CCA end of the P-site tRNA, tSpm, and residue m^{3}U2952 indicated. (**C**) tSpm molecule (dark grey) bound in the PTC, interacting with phosphate groups (red/orange) of rRNA (white) and tRNA (cyan). Electrostatic interactions, grey dashed lines. Cryo-EM map, grey mesh. (**D**) tSpm bridges the phosphate group linking residues m^{3}U2952 and U2953 with the CCA-end of the P-site tRNA, close to the nascent polypeptide. (**E**) tSpm molecule bound in the PTC of the *ovac* mutant ribosome. Cryo-EM map, grey mesh. (**F**) tSpm molecule adopts an altered conformation in the *ovac* mutant ribosome whereby hydrogen bonding with the phosphate group of U2953 is lost. (**G-H**) Superimposition of tSpm-bound WT (white/grey/cyan) and *ovac* mutant (yellow) ribosomes. Cryo-EM maps, grey mesh; * indicates methyl group of m^{3}U2952.

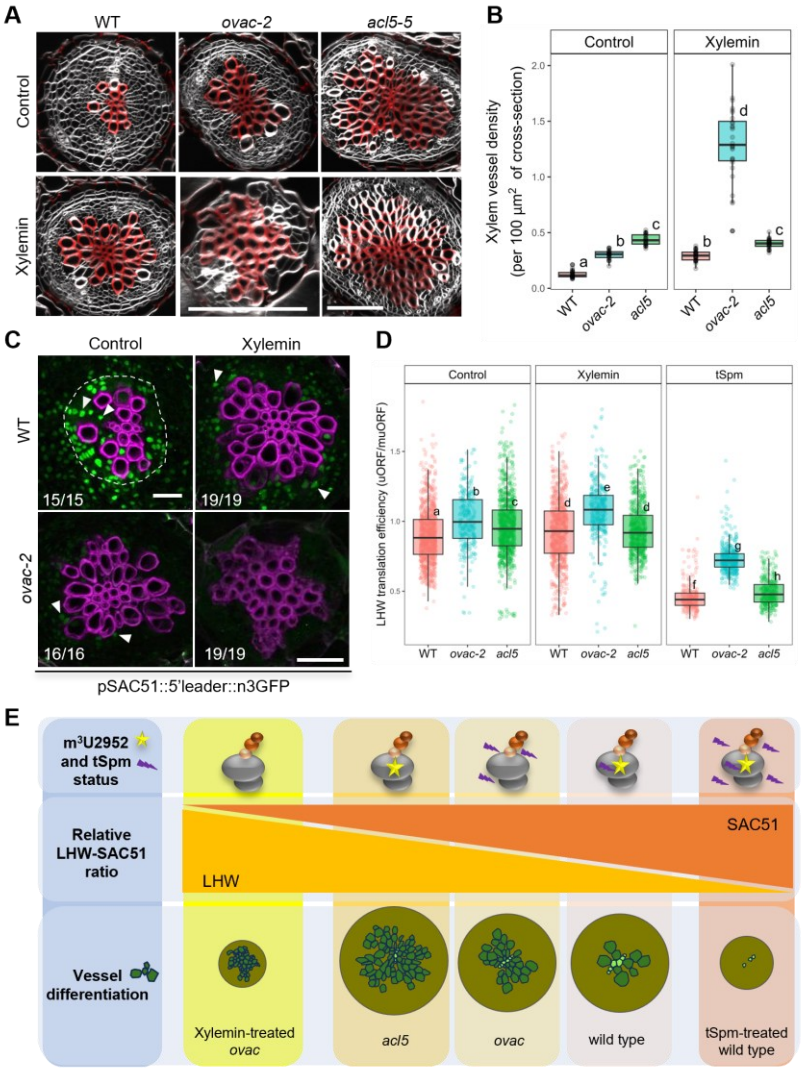


Fig. 4. Thermospermine (tSpm) binding to the methylated ribosome switches cell fate.

(**A**) Root cross-sections of plants grown for 14 days with or without 50 µM xylemin. Gray, SR2200; Red, Fuchsin staining. Scale bar, 50 µm. (**B**) Number of xylem vessels per total vascular area from (**A**) (n = 24 ~ 30, Wilcoxon rank sum test with Bonferroni correction). (**C**) Maximal z-projection of confocal images of root cross-sections of WT and *ovac-2* grown for 14 days on control or media supplemented with 50 µM xylemin. Scale bar, 20 µm. White dotted lines mark the xylem region in one panel as an example. White arrowheads highlight representative reporter expression in xylem cells. Magenta, Fuchsin staining. (**D**) *LHW* translation efficiency in mature roots of WT, *ovac-2* and *acl5* following 24 hours mock or 50 µM xylemin treatment (n = 8, Wilcoxon rank sum test with Bonferroni correction). (**E**) Schematic summary. *acl5* is predicted to have a higher LHW-to-SAC51 ratio compared to *ovac* due to its higher *LHW* transcription despite lower translation efficiency (D) (figs. S20, E to I, S22, and supplementary text). A purple symbol (tSpm) positioned next to a yellow star (m^3U2952) indicates functional tSpm binding to ribosomes. The circle background represents total cross-section area.

Science
AAAS

Supplementary Materials for

Recruitment of bifunctional regulator thermospermine to methylated ribosomes directs xylem fate

Donghwi Ko[1,3]†, Raili Ruonala[1,2,3,]†, Alexandre Faille[4]†*, Eva Hellmann[3, 5]†, Hanna Help[1], Huili Liu[10], Ronni Nielsen[6], Anders Haakonsson[6]‡, Nuria De Diego[18], Anja Paatero[2], Mariia V. Shcherbii[2], Karolina Stefanowicz[9], Sanja Ćavar Zeljković[18], Tine Drud Lundager Rasmussen[6], Ondrej Novak[12], Zsuzsanna Bodi[13], Gugan Eswaran[1, 2]§, Brecht Wybouw[1,2], Matthieu Bourdon[3]¶, Cristina Urbez[14], Xiaonan Liu[2], Kari Salokas[2], Tiina Öhman[2], Tanya Waldie[3], Petri Törönen[2], Sedeer el-Showk[1], Martin Balcerowicz[19], Fabrice Besnard[15], Xiaomin Liu[3], Patrick Perkins[16], Serina Mazzoni-Putman[17], Julia P. Vainonen[1], Maija Sierla[1], Mikko J. Frilander[2], Susanne Mandrup[6], Teva Vernoux[15], Karin Ljung[11], Alejandro Ferrando[14], Miguel A. Blazquez[14], Liisa Holm[1,2], Rupert Fray[13], Markku Varjosalo[2], Ottoline Leyser[3]#, Ville O. Paavilainen[2], Ari Pekka Mähönen[1,2], Anna Stepanova[17], Jose Alonso[17], Steffen Heber[16], Robert Malinowski[9], Finn Kirpekar[6]*, Alan J. Warren[4,7,8]*, Ykä Helariutta[1,2,3,20]*

Corresponding authors: yrjo.helariutta@helsinki.fi, ajw1000@cam.ac.uk, f.kir@bmb.sdu.dk, raf58@cam.ac.uk

The PDF file includes:

Materials and Methods
Supplementary Text
Figs. S1 to S22
Data S1 to S11
References (51 – 115)

Materials and Methods

Plant materials and growth conditions

The *Arabidopsis thaliana* (L.) Heynh (*Arabidopsis*) lines used in this study are detailed in Data S10. All *Arabidopsis* mutants are in the Columbia-0 background (Col-0, wild type, WT), except for *cre1-10* (*51*) used in the mapping experiment is in the Wassilewskija-2 (Ws-2) background, and *sacl* (*36*) as well as *sac56-d* (*41*) used as sources of corresponding point mutations are in the Landsberg (Ler) background. Col-0 plants expressing either p*SAC51*::*5'leader*::*n3GFP* or p*SAC51*::*n3GFP*(*36*) were crossed with *ovac-2* to produce *ovac-2* mutants containing these reporter constructs.

For sterile plant culture, *Arabidopsis* seeds were surface sterilized in bleach (4% sodium hypochlorite with 0.02% tween-20) for 4-5 min with vortexing, or in bleach for 6 min followed by 70% ethanol washes. After the sterilization, seeds were washed with sterile water for 5-8 times and stratified in water at 4°C in darkness for 2-4 days. Seeds were plated on half-strength Murashige and Skoog (MS) (*52*) medium containing 1% Difco agar, 1% sucrose, and 0.5g/L MES, pH 5.7. For MS medium containing auxin, thermospermine, or xylemin, we added indole-3-acetic acid (IAA, Sigma) 50 mM stock in 70% ethanol, thermospermine hydrochloride (Santa Cruz) 100 mM stock in 50% DMSO or water, or xylemin (TCI) 100 mM stock in water, as indicated in the text. For experiments that required large amounts of material (such as rRNA methylation assays, protein extractions, ribosome purifications, and footprinting), the seeds were plated on nylon mesh (Normesh, 100 μm) and placed on the growth medium. The plates were incubated vertically in a 23°C growth chamber with long-day settings (16/8 hours light/dark) unless noted otherwise. Seedlings were grown on plates for up to 14 days before the experiments. For experiments requiring an extended period of growth, such as crossing, transformation, observation of adult plant phenotypes or propagation, the stratified *Arabidopsis* seeds were placed directly on compost (Levington F2) or transferred to compost as seedlings after cultivating on sterile plates for about one week. Crosses were performed by emasculating pistils and manually pollinating with the pollen of chosen lines, thus avoiding the self-pollination characteristic of *Arabidopsis*.

Experimental design and statistical analysis

Plants were grown in randomized positions, and samples were collected randomly, excluding individuals with visibly abnormal growth. Sample sizes for phenotyping and confocal imaging followed by quantification were determined based on experimental feasibility and data variability. The number of biological replicates is provided in each figure legend. Data were tested for normality and homogeneity of variance to determine the appropriate statistical tests, which are indicated in the corresponding figure legends.

EMS mutant screen and identification of the mutated gene

Seeds were treated with 0.2 % ethyl methanesulfonate (EMS) for 16 h at room temperature in darkness. Primary roots of 5-d old M2 seedlings were initially screened for altered GFP expression under a stereomicroscope (Leica), and subsequently the GFP pattern was analyzed in optical cross sections, typically 50 μm shoot-ward of the quiescent center, under a Leica TCS SP5 II confocal laser scanning microscope using a solid-state blue laser for GFP (480 nm/270 mW) at 63x magnification. For the confocal analyses, roots were mounted in 50 μg/mL propidium iodide solution (Sigma) to counter-stain cell borders. To identify the mutated gene, two strategies were applied. First, the double mutant *ovac-1 cre1-12 pAHP6::GFP* (Col-0) was crossed with *cre1-10* (Ws-2) (*51*) to generate an F2 mapping population for

amplified fragment length polymorphism analyses, yet maintaining the cytokinin hyposensitivity characteristic across the population. A mapping population of 15 individuals was selected based on a strong, expanded *pAHP6::GFP* signal in the primary root (fig. S1A) and a stunted, bushy growth habit of the adult plant (Fig. 1E). Second, whole-genome resequencing of the newly isolated mutant was performed (HiSeq2000 platform, Beijing Genomics Institute, BGI) to identify single nucleotide polymorphisms (SNPs). To create a single-mutant *ovac-1* free of excess second-site point mutations, and to analyze the Mendelian inheritance pattern of phenotypic traits such as the stunted growth habit linked with the mutation, the EMS-generated *ovac-1 cre1-12 pAHP6::GFP* was crossed with Col-0 (with or without the *pAHP6::GFP* marker) twice.

Based on the rough mapping approach, a 1.5 Mb window between markers nga106 (http://signal.salk.edu/genome/SSLP_info/SSLPsordered.html 5.613.000 Mb) and UPSC_5-7134 (*53*) (7.134.242 Mb) was established in chromosome 5. Based on the whole-genome sequencing, two SNPs were identified within the rough mapping window: a C to A at position 6931476 that resides within an intron (At5g20490), and a C to T nonsense mutation at position 6495740 that results in an in-frame premature stop codon in the first exon of At5g19300 (Q50*, residue +148 from ATG). Once the nonsense mutation in At5g19300 was identified, we designed a genotyping analysis based on a derived cleaved amplified polymorphic sequence (dCAPS, (*54*) ; Data S11) assay for *ovac-1* by digesting a PCR product of *OVAC* containing the target site with AvaII.

An additional *ovac* allele, *ovac-2* (SAIL_722_B08), was obtained from the Nottingham Arabidopsis Stock Centre (NASC) and crossed with Col-0 to confirm the genetic inheritance of the allele and isolate a homozygous transferred DNA (T-DNA) insertion mutant line in the F3 generation for subsequent experiments. *ovac-2* (V85, +256 from ATG) is a knockout allele with T-DNA insertion interrupting the first exon. This genotype was confirmed with primer pairs designed to amplify a WT allele or a T-DNA disrupted allele (Data S11, http://signal.salk.edu/tdnaprimers.2.html). The *OVAC* coding sequence is disrupted upstream of the RNA methyltransferase domain in both *ovac* alleles.

Protein homology modeling

The SANSparallel tool (*55*) was used for OVAC protein homology search and the Distance matrix alignment (Dali) web server (*56*) for structure comparisons.

DAPI staining

Seedlings (7–10 days old) expressing pOVAC::eGFP::OVAC were incubated for 20 minutes in DAPI staining solution (2 µg/mL 4′,6-diamidino-2-phenylindole (DAPI) and 0.1% (v/v) Tween 20 in phosphate-buffered saline (PBS) buffer), then washed three times with PBS buffer prior to confocal imaging.

Identification of m^3U sites in the rRNA by RNA sequencing and polymerase chain reaction

Wild-type and *ovac-2* seedlings were grown on half MS medium for 4 days and transferred on the same medium supplemented with 1 µM auxin to induce outgrowth of lateral roots for another 4 days before harvesting the roots. Total RNA was extracted using the RNeasy Plant Mini kit with an on-column DNase treatment according to manufacturer's instructions (Qiagen) and again treated with DNaseI (Roche) before proceeding. To screen for RNA modifications at a single-nucleotide resolution, such as m^3U that interfere with Watson-Crick base pairing during reverse transcription, we adapted library preparation methods described in (*57*, *58*). Briefly, total RNA was fragmented to 80-150 bp using Magnesium RNA fragmentation and stop solution (NEB) for 5 min and analyzed on a Bioanalyzer 2100 using an RNA Pico chip (Agilent). The fragmented RNA was dephosphorylated with FastAP Thermosensitive Alkaline Phosphatase (Thermo Scientific), and a 3' adaptor was ligated with T4 RNA Ligase I (NEB). The ligated RNA was reverse transcribed using AffinityScript Reverse Transcriptase (Agilent) at 55°C for 10 min. RNA was degraded, and a 5' adaptor was ligated to the cDNA with FastAP Thermosensitive Alkaline Phosphatase (Thermo Scientific). We used the RNA Clean & Concentrator-5 kit (Zymo Research) to clean reactions throughout the protocol. Adaptor and reverse transcriptase primer sequences were as detailed in (*57*) (Data S11). The cDNA libraries were amplified for 12 cycles, cleaned with AMPure XP beads (Agencourt), and sequenced on Illumina HiSeq with 30-bp paired-end reads.

Using bowtie2 (*59*), the 250-340000 read pairs of each cDNA library were aligned to the *Arabidopsis* whole genome (TAIR10) and to the rRNA sequences taken from GenBank entries X52322 and AF335842. About 98% aligned to the whole genome, whereas ~85% and ~82% read pairs of wild type and *ovac-2*, respectively, aligned to the rRNA sequences. To identify rRNA positions with the termination of reverse transcriptase significantly differing between wild type and *ovac-2*, the RNA sequencing data were analyzed following calculations and criteria described in (*58*). Essentially, the two criteria that were to be satisfied were: Ψ-ratio >0.1 (Ψ-ratio = 3' coverage+1 / coverage+1) and log2(Ψ-ratio[ovac-2] / Ψ-ratio[Col-0])| >3.

To detect m^3U2952 using RTL-P (Reverse Transcription at Low dNTP concentrations followed by Polymerase Chain Reaction) as described previously (*30*, *60*), total RNA was extracted from 12-day-old seedlings following the method mentioned above. Reverse transcription was performed in a 20 µL reaction containing 400 ng of total RNA, 5 µM dNTPs, and 2.5 µM 25S rRNA-specific primer (Data S11). The resulting cDNA was amplified through a 21-cycle PCR using EmeraldAmp MAX PCR Master Mix (Takara Bio).

Mass spectrometry (MS) analyzes for identification of modified nucleosides

Total RNA was extracted from wild-type, *ovac-2,* and *acl5-5* roots (root tips enriched by an auxin treatment as described above), as well as wild-type cotyledons and cauline leaves using the RNeasy Plant Mini kit

with an on-column DNase treatment according to manufacturer's instructions (Qiagen). Cotyledons were harvested from 7-day-old sterile seedlings and cauline leaves from adult plants grown on compost.

Relevant 25S rRNA sub-fragments were digested with the pyrimidine-specific RNase A (the digestion is characteristically inhibited by an m^3U or a ribose methylation) or G-specific RNase T1, purified and analyzed by MALDI reflectron Time-of-Flight (MALDI-TOF) mass spectrometry according to (*61*).

For quantitative analyses of the OVAC-dependent modification, one sample (such as wild type) was RNase A -digested in ^{18}O water and the comparison (such as *acl5*) in normal water, resulting in a two-Dalton mass difference when the digests were co-analyzed by MS. Finally, the signal intensities of the unmodified GGGU2952 products were compared and normalized for sample input through the intensity of an unrelated digestion product.

OVAC protein purification

Expression of the OVAC wild-type and OVAC-mut (with mutated G335A, G339A residues) recombinant proteins tagged with a maltose-binding protein (MBP) was carried out in one liter of *Escherichia coli* BL21 (DE3) in Luria-Bertani (LB) media supplemented with kanamycin. The expression was induced with Isopropyl β-d-1-thiogalactopyranoside (IPTG) when OD_{600} reached approximately 0.9-1.0, and the expression was allowed to continue at 18°C for 12 hours. The next day, the cells were collected by centrifugation, washed once with PBS, and cell pellets stored at -75°C.

The cell pellets were thawed on ice and cells were resuspended into 25 milliliters of ice-cold lysis buffer (10 mM imidazole, 250 mM NaCl, 50 mM, Tris-HCl pH 8.0) with freshly added 1 mM phenylmethylsulfonyl fluoride (PMSF). The cell suspension was passed through Emulsiflex for 10 min at 10,000 psi at 4°C to lyse the cells. The lysate was centrifuged in SS-34 rotor at 10,000 g at 4°C for 30 min to remove large debris. The clarified lysate was applied on to 1 mL Ni-NTA beads and allowed to bind the resin with end-to-end mixing for 3 hours at 4°C. The beads were then spun down and washed with 30 mL wash buffer (20 mM Imidazole, 250 mM NaCl, 10 mM Tris, pH 8.0) in total four times. The bound proteins were eluted with 3 x 2 mL of elution buffer (350 mM Imidazole, 250 mM NaCl, 10 mM Tris, pH 8.0). The eluates were dialysed overnight at 4°C against storage buffer (200 mM NaCl, 1 mM DTT, 20 mM Tris-HCl pH 8.0) and concentrated with a 10 kDa cutoff Amicon concentrator.

The concentration of the purified proteins was determined by comparing with a Bovine Serum Albumin (BSA) standard on a Coomassie stained SDS-PAGE. The gel was scanned using Sapphire FL Biomolecular Imager and quantified by AzureSpot Pro 1.4 program.

Primer extension analysis and *in vitro* methyltransferase reaction conditions

Primer extension analysis was used to map the m^3U2952 residues on *Arabidopsis* 25S rRNA. Total RNA was extracted from roots of 7-day old plants, or whole seedlings, using the RNeasy Plant Mini kit with an

on-column DNase treatment (Qiagen). The total RNA (1 µg) was ethanol precipitated with 1 pmol of a ^{32}P-labeled DNA primer or 10 pmol of fluorescent DY782-labeled primer (Data S11) and annealed by heating to 95°C followed by slow cooling to 50°C. Annealing was carried out in 50 mM Tris-HCl (pH 8.3), 50 mM KCl, 1 mM EDTA. For extension, samples were adjusted to 50 mM Tris-HCl (pH 8.3), 75 mM KCl, 3 mM $MgCl_2$, 10 mM DTT, 0.5 mM to 1 mM dNTPs, 50 µg/mL actinomycin D, 1 U/µL RiboLock, 2 U/µL MashUp-RT (*62*). Extension reactions were incubated at +60°C for 30 min and terminated at 85°C for 5 min. After extension, template RNA was digested with RNase H and RNase A and the reactions were purified by phenol-chloroform (pH 7) extraction and ethanol precipitation. Extension products were analyzed on a 9% urea-polyacrylamide gel together with a sequencing ladder generated with the labelled primer and dideoxy chain termination method from a synthetic plasmid containing a 2000 bp fragment of the 3' end of *Arabidopsis* 25S rRNA gene. With reactions using ^{32}P labeled primer, the gel was dried, exposed on an imaging plate and scanned using Sapphire FL Biomolecular Imager and 638 nm laser and 424 nm shortpass filter. With DY782-labeled primer the gel was directly scanned with Sapphire FL Biomolecular Imager using 784 nm IR-laser and 829/62 nm filter. Quantification was done using AIDA software (Elysia Raytest).

For *in vitro* transcription of the synthetic *Arabidopsis* rRNA, a 1457 bp DNA fragment was first amplified using a forward primer flanked with a T7 promoter and a reverse primer that anneals to the 3' end of the 25S rDNA (Data S11). The resulting DNA fragment was used in *in vitro* transcription reaction with in-house purified T7 RNA polymerase in 1× transcription buffer [120 mM HEPES-KOH (pH 7.5), 24 mM $MgCl_2$, 20 mM DTT, 1 mM spermidine], supplemented with 5 mM each NTP, 1 U/µL RNase inhibitor, and 1.5 U/µL T7 polymerase. Transcripts were purified by phenol–chloroform extraction and ethanol precipitation.

For the *in vitro* methylation, the *in vitro* transcribed synthetic rRNA was used at a final concentration of 0.375 µM in 25 µL reactions containing 0.5 mM *S*-adenosylmethionine (SAM) and 1 mM recombinant OVAC protein or its SAM-binding deficient, inactive mutant (OVAC-mut carrying G335A, G339A mutations), in 1× methylation buffer [50 mM Tris-HCl (pH 8.0), 50 mM NaCl, 10 mM $MgCl_2$, 10 mM DTT, 0.5 U/µL RNase inhibitor]. Reactions were incubated at 25 °C for 2 hours and purified by phenol–chloroform extraction and ethanol precipitation. Methylation was assessed by primer extension as described above.

Plant protein extraction and immunoblotting

Roots of 7-day old seedlings were harvested and ground in liquid nitrogen. Total proteins were extracted as described in (*63*). Protein concentrations were determined using a Detergent Compatible assay (Bio-Rad), equal amounts (70 µg total protein) resolved by SDS-PAGE and subjected to immunoblotting using standard procedures. The immunoblots were probed with a monoclonal Anti-FLAG M2 primary antibody

(Sigma #F-1804), and signal detected using enhanced chemiluminescence with a Goat Anti-Mouse IgG (H + L)-HRP Conjugate secondary antibody (BioRad #1706516).

Ribosome footprinting along with transcriptomics

Ribosome footprinting analyzes of the *ovac-2* and wild type with and without thermospermine have been performed using the Illumina Ribo-Seq kit with a few modifications. Samples were grown on mesh on half-strength MS media for 7 days and incubated in 100 µM thermospermine-containing or mock liquid media for 10 hours in the treatment rounds, 10 hours is sufficient to upregulate the *SAC51* translational fusion reporter (p*SAC51*::*SAC51 5'leader*::*n3GFP*). If not treated, samples were harvested from the mesh after 7 days. We collected about 1/3rd of the root for each experiment and shock froze the samples before grinding them to a fine powder without letting them thaw. The first analysis was performed as follows: 1.6 mL powder was mixed with Polysome extraction buffer (10.2 mL H_2O, 280 mg deoxycholic acid, 2.8 mL 20% polyoxyethylene-10-tridecylether, 5.6 mL 1M Tris-HCl pH 8, 700 µL 2M KCl, 700 µL 1M $MgCl_2$, 28 µL 1mM DTT, 28 µL 100 mg/mL CHX, 28 µL 2 u/µL DNase TURBO as in (*64*)). We concentrated the buffer higher because water crystals developed during harvesting diluting the samples. Samples were incubated by shaking for 10 min on ice and centrifuged for 12 min at 4 °C and 14 000 rpm. The supernatant was separated into one aliquot for total RNA (100 µL) and one aliquot for footprint RNA (400 µL). 10 µL 10% SDS were added to the total RNA sample and stored for RNA extraction at a later point on ice or at -80°C. We followed the Ribo-Seq protocol from Illumina. For monosome collection, we used microspin S-400 columns washed with equilibration buffer (75 mL H_2O, 20 mL 1M Tris-HCl pH 8, 2.5 mL 2M KCl, 2.5 mL 1M $MgCl_2$) on a vacuum manifold. We purified the RNA with RNA Clean and Concentrator kits (T-25 and T5 for the later stages) from Zymo and removed rRNA with the Illumina RiboZero root kit. Footprint RNA was cut out from a 15% urea polyacrylamide gel and libraries were cut out and purified from a 10% TBE Polyacrylamide gel and diluted to 10nM in a pool for sequencing.

Data analysis ribosome footprinting: We used the TAIR10 genome sequence, the Araport11 genebuild, and ncRNA sequences downloaded from the ENSEMBLPlants FTP site https://plants.ensembl.org/info/data/ftp/index.html. Adapter and quality trimming were performed with FASTP (*65*). Quality control was performed with FASTQC and MultiQC. Sequences mapping to different ncRNA populations were identified using bowtie2 and removed from the dataset (*59*). The remaining reads were aligned with the TAIR 10 genome sequence using STAR (*66*). Read count matrices were generated from the alignment and the counts were subsequently adjusted to FPKM values. Pearson correlation coefficients among biological replicates of RNA-seq and ribosome footprinting (fig. S5, A and B) were calculated from FPKM values using R. Read length distribution, P-site position, and three-nucleotide periodicity were analyzed with the RibosomeProfilingQC package in R (fig. S5, C to E) (*67*). We used edgeR's classic quantile-adjusted conditional maximum likelihood method (qCML) to compute differential

transcription measurements (*68*). Translation efficiency is calculated as ratio between counts derived from ribosome footprints and RNA-seq. edgeR was used to identify significant ($p<0.05$) up- or downregulation in translation efficiency in each condition. To identify genes with uORFs whose translation is altered by thermospermine treatment in the wild type but not in *ovac*, we selected uORF-containing transcripts (*69*) that showed significant changes in translation between wild-type plants with and without thermospermine treatment but exhibited no significant changes in *ovac* under the same conditions.

Ribosome purifications for cryo-electron microscopy (Cryo-EM)

Roots of 6-day-old *Arabidopsis* seedlings were harvested in liquid nitrogen, and ribosomes were purified as follows. Frozen root powder was suspended in 2.3 volumes of ice-cold lysis buffer (modified from (*64*))(200 mM Tris, pH 8.8, 200 mM KCl, 36 mM $MgCl_2$, 1% Triton-X100, 1% Brij 35, 1% Tween-40, 1% NP-40, 1 mM DTT, 1 mg/mL heparin, 2% PTE, 1% Deoxycholate, Complete protease inhibitor) in an ice-cold mortar, and ground until achieving liquid consistency. The lysate was incubated on ice for 1-1.5 hours and centrifuged through a QiaShredder (Qiagen) column (1 min, 14000 rpm, 4°C) to remove cellular debris. The flow through was collected, incubated on ice for 5 min, and clarified by centrifugation (10 min, 12,000 g, 4°C). The supernatant was collected, layered at 1:1 ratio over Plant Sucrose Cushion (400 mM Tris, pH 8.8, 35 mM $MgCl_2$, 200 mM NaCl, 1 mM DTT, 1.75 M sucrose, Complete protease inhibitor) and centrifuged overnight (either 18 hours 20 min, 50 000 rpm, 4°C, S55-S rotor, or 18 hours, 41 000 rpm, 4°C, AH650 rotor). The pellet was carefully rinsed with ice-cold water and resuspended into Final Ribosome Buffer (50 mM Hepes, pH 7.4, 5 mM MgAc, 100 mM KAc, pH 7.5, 1 mM DTT, Complete protease inhibitor) on ice for 5 hours.

To transform the polysomes into monosomes, 1 mM $CaCl_2$ and micrococcal nuclease (0.15 U/µL) were added. The reaction was incubated in a 25°C water bath for 7 min, transferred on ice, and the nuclease was inactivated by adding 2 mM EGTA. To remove any remaining particles, the sample was centrifuged for 10 min at 20,000 g, 4°C, and the supernatant was collected.

Monosomes were purified using size-exclusion chromatography. The gel filtration column with 1 mL bed volume of Sephacryl S300HR (GE Healthcare) was equilibrated with Final Ribosome Buffer. The sample was loaded, and the column ran with the Final Ribosome Buffer. Fractions were collected manually, and their concentration was determined by measuring A_{260} with Nanodrop.

Cryo-EM sample preparation, data collection, and processing

4 µL of purified *Arabidopsis* 80S ribosomes were deposited on a graphene-coated Quantifoil R2/2 300 mesh copper grid (Graphenea) functionalized with 1-pyrenemethylamine (Sigma-Aldrich) (*8*) and incubated for 30 s in a Vitrobot Mark IV device set at 4 °C and 100% humidity. Excess liquid was blotted at force -7 for 1s, the grid was plunge-frozen in liquid ethane and stored in liquid nitrogen. Datasets were

collected using EPU (Thermo Fisher Scientific) on a Titan Krios microscope equipped with either a TFS Falcon4i or a Gatan K3 detector (Data S9) operating in fast data collection mode. Pre-processing (up to particle extraction stage) was either performed in cryoSPARC (*70*) using patch motion correction and patch ctf correction or in RELION (*71*) using MotionCor2 (*72*) and CTFFIND (*73*) and extracted particles were then imported in cryoSPARC where a combination of ab initio reconstruction and heterogeneous refinement was used to remove 'junk' particles. CryoDRGN (*74*) was used to represent the heterogeneity of 40S rotation states and tRNA-bound states. 40S-rotated and P-site bound ribosomes were of particular interest as they showed a well-defined peptidyl transferase center featuring clear signal for the CCA end of the tRNA as well as the nascent peptide backbone in the exit tunnel. Selected particles were filtered in cryoSPARC and a round of masked 3D classification focusing on the P-site tRNA was run to select for highly homogeneous particles. This final set of particles was used for homogeneous refinement in cryoSPARC with all global parameters refinement as well as per-particle defocus refinement enabled. Where the entire data processing had been performed in cryoSPARC, this was followed by a reference-based motion correction step (*75*). Where pre-processing had been performed in RELION, selected particles were compiled into a star file using pyem software (*76*) to perform bayesian polishing in RELION and subsequently re-imported into cryoSPARC. In both cases, a round of homogeneous refinement was then run in cryoSPARC with the same parameters as above to generate the final map. The structure of the WT tSpm- ribosome sample was first built in Coot (*77*), using the deposited 8b2l pdb model as an initial template. Refmac/Servalcat (*78*) was used for structure refinement and generation of the map-to-model FSC curves. The resulting model was then fitted into maps obtained for other samples and manually rebuilt where appropriate. All ligands were positioned and refined manually in Coot. As the maps represent an average of extracted actively translating ribosomes, mRNA was modelled as a poly-U chain and nascent peptide as a poly-A chain. The P- and E-tRNAs were represented as Phe (GAA) tRNA since its structure had previously been determined in pdb 8b2l. Prior to the final structure refinement in Refmac, a round of real-space refinement in Phenix (*79*) was performed to optimize protein and RNA geometry. Figures were generated in ChimeraX (*80*).

Ribosome profiling and polysome proteomics

Samples were grown on mesh on half-MS for 7 days and 1/3rd of the root was harvested and shock-frozen in liquid nitrogen. Samples were ground to a fine powder without allowing to thaw. 750 µL tissue was mixed with the same amount of polysome extraction buffer (1 mL 2M Tris pH 9, 1 mL 2M KCl, 500 µL 0.5M EGTA pH 8.3, 360 µL 1M $MgCl_2$, 7.14 mL H_2O, 80 µL β-mercaptoethanol, 10 µL 50 mg/mL CHX, 10 µL 50 mg/mL Chloramphenicol, 500 µL 20% detergent mix (20% (w/v or v/v) of each Brij-35, Triton X-100, Igepal, CA 630, Tween 20 in water), 1mL 2% polyoxyethylene-10-tridecylether 10% Deoxycholic acid, 10 mg heparin, in a total volume of 10 mL) and kept on ice for 10 min with occasional inversion.

Samples were centrifuged for 2 min at 14,000 rpm at 4°C and the supernatant was purified through QiaShedder columns (700 µL column). 700 µL sample was layered on a sucrose gradient (18% 2.0 mL, 26% 1.9 mL, 34% 1.9 mL, 42% 1.9 mL, 50% 1.9 mL, 60% 0.5 mL in gradient buffer pH 8.4 (50 mL 10x buffer contain 2.43 g Trizma base, 0.75 g KCl, 1.02 g $MgCl_2$ with 50 µL 50 mg/mL CHX and 50 mg heparin), centrifuged for 90 min at 275,000 *g* and fractionated into 14 microtubes (sensitivity 1.0, flow rate 1.5 mL/min). The polysomal fractions 7-9 were combined and sent for MS analysis.

For the MS analysis, the disulfide bonds were reduced with dithiothreitol (final concentration 5 mmol/L; Sigma-Aldrich, St. Louis, MO), and the cysteine residues were carbamidomethylated with iodoacetamide (final concentration 15 mM; Sigma-Aldrich, St. Louis, MO). The proteins were digested with 2.5 µg of sequencing-grade modified trypsin (Promega, Madison, WI). The resulting peptides were purified with C18 MicroSpin columns (The Nest Group, Inc., Ipswich, MA). After C18 purification, the samples were evaporated to dryness with a vacuum centrifuge and stored at − 20°C. Prior to LC–MS analysis, the samples were re-solubilized with 15 min sonication in 30 µL of 1% acetonitrile + 0.1% trifluoroacetic acid in LC–MS grade water (all from VWR, Radnor, PA).

The MS analysis was performed on a Q-Exactive mass spectrometer using Xcalibur version 3.0.63 coupled with an EASY-nLC 1000 system via an electrospray ionization sprayer (Thermo Fisher Scientific). In detail, peptides (10% sample) were eluted and separated with a C18 precolumn (Acclaim PepMap 100, 75 µm x 2 cm, 3 µm, 100 Å, Thermo Scientific) and analytical column (Acclaim PepMap RSLC, 75 µm × 15 cm, 2 µm, 100 Å; Thermo Scientific), using a 120-min linear gradient and detected with a Q-Exactive MS (Thermo Scientific) using top10 data-dependent acquisition, in which the 10 most intense ions from each MS1 full scan were fragmented and analyzed in MS2.

The *Arabidopsis thaliana* proteome from UniProt (UP000006548, retrieved 8.9.2025), supplemented with common contaminants and decoy sequences, was used for protein identification. Label-free quantification (MaxLFQ) (*81*) intensities were obtained from FragPipe output (Fragpipe v23.0, MSFragger v4.3) (*82*). Proteins identified in fewer than 3 samples were discarded. MaxLFQ intensities were $\log_2$-transformed, and missing values imputed using QRILC to approximate low-abundance signals. Differential protein abundance between WT and *ovac* samples (n = 5 biological replicates each) was assessed using two-sample t-tests applied to imputed $\log_2$ intensities with p-values adjusted by the Benjamini–Hochberg method. Adjusted p-values under 0.01 were considered significant, if $\log_2$ fold change between WT and *ovac* samples was either over 1 or under -1. Ribosomal proteins were identified by searching Quickgo (*83*) for cellular component ribosome (GO:0005840), and filtering with the qualifier "part_of". All analyses were performed in Python (v3.12) with pandas, numpy, statsmodels, scipy, matplotlib, and seaborn.

Molecular cloning and transformation

For initial complementation analyses, a genomic fragment spanning the *OVAC* locus and containing 489 bp of the sequence upstream of the transcriptional start was cloned as a 3100 bp Bam HI-Eco RI fragment into pGREEN1079 and introduced to *ovac-1 cre1-12 pAHP6:GFP*. The promoter region was limited to approximately 0.5 kb to avoid the flanking gene in the same orientation. *mOVAC* that harbors two point mutations within the RNA methyltransferase domain was created using QuikChange Lightning Multi Site-Directed Mutagenesis Kit (Agilent). *mOVAC* has R127 (CGT to GCT) and T310 (ACC to GCC) mutated into alanine, thus disrupting the two predicted active sites of the methyltransferase domain of OVAC.

For the *in vitro* transcription of *Arabidopsis* rRNA, and the dideoxy chain termination to generate a sequencing ladder, a synthetic 2000 bp fragment from the 3' end of the 25S rDNA was ordered ready-cloned in pUC19 vector (Twist Bioscience). For the OVAC protein purifications, the coding sequence was ordered tagged with MBP and ready-cloned in pET-28a(+) vector (Twist Bioscience) for expression in *E. coli*.

For the translation experiments in protoplasts, we created the pGreen2x35SLUC plasmid (Addgene plasmid #108228), produced by introducing into the plasmid backbone pGreenII0800-LUC(*84*) the 2x35S promoter sequence derived from plasmid pGJ1425(*85*). The 2x35S promoter was introduced at the 5' of the Firefly luciferase gene and separated by a polylinker sequence where the wild-type or mutant versions of the 5'-leader of the *SACL3* gene were cloned.

Other plasmids with genetic components originating from *Arabidopsis* were generated using the 3x Multisite Gateway (Invitrogen) system. The *OVAC* promoter was cloned by amplifying a 489 bp fragment upstream of the transcription site and inserting it into the pDONR-P41R entry vector. The coding sequence of *OVAC* was cloned as a 2392 bp genomic (or a 1412 bp cDNA) fragment into the pDONR-221 or the pDONR-P2rP3 entry vector. For transcriptional and translational fluorescent reporter constructs we used GUS/RFP (*86*) or GFP (*87*). The 3xFLAG tag was subcloned into the pDONR-221 entry vector from the pCI-neo-3x-FLAG vector (*88*), to subsequently generate plants expressing N-terminal 3xFLAG tagged recombinant proteins (OVAC or mOVAC) under the control of the *OVAC* promoter. Entry clones were recombined into destination vectors (pHm43GW, pBm43GW, or pFR7m34GW) by MultiSite Gateway LR reactions. To introduce *sacl* point mutations, the mutated *SACLs* gDNA (*36*) were cloned and transformed into wild type and the *ovac-2* background to avoid a Col-0/Ler hybrid.

To generate plants carrying three reporters (1. *pLHW*::*5'leader::n3mVenus*, *pLHW*::*mutated 5'leader*::*n3mTurq2*, and *pACL5*::*n3mScarlet-I;* 2. *pLHW*::*5'leader::n3mVenus*, *pSAC51::5'leader::n3mTurq2, pACL5*::*n3mScarlet-I;* 3. *pSAC51::SAC51 5'leader-LHW uORF::n3mVenus, pSAC51::SAC51 5'leader-SAC51 uORF::n3mTurq2, pSAC51::mutated SAC51 5'leader::n3mScarlet-I;* 4. *pLHW::LHW 5'leader-SAC51 uORF::n3mVenus, pLHW::LHW 5'leader-LHW uORF::n3mTurq2, pLHW::mutated LHW 5'leader::n3mScarlet-I*), the Golden Gate cloning system was used (*89*) . A 1717 bp fragment of the *LHW* promoter (excluding the 5'leader) and an 1811 bp fragment of

the *ACL5* promoter (including the 5'leader) were amplified from *Arabidopsis* genomic DNA. The *LHW* and *SAC51* 5'leader sequence was amplified from *Arabidopsis* cDNA, and a mutated version was generated by replacing the ATG start codon of its uORF with a TAG stop codon. Chimeric 5′ leaders were synthesized by Twist Bioscience: one in which the last uORF of the SAC51 5' leader was replaced with the LHW uORF, and another in which the LHW 5′leader uORF was substituted with the last uORF from SAC51. All sequences were domesticated for Golden Gate cloning by removing internal *BsaI* and *BpiI* restriction sites and cloned into Level 0 constructs, which were subsequently assembled into Level 1 and Level 2 constructs.

In the case of the *Homo sapiens* (human) *OVAC,* the coding sequence of *C9orf114* (RefSeq NM_016390) was synthesized (DNA2.0), and cloned into AvrII/MluI sites of the pCI-neo-3x-FLAG vector (*88*) to generate an N-terminal 3xFLAG tagged in vivo mammalian over-expression construct.

All transgenic lines were created by an *Agrobacterium*-mediated (strains GV3101, GV3101::pMP90), standard floral dip method (*90*). Seeds were selected on MS plates containing appropriate antibiotics (DL-Phosphinothricin (PPT), hygromycin) or based on a FastRed/FastGreen selection system (*91*). At least two or three independent lines were analyzed for each construct. We note that the N-terminal translational fusion protein eGFP-OVAC was non-functional, as it did not complement the *ovac* mutant phenotypes in any of the 13 individual transgenic lines generated.

Cell culture, transfection, and immunofluorescence

HEK293 cells were cultured in Dulbecco's modified Eagle's medium supplemented with 10% fetal bovine serum and 2 mM L-glutamine using standard procedures. To over-express C9orf114 protein in HEK293, cells were transiently transfected using Lipofectamine 2000 (Thermo) and 100-750 ng of the mammalian over-expression construct for 48 hours. To confirm C9orf114 over-expression in the transfected cells, lysates were prepared by adding Laemmli sample buffer to the cells and run on an SDS-PAGE followed by immunoblotting. Immunoblots were processed using standard procedures, using primary antibodies against the FLAG (Sigma M2, #F-1804) tag, and analyzed using enhanced chemiluminescence with an HRP-conjugated anti-mouse (Invitrogen #31430) secondary antibody. To analyze the cellular localization of 3xFLAG-C9orf114 in HEK293 cells by immunofluorescence, an anti-FLAG-GFP secondary antibody (Invitrogen #A-11122) was used. For imaging under a Leica SP8 confocal microscope, coverslips were mounted using ProLong Gold Antifade Mountant with DAPI (Thermo) to stain for DNA in the nuclei.

RT-PCR analyses of specific mRNAs

Total RNA was extracted using RNeasy Plant Mini kit (Qiagen) with DNase treatment to avoid genomic DNA contamination. cDNA was synthesized from 0.5-1 µg RNA with a cDNA synthesis kit using a mixture of Oligo dT and random hexamer primers (Roche). LightCycler SYBR Green master mix (Roche) was used in a LightCycler 480 device (Roche) following manufacturer's default program recommendations for

quantitative RT-PCR (qRT-PCR). *OVAC* and *ACL5* transcript levels were normalized to a respective housekeeping gene *PP2A*.

Protoplast assays, Luciferase firefly/Renilla

Protoplasts were obtained from leaf tissues and transiently transformed according to (*92*). The translation experiments in protoplasts were based on transient expression of dual-luciferase reporter assays(*93*). After protoplast transient expression of the different constructs, translation of the reporter Firefly luciferase was quantified using Renilla luciferase as a reference, which was insensitive to thermospermine treatments.

Tobacco infiltration

Tobacco (*Nicotiana benthamiana*) infiltration was performed following a previously published protocol (*94*). Briefly, *Agrobacterium tumefaciens* strain GV3101 was cultured overnight at 28 °C in 10 mL of LB medium supplemented with kanamycin (100 mg/L) and rifampicin (50 mg/L). Cultures were pelleted by centrifugation and resuspended in infiltration buffer (10 mM MES, pH 5.6, 10 mM $MgCl_2$, 200 μM acetosyringone) to an optical density ($OD_{600\ nm}$) of 0.8 ~ 0.9. Bacterial suspensions were infiltrated into the abaxial side of leaves from 4-week-old tobacco plants using a blunt-tipped 1 mL syringe. For thermospermine or mock treatments, 50 μM thermospermine or an equivalent volume of mock in infiltration buffer was infiltrated into the same leaf regions 24 hours after *Agrobacterium* infiltration using a blunt-tipped 1 mL syringe. Leaf tissues were collected 21 ~ 24 hours after thermospermine or mock treatment for confocal imaging. A total of five to nine infiltrated spots from two to three leaves were imaged per construct and condition.

Thermospermine measurements

Polyamine measurements were conducted using 21-day-old plants. Roots from 50 plants per biological replicate were collected, with three independent replicates generated. Polyamines were purified and quantified following the procedures described in 65,66.

Histology

Arabidopsis roots and hypocotyls were fixed and embedded in Historesin (Leica) as described (*97*, *98*). Cross sections were obtained using a rotary microtome (Leica). Before imaging, the sections were stained in 0.05% toluidine blue (and 0.05% ruthenium red, sequentially). Alternatively, the tissues were fixed and cleared using ClearSee (*99*) and stained with calcofluor white or with 0.1% (v/v) SCRI Renaissance 2200 (SR2200) stain before observing. Histochemical staining for GUS activity was carried out as described in (*100*). For vibratome sections, hypocotyls were fixed in 4% formaldehyde and embedded in 4% agarose following a protocol described in (*101*). Transverse sections were made by vibratome Leica VT1200S and

stained with 0.1% (v/v) SCRI Renaissance 2200 Stain and 0.05% Fuchsin stain before imaging by confocal microscope.

Confocal imaging for reporter expressions

For confocal imaging of root apical meristem with *SACL* reporters, 7-day-old seedlings were fixed in 4% formaldehyde, stained with SR2200 or propidium iodide, and cleared using ClearSee(*99*) prior to visualization. To assess *SAC51* and *LHW* translation in root tips and during secondary development, and to determine the half maximal inhibitory concentration for LHW translation, 6- or 7-day-old seedlings grown on half-strength MS medium were transferred to medium containing various concentrations of thermospermine indicated, 50 μM xylemin or a mock treatment and incubated for 24 hours. For SAC51 reporter expression analysis during secondary development and the half-maximal excitation concentration for SAC51 translation, seedlings were grown for 14 days on medium with various concentrations of thermospermine indicated, 50 μM xylemin or a mock treatment before processing. All seedlings were fixed in 4% formaldehyde, and roots from 14-day-old plants were sectioned at the hypocotyl-root junction by vibratome Leica VT1200S and stained with SR2200, while younger seedlings were directly stained and cleared before confocal imaging. Confocal images were acquired using a Leica TCS SP8 confocal microscope with a 63×/1.20 WATER objective for root tips and a 20×/0.70 DRY objective for cross-sections of the hypocotyl-root junction and the mature part of the roots, where *ACL5* expression is detected in xylem parenchyma and/or pericycle cells (fig. S13E). This region was selected because *ACL5* serves as a secondary xylem vessel marker, and xylem pole pericycle cells contribute to cambial development (*35*, *101*).

The image resolution was set to 512 x 512 or 1024 x 1024 pixels, with a z-step size of 1 μm. Excitation settings were 405 nm (SR2200 and calcofluor white), 488 nm (GFP), 514 nm (mVenus), or 561 nm (Fuchsin staining), while emission settings ranged 430 ~ 445 nm (SR2200 and calcofluor white), 496 ~ 521 nm (GFP), 525 ~ 555 nm (mVenus), and 590 ~ 615 nm (Fuchsin staining), respectively. To determine xylem vessel density per total cross-section area, the total cross-section area (including xylem, phloem and phelloderm) was measured using Fiji software (*102*) and the number of xylem vessels and total number of cells were either manually counted based on Fuchsin staining or counted using Cellpose (*103*). Segmentation and quantification of fluorescence intensity of nuclear-localized GFP (n3GFP), mVenus (n3mVenus), mScarlet-I (n3mScarlet), or mTurquise2 (n3mTurq) were performed on z-stacked 16-bit confocal images using FRETENATOR2 (*104*, *105*) plugin in Fiji software.

Supplementary Text

Identification of the *OVERACHIEVER*

In search of novel modifiers of cytokinin-mediated vascular patterning, known for its robustness in the *Arabidopsis* primary root (*106*), we performed an EMS mutagenesis screen for *pAHP6::GFP* misexpression in the cytokinin hyposensitive background, *cre1-12*. Given that the expression pattern of *AHP6* in the primary root is restricted to the protoxylem and the adjacent two pericycle cells only (*107*), it can be regarded as a highly specific marker of differentiating protoxylem. From the EMS screen, we selected a mutant named *overachiever* (*ovac*) that displayed an expanded *pAHP6::GFP* expression domain (fig. S1A). The *ovac-1* mutation is recessive, and the mutant plants are fertile and grow vigorously in optimal conditions (Fig. 1E). The expanded *AHP6* domain correlates with the presence of an excessive number of protoxylem cell files at the ends of the xylem axis in the *ovac-1 cre1-12* double mutant primary root (fig. S1B). Occasionally, we could see a full double axis of xylem cells (fig. S1B) which resembles the root phenotype reported for the cytokinin receptor double mutant *ahk3 cre1* (*107*). These phenotypic analyses suggest that OVAC may control xylem differentiation by spatially restricting cytokinin signaling via promoting *AHP6* expression. Based on quantitative analysis of the cross-sections, we found that the *ovac* single mutants showed normal primary vascular development but excessive formation of xylem vessels during secondary development (Fig. 1, C and D, and fig. S1A).

To identify the gene underlying the *ovac-1* mutant phenotype, we first performed whole-genome sequencing and rough mapping of the double mutant *ovac-1 cre1-12* (Materials and Methods). We discovered an early stop codon in the first exon of an uncharacterized, putative RNA methyltransferase gene (At5g19300), that resided within the mapping window of 1.5 Mb located in chromosome 5 (Fig. 1B). *OVAC* is a single copy gene that is conserved across the plant and animal kingdom. To confirm the gene identification, we tested for allelism and complemented the *ovac* mutant phenotype by transforming the At5g19300 full genomic context or coding sequence with 0.5 kb of the 5' region. 0.5 kb of the promoter region were sufficient to complement *ovac* (figs. S1A and S4E). To examine the cell-specific expression, we fused the 0.5 kb *OVAC* promoter that was sufficient for complementation with *GUS/RFP,* and observed the reporter construct in plants. *OVAC* is highly expressed in the root tip, emerging lateral roots and the root/hypocotyl junction (fig. S1C). In cross-sections of the hypocotyl, *OVAC* is expressed in xylem parenchyma cells (fig. S1D). Homology modelling of the OVAC protein sequence showed 47% and 32% identity to a human 4rg1B (C9orf114), that we confirmed to localize to the nucleolus (fig. S2C)(40), and a *Methanobacterium* methyltransferase 1k3rB, respectively. These proteins are representatives of the Archaea and Eukaryota protein family COG2106 and characterized by a conserved, putative RNA methyltransferase domain with a putative RNA-binding OB-fold domain inserted in the middle (*22*).

In vitro **reconstitution of the 25S rRNA m^{3}U2952 modification reaction**

We used *in vitro* reconstitution to define the minimal conditions required for the m^{3}U2952 modification. For this, we set up a primer extension analysis (fig. S3A) to identify methylated and

unmethylated U2952 residues on rRNA at one-nucleotide resolution. Primer extension reaction is a widely used method for mapping modified nucleotides, particularly 2'-O-methylation on rRNA (*108*) but can be used for other modifications on any RNA. m^3U modifications have been shown to generate strong primer extension stop bands because of its incompatibility as base-pairing partner in unmodified RNA or DNA duplex (*30*). We initially confirmed the functionality of the assay by analyzing the U2952 modifications from total RNA pools derived from WT and *ovac-2* plants. We observed a strong primer extension stop one nucleotide preceding the modified nucleotide with WT but not *ovac-2* total RNA pool (fig. S3B) confirming the location of the m^3U modification. In repeated experiments this main primer extension stop was frequently followed by weaker bands of variable intensity, known to result from polymerase "stuttering" reaction where 1-2 untemplated nucleotides are added after pausing of the polymerase (*108*).

For *in vitro* reconstitutions, we used recombinant catalytically active WT methyltransferase (OVAC-WT) and a catalytically inactive version of the enzyme (OVAC-mut) (fig. S3C). The G335A and G339A substitutions in OVAC-mut are expected to disrupt the binding to cofactor *S*-adenosyl methionine (SAM) and render the enzyme catalytically inactive. The inactivating mutations were designed based on the earlier work on *Drosophila* ortholog (*30*). As a substrate for m^3U modification we used *in vitro* transcription with T7 RNA polymerase to produce unmodified 1475 nt 3' fragment of the *Arabidopsis* rRNA. In the presence of SAM, only the OVAC-WT but not OVAC-mut was able to methylate the U2952 position of the synthetic RNA (Fig. 1H), identifying the minimal conditions for the m^3U2952 modification.

Ribosome profiling and RNA-seq analyses of *Arabidopsis* roots

We performed ribosome profiling and RNA-seq analyses of roots to assess both translational regulation and transcript abundance across different genotypes and treatments. To identify genes with altered translational efficiency, we calculated the ratio of ribosome footprint counts to RNA-seq counts and applied edgeR to detect significant changes (FDR < 0.05) in up- or downregulation (|logFC| > 0.5) under each condition (fig. S6 and Data S4 to S7).

Through the comparisons, we identified genes that responded consistently across analyses. As described in the main text, three genes (*SAC51*, *SACL2*, and *SACL3*) showed reduced translation in *ovac* (with or without thermospermine treatment) relative to corresponding wild-type controls but were upregulated by thermospermine only in wild type (fig. S6B). Conversely, one gene (AT4G30960) was upregulated in *ovac* compared to wild type but downregulated by thermospermine in wild type (fig. S6B). In addition, five genes (GBF5, GBF6, VTC2, VTC5, and AT5G41990) showed no response to thermospermine in wild type but exhibited altered translation specifically in *ovac* under both treated and untreated conditions comparing to wild type (fig. S6B), suggesting OVAC-specific regulation. There are four additional genes whose translation was altered in the same direction in both the *ovac* vs. wild type and the thermospermine-treated wild type vs. mock-treated wild type (fig. S6B). Given that *ovac* mutant has an

increased amount of thermospermine (fig. S18, A and B), these genes are potentially regulated in their translation by thermospermine alone. For instance, Polyamine oxidase 4, a polyamine catalytic enzyme, is upregulated in its translation in both contexts, implying that high amount of polyamine induces its catabolism as reported previously (*109*, *110*). We therefore regard these 13 genes of 30 genes as direct impacted translation by OVAC and/or tSpm.

Beyond these, we identified 186 genes (35 genes upregulated and 151 genes downregulated), including LHW, that were altered in their translation by thermospermine in wild type but not in *ovac* (fig. S6B). As we validated that LHW translation is downregulated by thermospermine in wild type, but not to the same extent in *ovac*, this indicates that LHW regulation also depends on OVAC and thermospermine. It is possible that additional genes among this set of 186 are similarly regulated. It is also possible that the differential regulation by tSpm of many of the remaining 186 genes and 17 genes (*ovac* vs. WT comparison) more likely reflects indirect effects, arising from altered cell fate decisions or downstream consequences of misregulated translation of key transcription factors such as SACLs and LHW, which are central regulators of vascular development.

Finally, unlike other *SACL* genes, we observed that *SAC51* and *LHW* transcript abundance appears to be altered by thermospermine treatment in wild type (increased or decreased, respectively) but not in *ovac* (fig. S8B, S9 and S10). Because their translation is significantly up- or downregulated by thermospermine only in wild type, we consider it plausible that the observed transcript abundance changes are coupled to, or arise as a consequence of, altered translational efficiency.

Phenotypic recovery of *ovac* by the mutations in SACLs, RPL4, and LHW

The thermospermine biosynthetic locus *ACL5* was identified based on a loss-of-function mutation causing a severely stunted phenotype and excessive xylem vessel formation (*39*). Three types of mutations can suppress this phenotype: (1) point mutations in the inhibitory uORF sequences of *SAC51* and *SACL* genes (*36*, *38*), (2) mutations in the ribosomal proteins LARGE SUBUNIT RIBOSOMAL PROTEIN 10 (RPL10) (*111*) and RPL4 (*41*), and (3) T-DNA insertion in *LHW* (*36*). These data suggested that the inhibitory interaction between the SACL uORF peptides and ribosomes results in substantial reduction in SACL translation in *acl5*. Furthermore, reducing LONESOME-HIGHWAY/TARGET-OF-MONOPTEROS5 heterodimerization through a *lhw* mutation in *acl5* can compensate for the defective *SACL*s translation in *acl5* (*36*, *37*). We investigated whether these mutations rescue *ovac* phenotypes. The uORF point mutation alleles, *sacl3-10, sacl3-31,* and *sac51-104*, significantly suppress the excessive vessel differentiation in *ovac*, restoring it to the wild type level ($n = 37 \sim 54$ per each line of *ovac sacl3-10* and *ovac sac51-104,* and $n = 4 \sim 8$ per each line of *ovac sacl3-31*, fig. S11, A to E), and markedly rescue the shoot phenotype in *ovac* ($n = 3$ for wild type, *ovac*, *ovac SAC51*, and *ovac sac51-104*, fig. S11F). The *sac56-d* introduces a G75R mutation within the RPL4 tentacle that contributes to the central ribosomal exit tunnel wall constriction

(*41*). In the *ovac*, *sac56-d* (*41*) partially restored the xylem differentiation (39.9 ± 3.07% recovery toward wild-type level compared to the *ovac* mutant; mean ± SE, *n = 34 ~ 42* per each genotype, fig. S5E) and shoot phenotype (*n* = 12 plants for *ovac-2 sac56-d* and *ovac-2*, fig. S11, G and H). Furthermore, we also observed that the *lhw* mutation can partially rescue the xylem vessel differentiation phenotype of *ovac,* with a recovery of 40.1 ± 6.93% toward wild-type levels (mean ± SE, *n = 18 ~ 25* per each genotype, fig. S11I). We interpret that the partial rescue in these cases may be due to a weak nature of mutation in *rpl4* or existence of redundant gene functions in *lhw*. Given that *LHW* translational suppression is impaired in *ovac* (Figs. 2, A, D and E, 4D, and S20, E to I), we concluded that the excessive xylem vessel differentiation in *ovac* is caused by defective *SACL* translation and impaired *LHW* translational suppression.

Analysis of bifunctional translational regulation of *SACL*s and *LHW*

To validate the ribosome footprinting data (Fig. 2A), we examined expression of translational reporters of *SAC51*, *SACL1*, *SACL2*, *SACL3* and *LHW* with and/or without thermospermine treatment. Analysis of translational reporters containing the uORFs without treatment confirmed that the translation of all *SACL* genes was inhibited in *ovac* compared to wild type (Fig. 2B). In wild-type root tip, thermospermine significantly enhanced the expression of *SAC51* uORF fusion reporter but not in the *ovac* mutant (Fig. 2C). However, no visible changes were detected in *SAC51* transcriptional reporter expression in the *ovac* in response to thermospermine (Fig. 2C). Dual-luciferase assays on various gene forms of *SACL3* with wild-type and *ovac* leaf protoplasts confirmed enhanced translation of *SACL3* upon thermospermine treatment in wild type but not in *ovac* (fig. S7, A and B). The *sacl3-31* dominant mutation (*36*) facilitated translation in both wild type and *ovac*, however, thermospermine treatment further enhanced translation only in wild type (fig. S7, A and B).

Since the *LHW* transcription is downregulated in the *ovac* compared to wild type (Fig. 2, D and E), we generated transgenic plants carrying two fluorescence reporters: one fused with the native *LHW* uORF and another with a mutated uORF where its start codon was replaced by a stop codon to remove regulatory effect of uORF (*112*), allowing calculation of translation efficiency based on fluorescence intensity considering the transcriptional differences. Thermospermine treatment significantly reduced *LHW* translation efficiency in root tip of both genotypes, but it remained higher in *ovac* than in the wild type (Fig. 2, D and E). A two-way ANOVA test showed that there was a significant interaction between the effects of thermospermine and the OVAC-mediated methylation on *LHW* translation efficiency (p = 2.2e-16). The thermospermine-induced downregulation of *LHW* translation efficiency was significantly greater in the wild type than in *ovac* (Fig. 2, D and E). However, the overall expression of *LHW* is downregulated in the *ovac* compared to the wild type due to the reduced transcription (Fig. 2, D and E).

To investigate the translation of *SAC51* and *LHW* reporters during secondary development, we grew plants on media supplemented with thermospermine and/or xylemin for 14 days. Unlike in the root

tip, where *SAC51* transcription levels did not differ between wild-type and *ovac* (Fig. 2C), we observed a significant reduction in *SAC51* transcriptional reporter expression in *ovac* compared to wild type during secondary growth (fig. S19, B and C). However, the translational decline in *ovac* was significantly pronounced than the reduction in the transcriptional reporter expression across all conditions (fig. S19D), confirming that *SAC51* translation is impaired in *ovac* relative to wild type during secondary development. Notably, while *SAC51* transcription remained unchanged in *ovac* upon xylemin treatment compared to untreated *ovac*, *SAC51* translation was abolished in xylemin-treated *ovac*, as indicated by the absence of detectable fluorescence (Fig. 4C and fig. S19, A to C). Furthermore, co-application of xylemin and thermospermine in *ovac* restored *SAC51* translation (fig. S19, A to D), vessel differentiation, and growth to levels comparable to untreated *ovac* (fig. S19, E to G). In contrast, the same treatment in wild type resulted in a substantial increase in *SAC51* translation, leading to severe inhibition of vessel differentiation (Fig. 4C and fig. S19, A to C). These findings confirm that the functional binding of thermospermine to the methylated ribosome is essential for the maximal induction of *SAC51* translation (Fig. 4E).

For LHW, 14-day thermospermine treatment confirmed its role in repressing *LHW* translation in wild type, consistent with observations from primary development in root tips (Fig. 2, D and E, and S20, A to D). However, 14-day xylemin treatment significantly reduced *LHW* transcription in wild-type xylem tissue (fig. S20A), preventing an accurate assessment of translation efficiency during secondary xylem development under these conditions. To circumvent this limitation, we conducted a 24-hour treatment and examined mature roots, focusing on vascular cells and xylem pole pericycle cells, where the secondary xylem vessel marker *ACL5* is expressed (*35*). Unlike in the root tip (Fig. 2, D and E), *LHW* translation efficiency was higher in both *ovac* and *acl5* mutants compared to wild type (Fig. 4D and fig. S20, E to I), confirming that OVAC-mediated methylation is necessary for translational inhibition of *LHW*. Moreover, *LHW* translation efficiency was higher in *ovac* than in *acl5*, indicating that OVAC-mediated methylation itself exerts an additional inhibitory effect on *LHW* translation independently of thermospermine binding in mature roots. Thermospermine treatment reduced the *LHW* translation efficiency in *acl5*, *ovac*, and wild type, although the *ovac* mutant retained a relatively higher translation efficiency compared to both wild type and *acl5,* consistent with findings from root tips (Fig. 4, C and D, and fig. S20, E to I). These results confirm that the maximal suppression of *LHW* translation requires functional binding of thermospermine to methylated ribosome (Fig. 4E).

Finally, to further validate that m^3U2952-mediated bifunctional roles of thermospermine in *LHW* and *SAC51* translation, we examined their translation in the mature part of wild-type and *ovac* roots with or without thermospermine treatment (fig. S7, C and D). Consistently, we observed that the *ovac* mutant exhibits significantly reduced *SAC51*-to-*LHW* translation ratio in response to thermospermine, compared to wild type (fig. S7, C and D). These results confirmed that the bifunctional regulation of thermospermine depends on its m^3U2952-promoted binding to the ribosome.

Elevated LHW expression in *acl5* causes exaggerated vessel differentiation compared to *ovac*

We found that overall *LHW* expression was significantly higher in *acl5* than in *ovac* due to decreased LHW transcription in *ovac* (fig. S20, F and G), despite *LHW* translation efficiency in *acl5* was not higher than in *ovac* (Fig. 4D). Consistent with this, *acl5* mutants displayed an increased proportion of vessels relative to total cells and cross-sectional area compared to *ovac* (fig. S22, A to D). Moreover, increasing expression of *LHW* by introducing a mutated uORF-fused *LHW* in *ovac* significantly enhanced vessel differentiation and caused severe dwarfism, phenocopying the *acl5* (fig. S22, C to E). Taken together, these findings indicate that the more severe vessel differentiation phenotype observed in *acl5* compared to *ovac* is primarily attributed to the higher *LHW* expression in the absence of thermospermine production.

Supplementary Figures

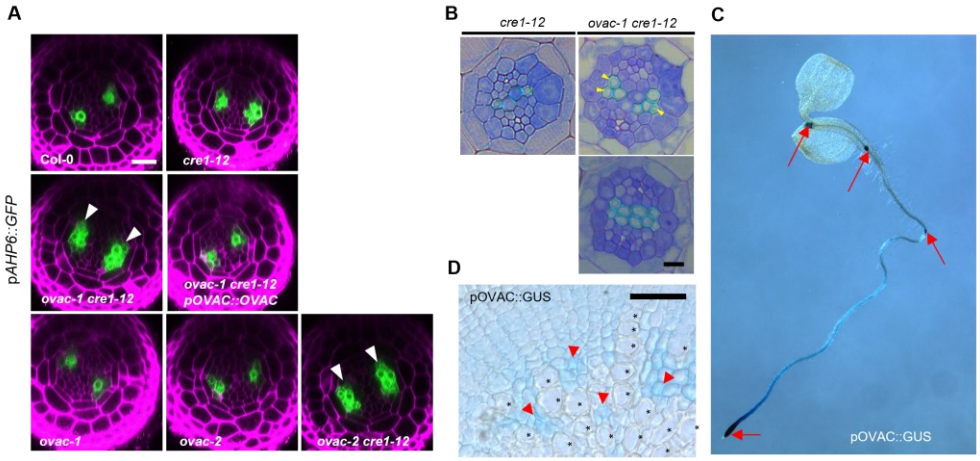


Fig. S1. Identification and characterization of OVAC.

(**A**) Confocal optical cross-sections show typical *pAHP6::GFP* expression in the primary root in various genetic backgrounds. Arrowheads indicate an expanded *pAHP6::GFP* domain in the double mutant *ovac-1 cre1-12* and *ovac-2 cre1-12*. Roots were counter-stained with propidium iodide. Scale bar, 20 µm. (**B**) histological sections of primary roots. Protoxylem is indicated with arrowheads. Sections were stained with toluidine blue. Scale bar, 10 µm. (**C**) expression pattern of *OVAC*, illustrated by GUS staining of a 4-day-old seedling. Arrows point at the shoot apex, root/hypocotyl junction, lateral root primordium, and the root tip. (**D**) cross-section of 33-day-old hypocotyl with GUS staining. Black asterisks and red arrows indicate differentiated vessels and xylem parenchyma cells, respectively. Plants were grown under short-day conditions (9 hours/15 hours, light/dark). Scale bar, 20 µm.

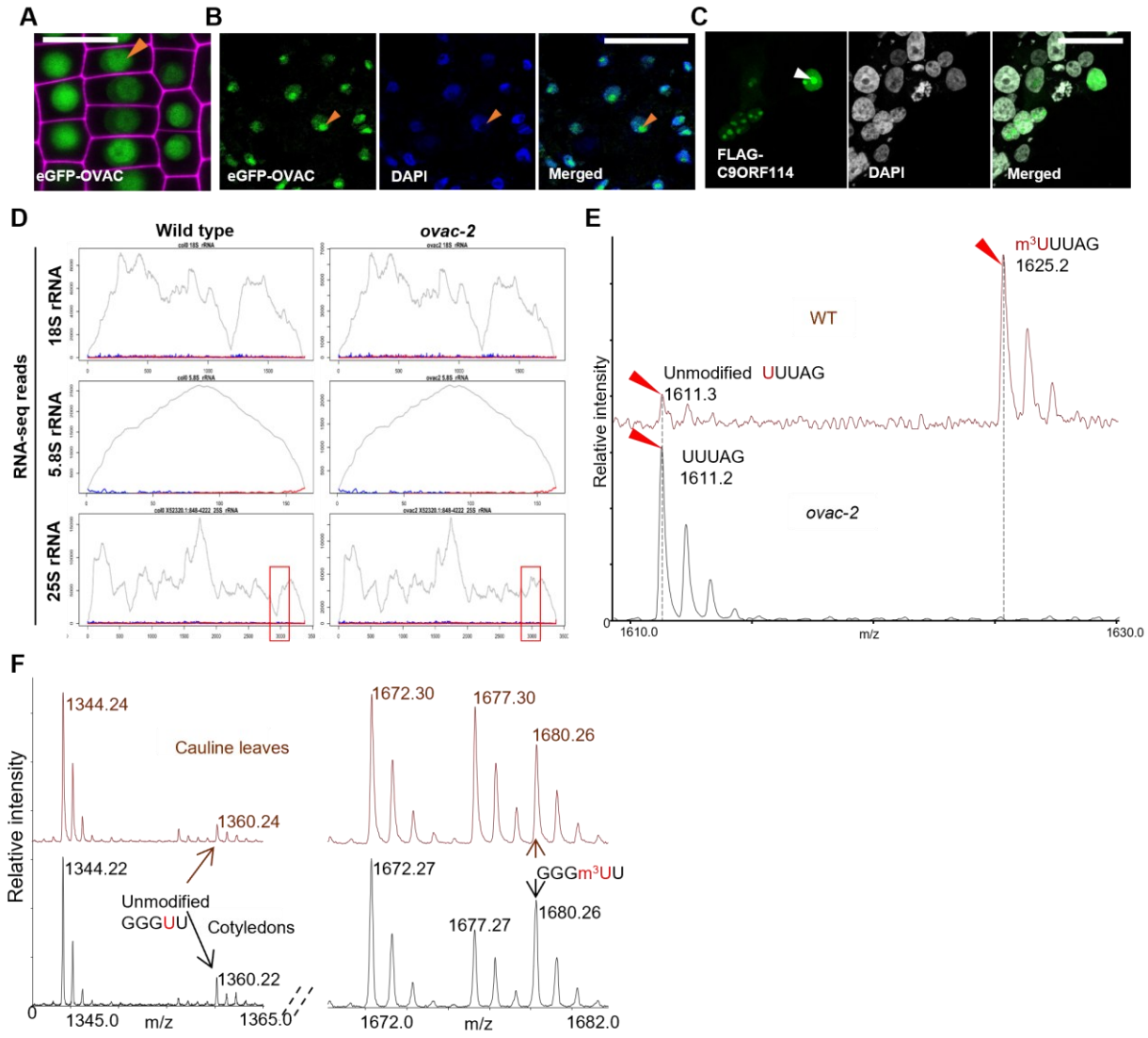


Fig. S2. m^{3}U2952 modification by OVAC.

(**A and B**) Cellular localization of the OVAC protein (p*OVAC*::*eGFP*::*OVAC*) in the root meristem (**A**) and leaves (**B**). The orange arrowhead indicates the nucleolar localization of the protein. Roots were stained with propidium iodide and leaves were stained with DAPI. Scale bar, 20 µm. (**C**) Protein localization of C9orf114, the human ortholog of *OVAC*, in HEK293 cells. Scale bar, 20 µm. (**D**) RNA-seq read counts of *Arabidopsis* rRNA species in WT and the *ovac-2* mutant. The red-boxed region contains the residue U2952 in the 25S rRNA. (**E**) Mass spectrometric analysis of an RNase T1-digested 25S rRNA sub-fragment from WT (top) and *ovac*-2 (bottom) roots, focusing on m/z region relevant for U2952 methylation (red letters and arrowheads). (**F**) Mass spectrometric analysis of an RNase A digested 25S rRNA sub-fragment from cauline leaves (upper red graph) or cotyledons (bottom black graph) of the WT, showing only the m/z ranges relevant for the U2952 modification.

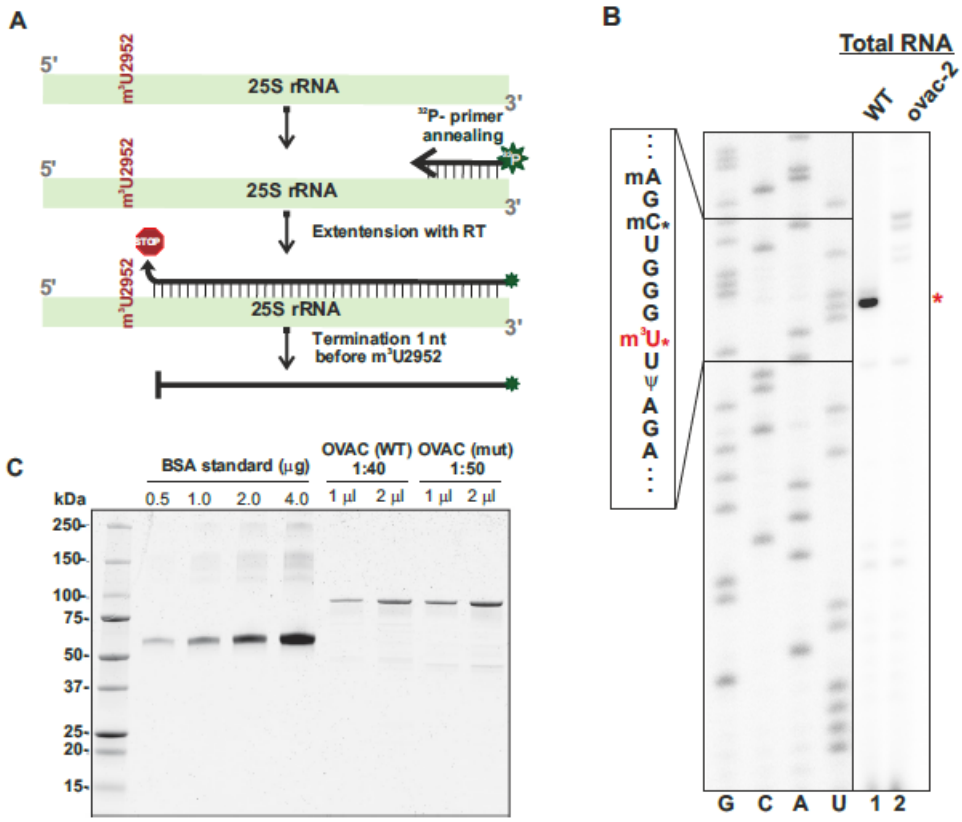


Fig. S3. Primer extension analysis and recombinant OVAC production for the *in vitro* reconstituted m^{3}U2952 modification reaction.

(**A**) Schematic illustration showing the principle of the primer extension analysis used for m^{3}U residue mapping. (**B**) Primer extension analysis of the m^{3}U2952 modification from *Arabidopsis* total RNA pools derived from WT and *ovac-2* plants. The first four lanes are a sequencing ladder. The primer extension stops corresponding to the U2952 (located one nucleotide before the modified nucleotide) is indicated with a red star on the right. Sequence track on the left also indicates the RNA modifications detected in this study by Cryo-EM. (**C**) SDS-PAGE showing the quantification of the purified MBP-tagged OVAC and OVAC-mut proteins together with a titration series of BSA used for concentration determination.

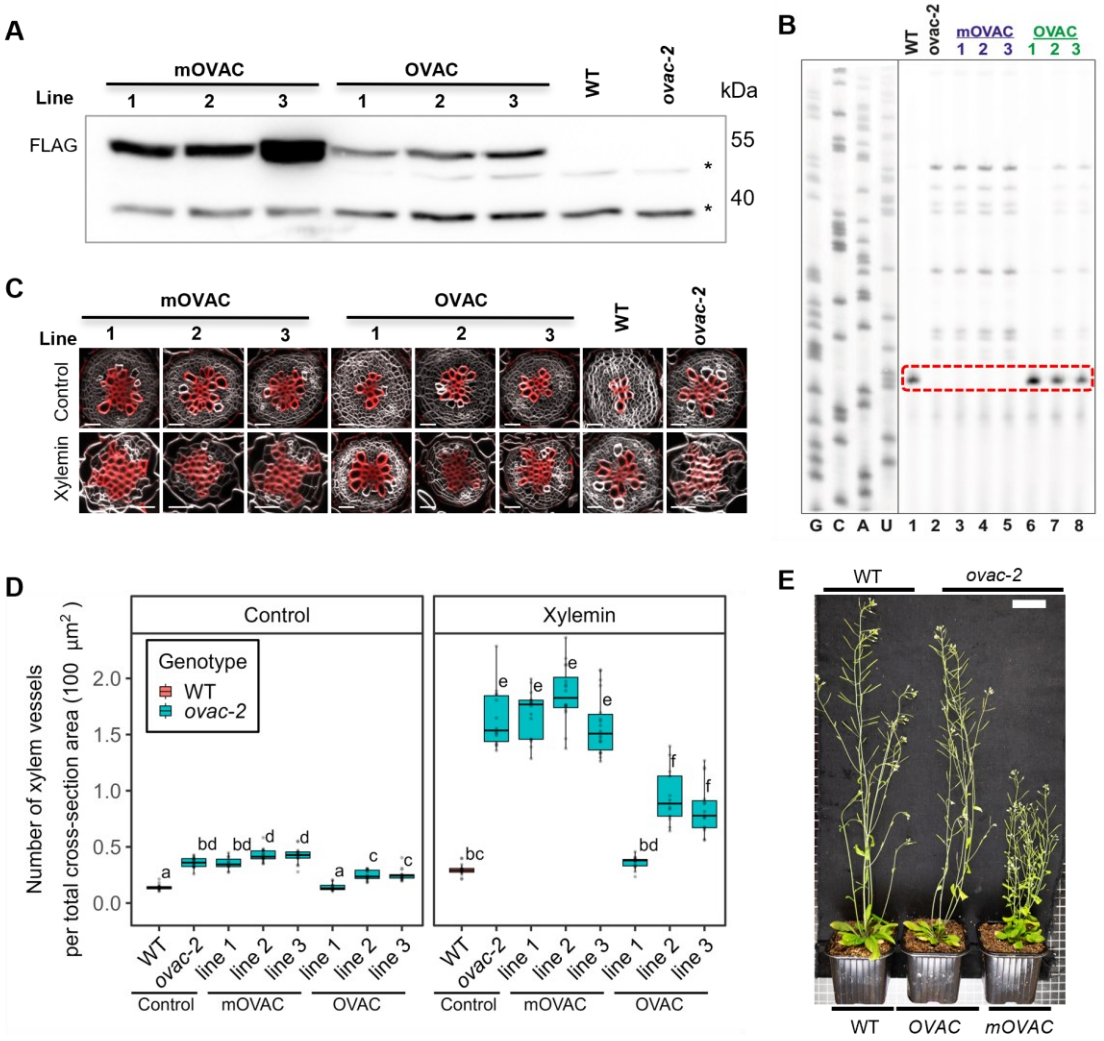


Fig. S4. OVAC methyltransferase activity is required for OVAC function.

(**A**) Immunoblotting against FLAG of total plant root extracts from three independent lines of *ovac-2* expressing catalytically inactive OVAC variant (mOVAC) or wild-type OVAC (OVAC), and from WT and *ovac-2* plants. The asterisks indicate nonspecific bands. (**B**) Primer extension analysis of the m^3U2952 modification from *Arabidopsis* total RNA pools derived from each transgenic line indicated, WT and *ovac-2* plants. The first four lanes are a sequencing ladder. The primer extension stops corresponding to the U2952 (located one nucleotide before the modified nucleotide) is indicated with a red box. (**C**) Representative root cross-sections of 14-day-old each transgenic line indicated, WT and *ovac-2* plants grown on mock or xylemin (50 μM)-containing media. Scale bar, 20 μm. (**D**) The graph quantifies vessel numbers per total cross-section area for WT, *ovac-2*, and independent transgenic lines (n = 11 ~ 18, Wilcoxon rank-sum tests with Bonferroni correction). (**E**) Transgenic *Arabidopsis* harboring the mOVAC gene on the right and wild-type OVAC on the left in *ovac-2* background. (n = 10 ~ 11). Scale bar, 4cm.

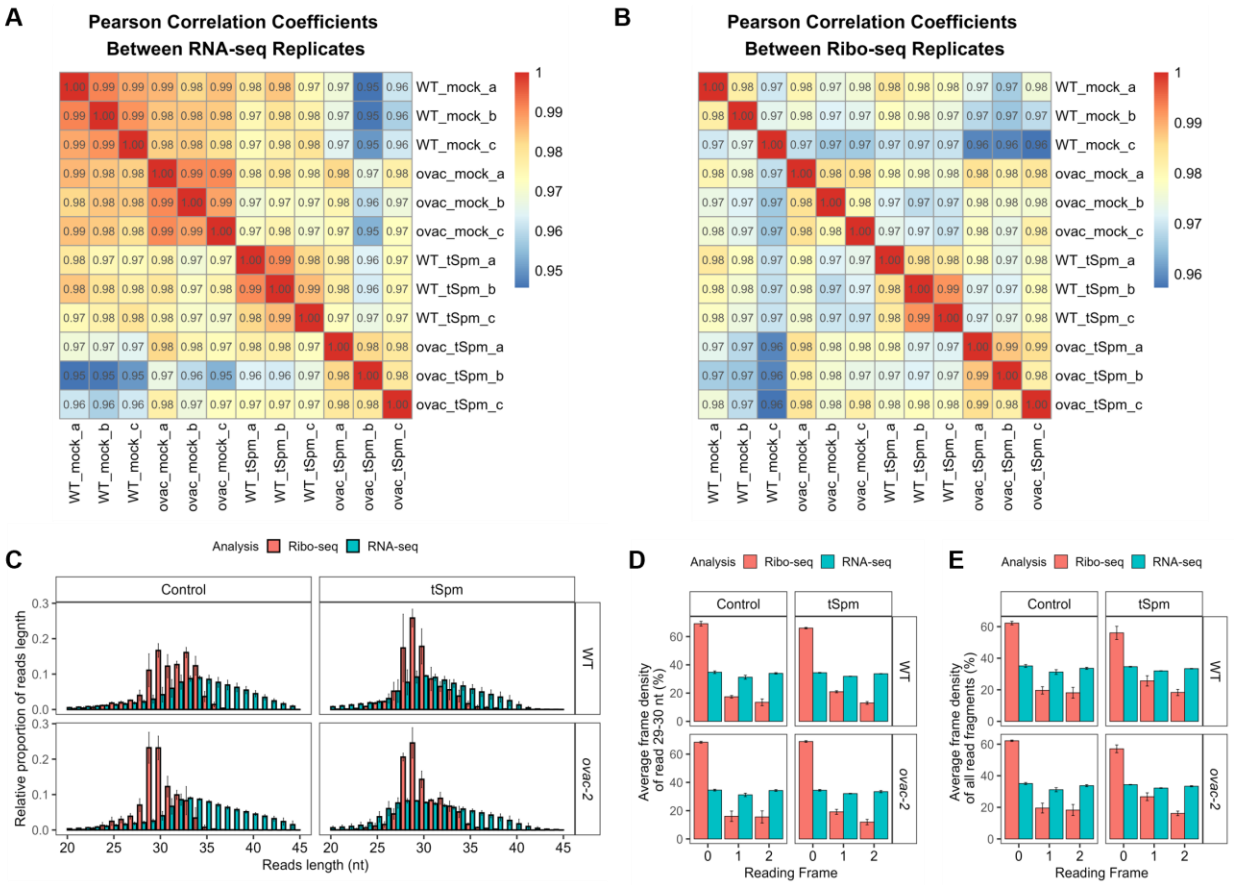


Fig. S5. Quality assessment of RNA-seq and ribosome footprinting (Ribo-seq) datasets.

(**A and B**) Pearson correlation coefficients based on FPKM values among biological replicates of RNA-seq (**A**) and Ribo-seq (**B**) samples. (**C**) Average read length distribution of Ribo-seq and RNA-seq of biological replicates across the indicated genotypes and treatments. (**D** and **E**) Three-nucleotide periodicity of Ribo-seq and RNA-seq reads analyzed with the RibosomeProfilingQC package (*67*), calculated either from reads of length 29-30 nucleotides (**D**) or from all reads (**E**).

A

Comparison	Downregulated genes (LogFC<-0.5)	Upregulated genes (LogFC>0.5)	Non-Significant Genes (FDR >0.05) (%)	Total genes detected	% Regulated genes
ovac-2 mock vs WT mock	15	15	18,992 (99.84 %)	19,022	0.16 %
WT tSpm vs WT mock	179	43	18,615 (98.82 %)	18,837	1.18 %
ovac-2 tSpm vs *ovac-2* mock	60	21	19,058 (99.58 %)	19,139	0.42 %
ovac-2 tSpm vs WT tSpm	13	6	19,133 (99.90 %)	19,152	0.10 %

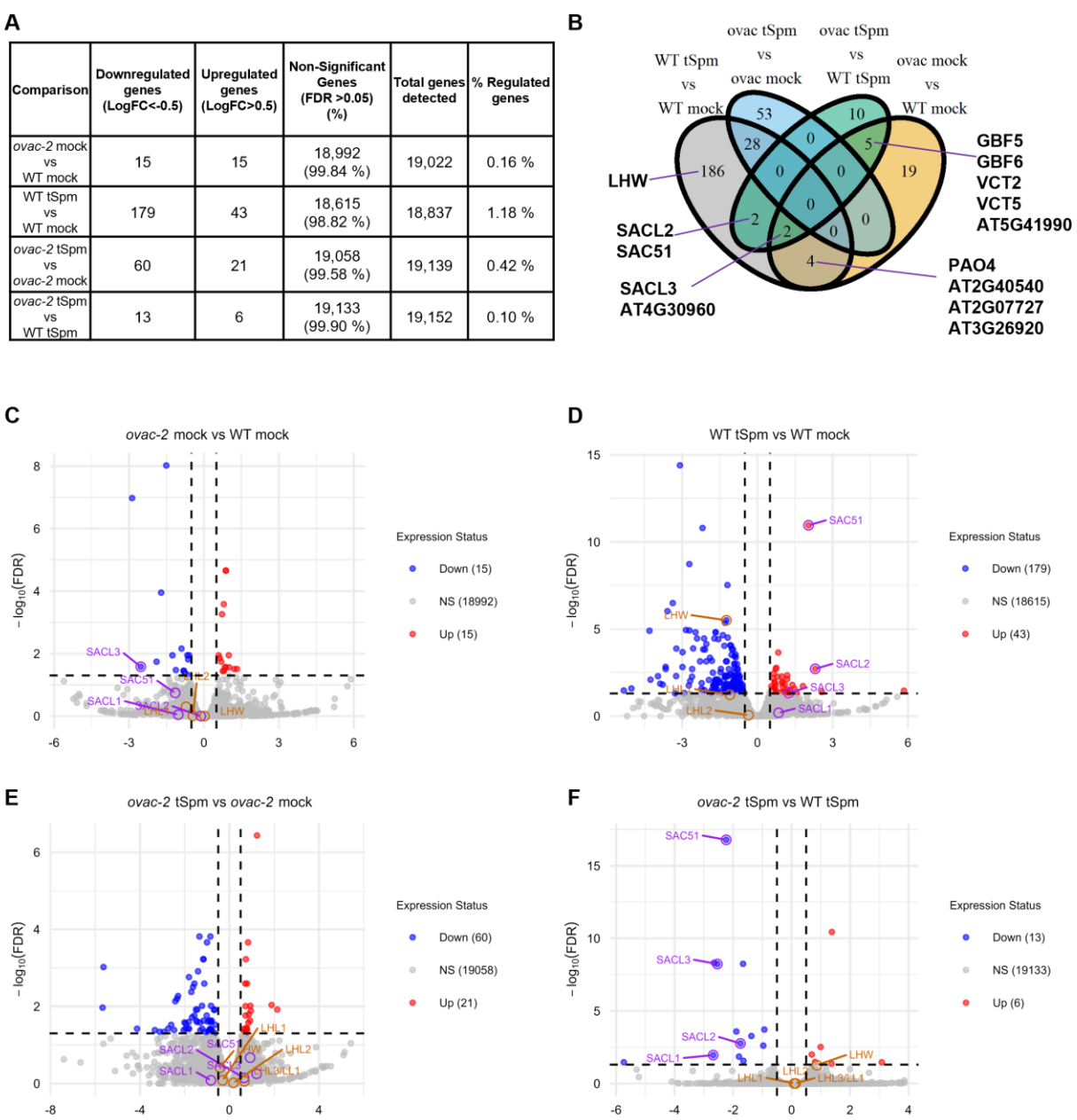


Fig. S6. Summary of differential translation efficiency analysis.

(**A**) Overview of comparisons between the indicated datasets for differential translation efficiency. EdgeR was applied to detect significant changes (FDR < 0.05) in up- or downregulation (|logFC| > 0.5) under each comparison. (**B**) Venn diagram showing significantly regulated genes in translation efficiency from the four comparisons indicated in (**A**). (**C** to **F**) Volcano plots displaying differentially regulated genes in translation for each of the four comparisons. SACLs, LHW, and their paralogs are highlighted.

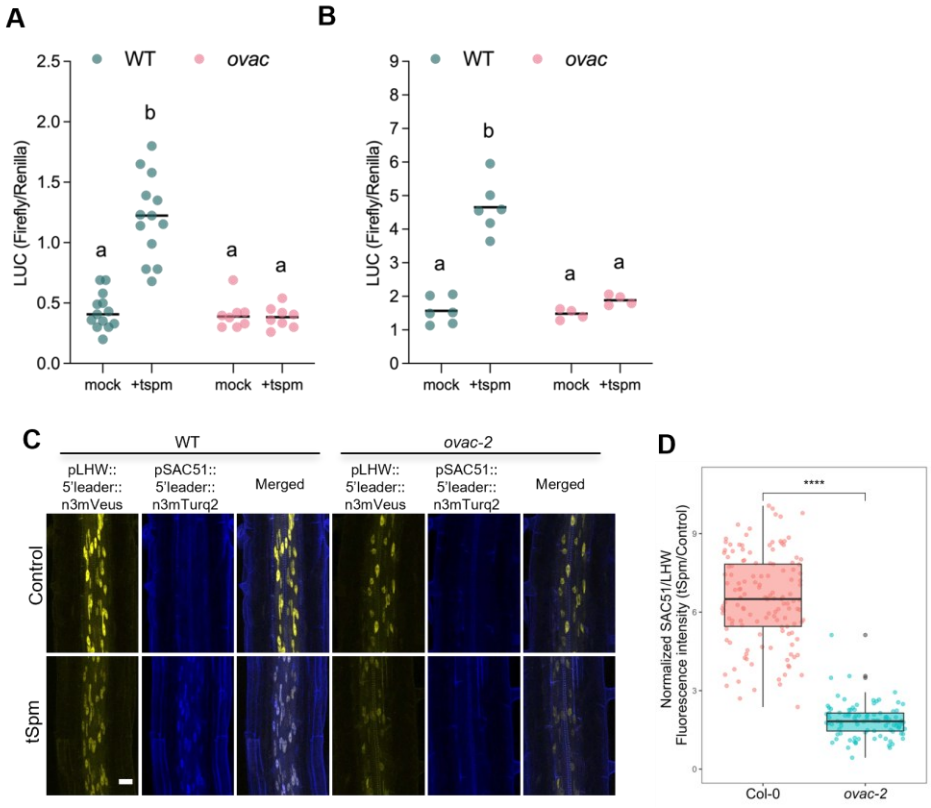


Fig. S7. Enhanced bifunctional translational regulation of thermospermine (tSpm) by m^{3}U2952.

(**A** and **B**) Dual-Luciferase assay in WT and *ovac-2* leaf protoplasts using p*35S*:: *SACL3 uORF*::*F-LUC* (A) or p*35s*::*sacl3-31 uORF*::*F-LUC* (B) (n = 6 -14, one-way ANOVA). (**C**) *LHW* and *SAC51* translational reporters in 8-day-old mature roots from WT and *ovac* with or without 24-hour 50 µM tSpm treatment. (**D**) *SAC51*/LHW fluorescence intensity normalized to mock condition from (C) (*n* = 3 - 4; 76-196 nuclei, Wilcoxon rank-sum test).

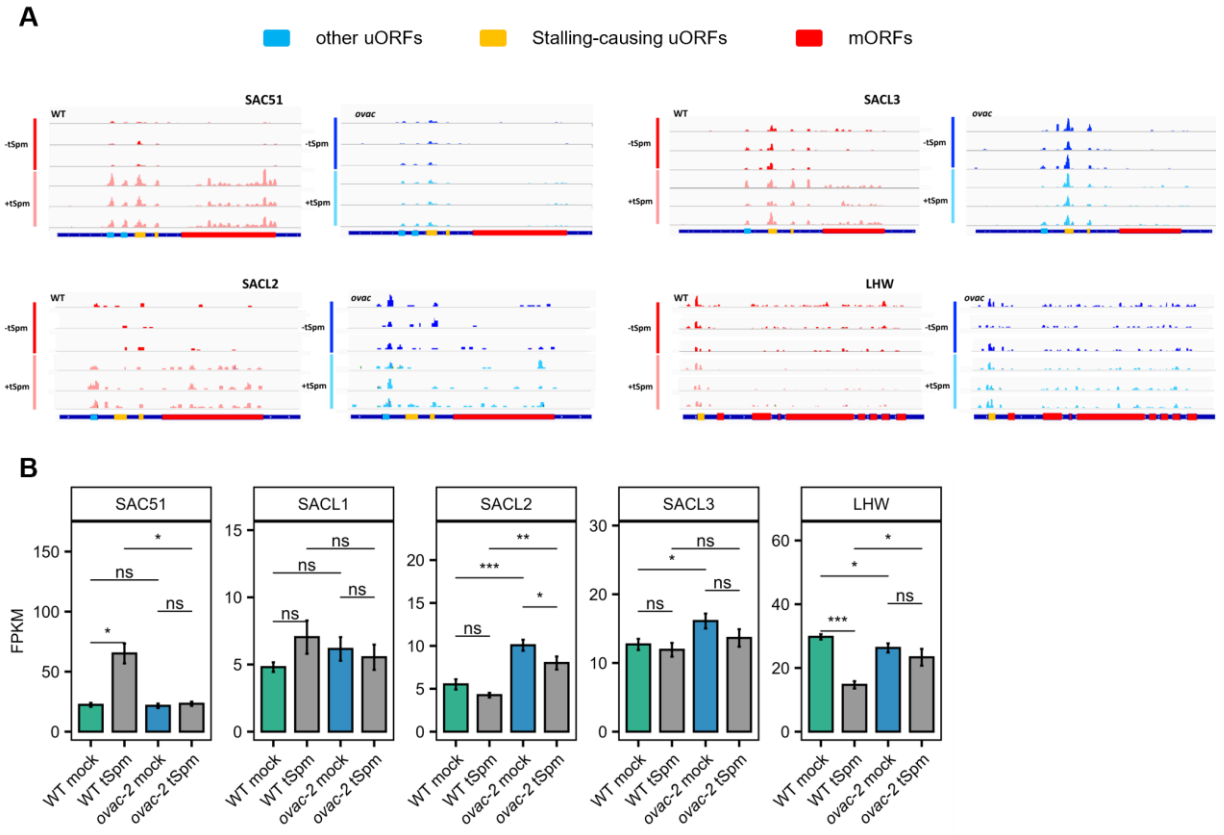


Fig. S8. Ribosome footprinting reads coverage and transcript levels of *SACL*s and *LHW*.
(**A**) Ribosome occupancy on *SAC51, SACL3, SACL2* and *LHW* mRNA. The peaks represent the number of reads/positions visualized with Integrative Genomics Viewer (*113*) (*n* = 3). (**B**) Transcript levels of SACLs and LHW in WT and *ovac-2* with and without 100 µM thermospermine (tSpm) from transcriptome analysis (n = 3). Student's T-test, ns, no significance, * P ≤ 0.05, **P ≤ 0.01, ***P ≤ 0.001.

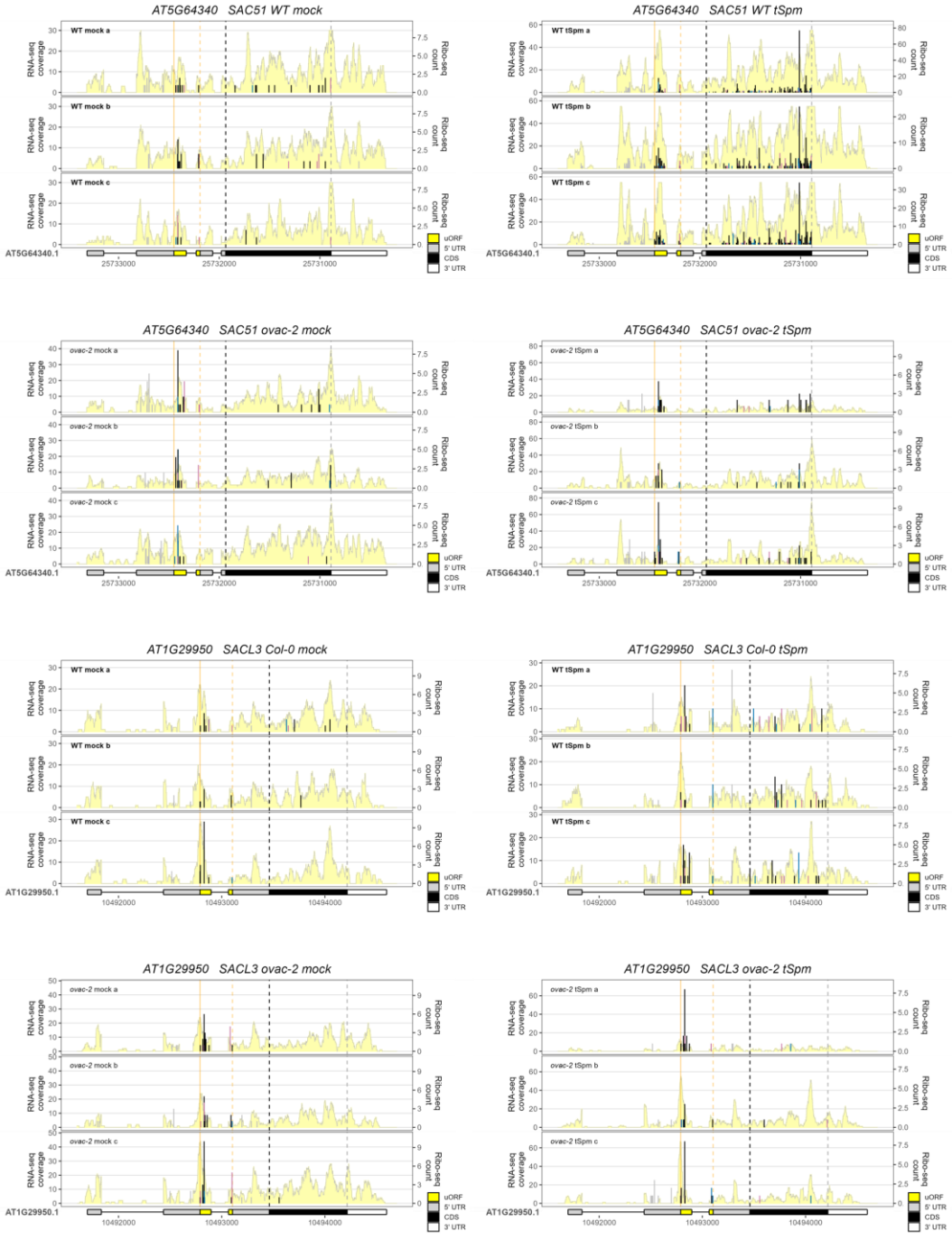


Fig. S9. RNA-seq and ribosome footprinting profiles of *SAC51* and *SACL3* in WT and *ovac-2* with or without thermospermine (tSpm) treatment.

RNA-seq coverage is shown with a light-yellow background. Ribosome footprinting reads are plotted with their first nucleotide aligned to the predicted P-site and are color-coded according to reading frame: black (first/expected frame), magenta (second frame), and blue (third frame). Plots were generated using the ggRibo (*114*).

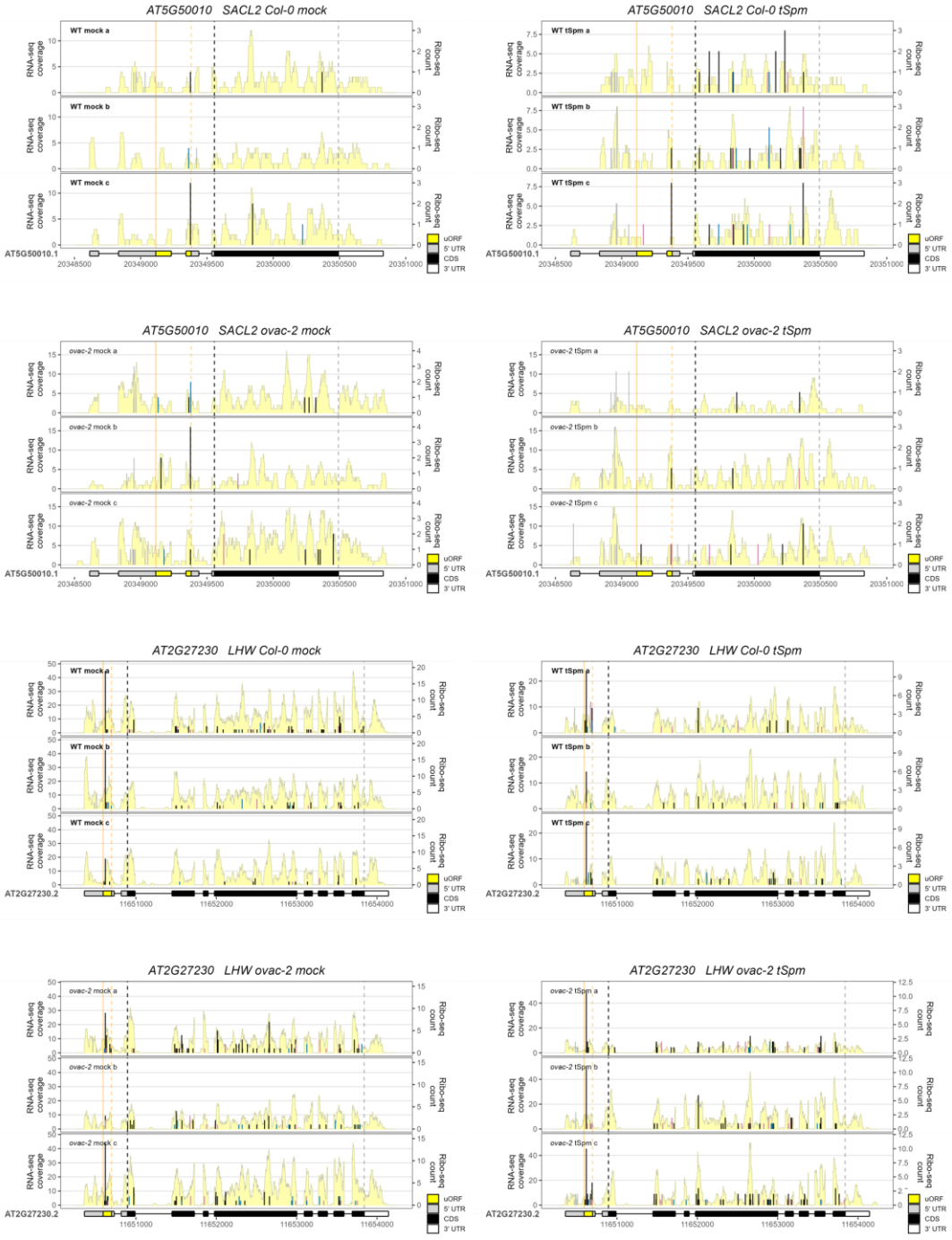
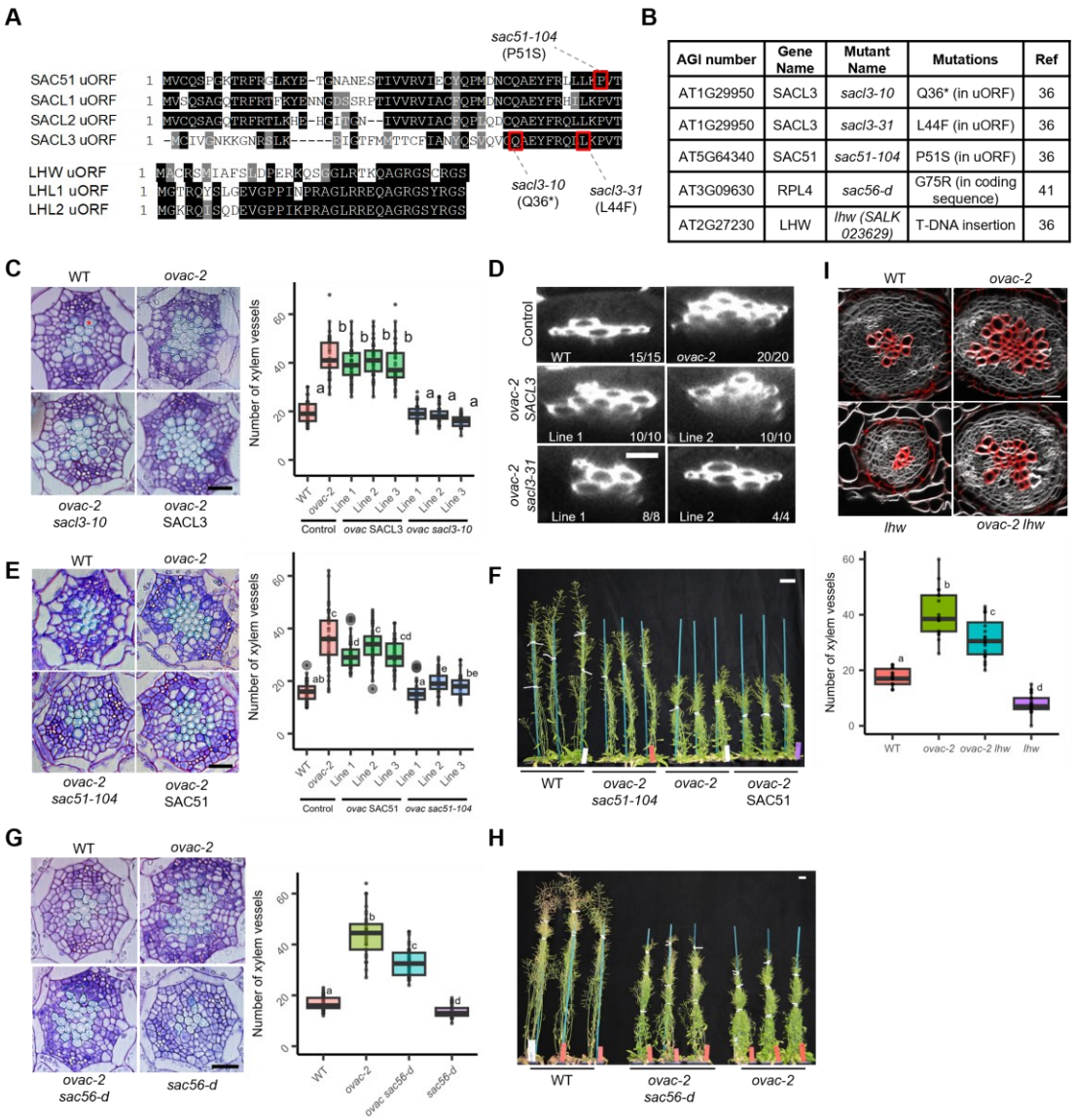


Fig. S10. RNA-seq and ribosome footprinting profiles of *SACL2* and *LHW* in WT and *ovac-2* with or without thermospermine (tSpm) treatment.

RNA-seq coverage is shown with a light-yellow background. Ribosome footprinting reads are plotted with their first nucleotide aligned to the predicted P-site and are color-coded according to reading frame: black (first/expected frame), magenta (second frame), and blue (third frame). Plots were generated using the ggRibo (*114*).



AGI number	Gene Name	Mutant Name	Mutations	Ref
AT1G29950	SACL3	*sacl3-10*	Q36* (in uORF)	36
AT1G29950	SACL3	*sacl3-31*	L44F (in uORF)	36
AT5G64340	SAC51	*sac51-104*	P51S (in uORF)	36
AT3G09630	RPL4	*sac56-d*	G75R (in coding sequence)	41
AT2G27230	LHW	*lhw (SALK 023629)*	T-DNA insertion	36

Fig. S11. Phenotypic recovery of *ovac*.

(**A**) Amino acid alignment of uORFs from SACLs, LHW, and LHW paralogs, with conserved residues highlighted and the mutations indicated. (**B**) Overview of mutants introduced to *ovac-2*. (**C** and **E**) Hypocotyl cross-sections (left) of 10-day-old WT, *ovac-2*, and *ovac-2* expressing the indicated transgenes. Graph (right) quantifies vessel numbers in the cross-sections (n = 35 ~ 54). (**D**) Confocal images of hypocotyl/root junctions from the indicated plants. Frequencies of observed phenotypes are shown (bottom-right corner). (**F**) Images of 58-day-old plants (n = 3 per 3 lines of *ovac-2 SAC51* and *ovac-2 sac51-104*). (**G** and **I**) Hypocotyl cross-sections of 10-day-old (G) or 14-day-old (I) indicated genotypes. The graph (right (G) or bottom (I)) shows vessel numbers (n = 34 ~ 42 for G, n =18 ~ 25 for I). (**H**) Images of 50-day-old plants (n = 12 for *ovac-2 sac56-d* and *ovac-2*). Scale bar, 4 cm (F and H) and 20 μm (C to E, G and I); toluidine blue (C, E, G), Fuchsin staining (D), or Fuchsin staining and SR2200 (I). one-way ANOVA with Tukey's test (C and I) or Wilcoxon rank-sum tests with Bonferroni correction (E and G).

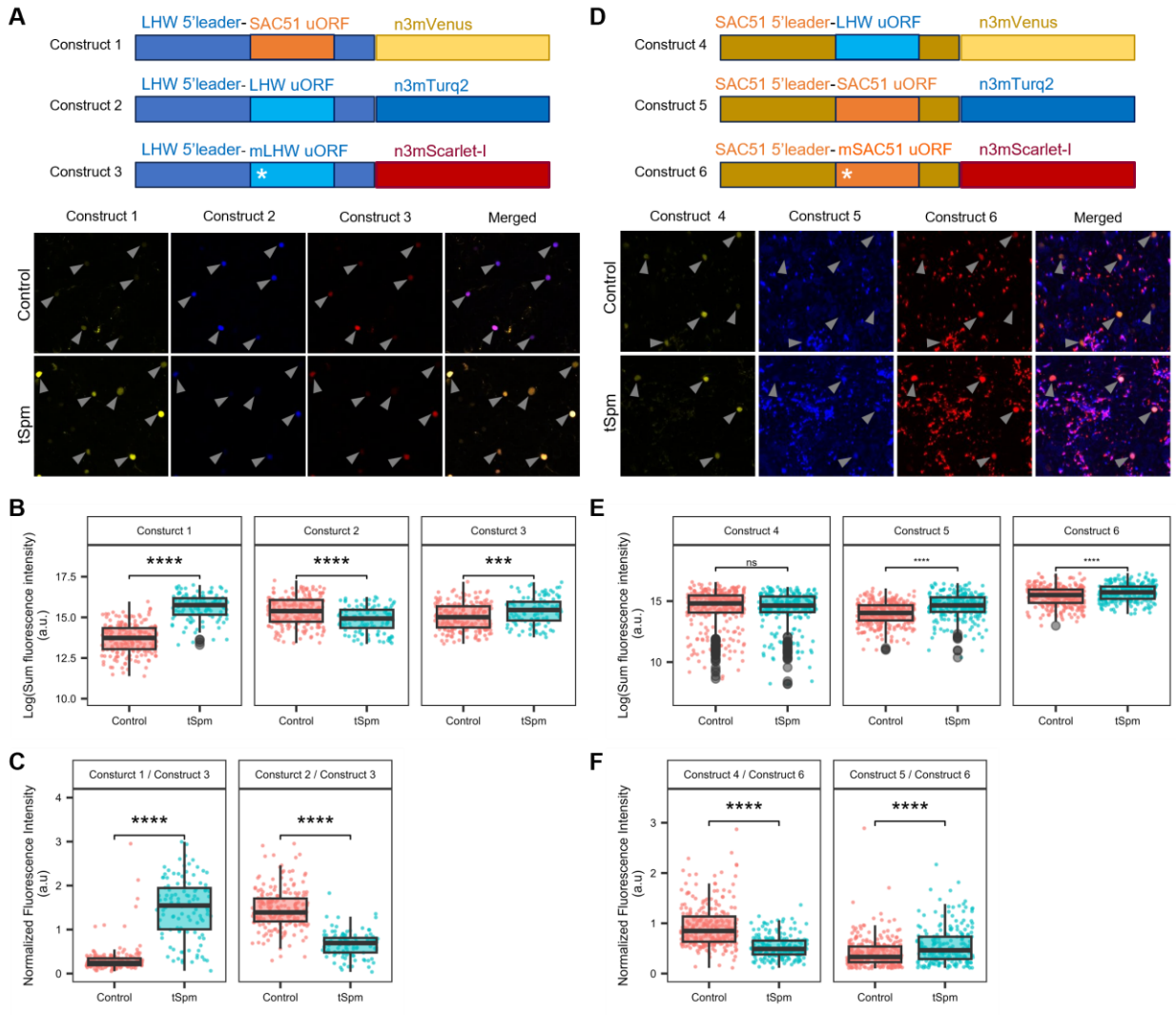


Fig. S12. Conserved uORF peptides of *SACL* and *LHW*-mediated thermospermine-dependent translational regulation.

(**A**) Tobacco leaves transiently expressing translational reporters (*LHW* 5′leader with *SAC51* [construct 1] or *LHW* uORF [construct 2]) and a transcriptional reporter (*LHW* 5′leader with mutated (m*LHW*) uORF [construct 3]), treated with or without tSpm. (**B**) Quantification of each reporter fluorescence. (**C**) normalization to the transcriptional reporter (n = 5, 116 ~ 203 nuclei, Student's t-test). (**D**) Tobacco leaves transiently expressing translational reporters (*SAC51* 5'leader with *LHW* [construct 4] or *SAC51* uORF [construct 5]), and transcriptional reporter (*SAC51* 5'leader with mutated (m*SAC51*) uORF [construct 6]), treated with or without tSpm. (**E**) Quantification of reporter fluorescence. (**F**) Normalization to the transcriptional reporter (n = 7 ~ 8, 250 ~ 325 nuclei, Student's t-test). A white asterisk indicates a stop codon introduced by substituting the start codon of each uORF.

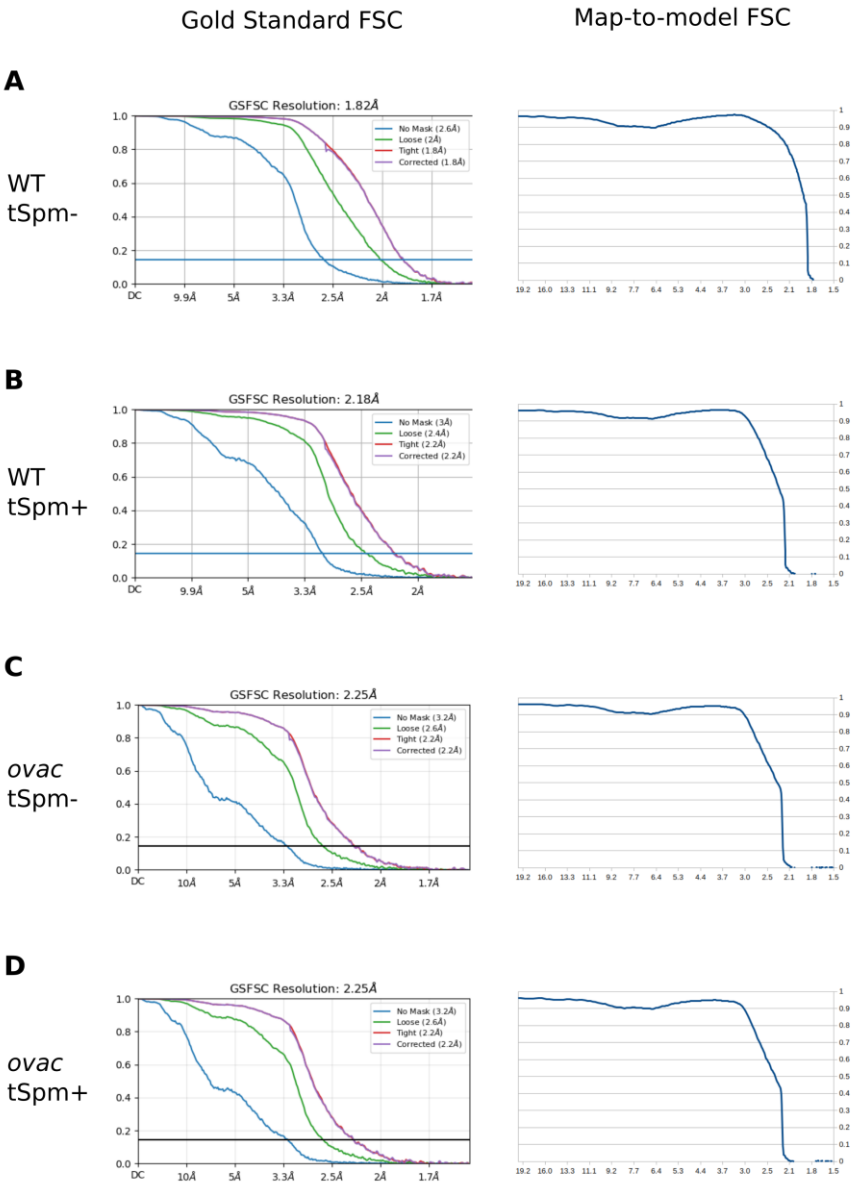


Fig. S13. Fourier Shell Correlation curves of cryo-EM reconstructions.

(**A** to **D**) Gold standard half-map Fourier Shell Correlation (FSC, left panel) as generated in cryoSPARC and map-to-model FSC (right panel) as generated by Refmac at the final structure refinement are shown for datasets of WT or *ovac* without (tSpm-) or with thermospermine (tSpm+): (**A**) WT (tSpm-), (**B**) WT tSpm+, (**C**) *ovac* tSpm-, and (**D**) *ovac* tSpm+.

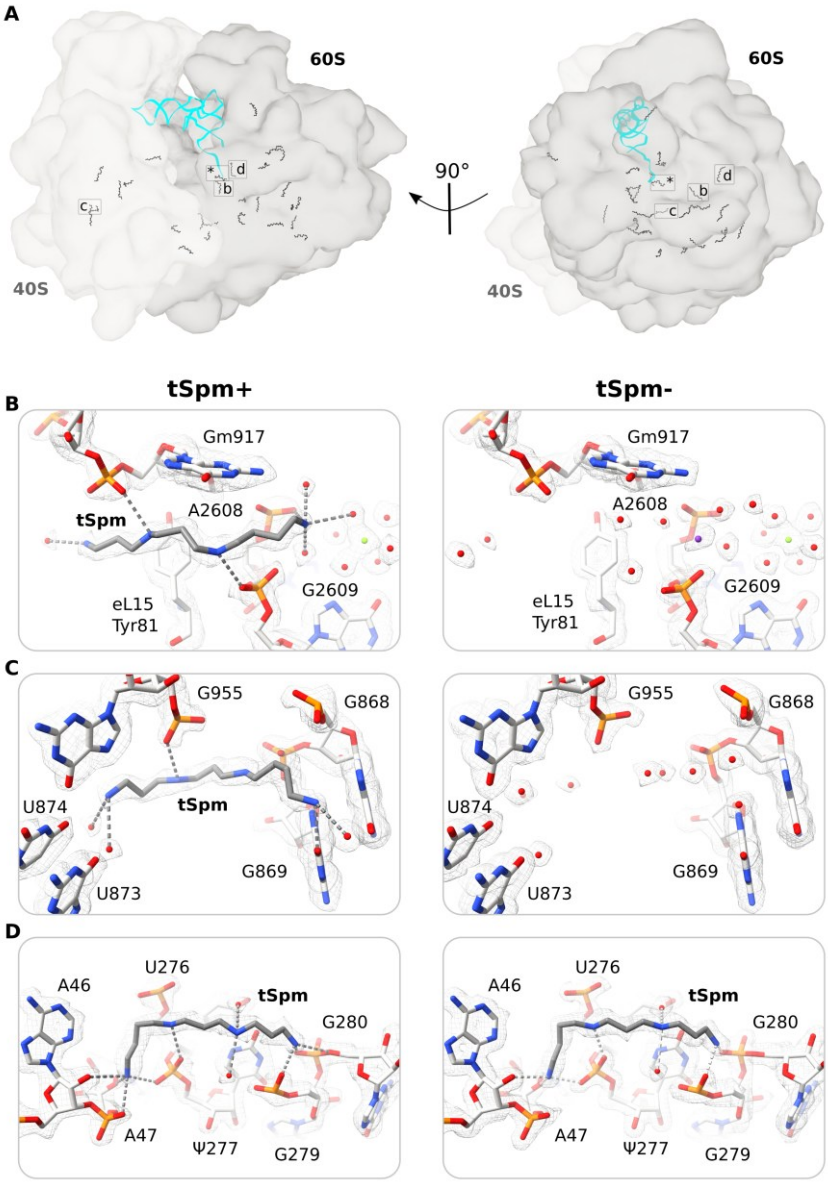


Fig. S14. Thermospermine (tSpm) binding sites in the WT *Arabidopsis* ribosome.

(**A**) Localization of all 27 putative tSpm binding sites found in the WT tSpm+ ribosome sample. Labeled molecules are represented in corresponding figure panels. The tSpm molecule marked by an asterisk '*' is also shown in Fig. 3 and Fig. S15A. (**B** to **D**) Example views of tSpm binding sites in the tSpm+ sample (left panel) compared to tSpm- sample (right panel). 'd' was the only tSpm molecule found in both WT tSpm- and tSpm+ samples.

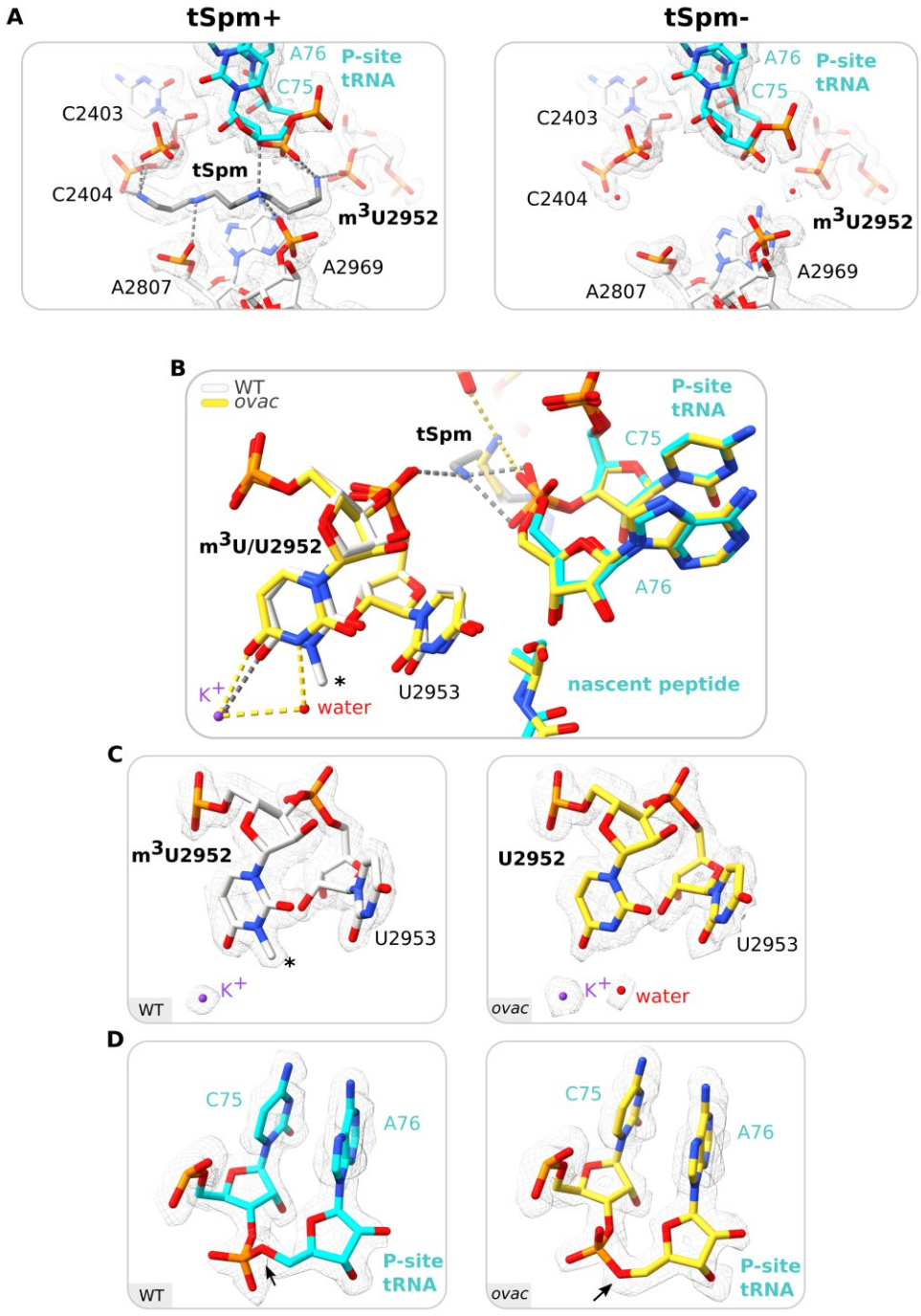


Fig. S15. Thermospermine (tSpm) binding site in WT and *ovac* mutant *Arabidopsis* ribosomes.

(**A**) tSpm binding site in the peptidyl transferase center; labelled '*' in Fig. S14A and also shown in Fig. 3. (**B**) Superimposition of tSpm-bound WT (grey/cyan) and *ovac* (yellow) *Arabidopsis* ribosome structures showing different binding modes for tSpm and conformational change of U2952-U2953 residues. * indicates methyl group of m³U2952. (**C**) Close-up view of U2952 and U2953 in WT (left panel) and *ovac* (right panel) ribosomes. Cryo-EM maps, grey mesh; K^+ ion, purple; water molecule, red. (**D**) Conformation of phosphate group linking P-site tRNA residues C75 to A76 (pointed with arrow) in WT (left panel) and *ovac* mutant (right panel) ribosomes.

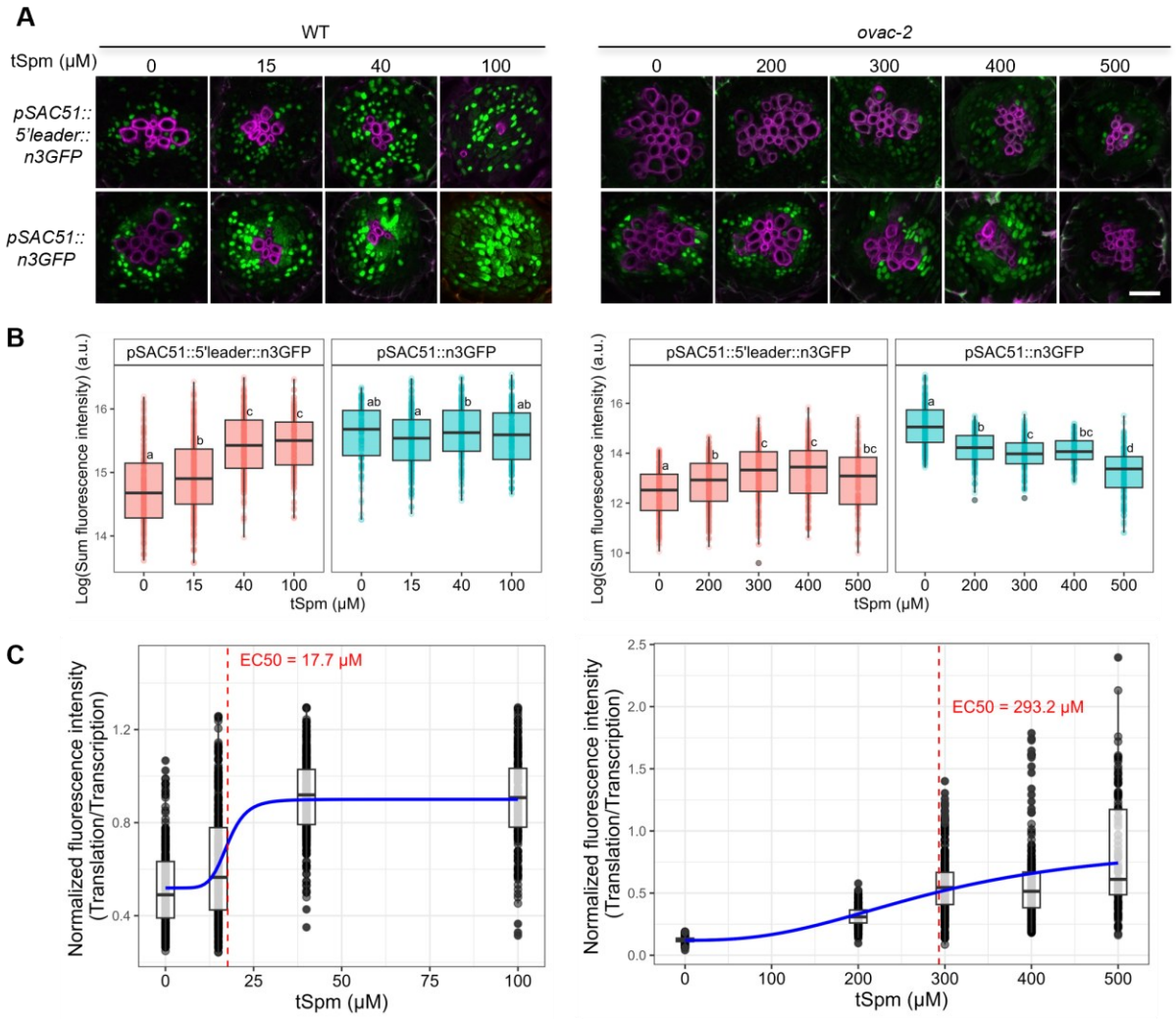


Fig. S16. Increased half-maximal excitation concentration (EC_{50}) for SAC51 translation in *ovac* compared to WT.

(**A**) Maximal z-projected confocal image of *SAC51* translational (top) and transcriptional (bottom) reporters in cross-sections of 14-day-old WT (left) and *ovac* (right) roots grown on the media containing the indicated thermospermine (tSpm) concentrations (μM). Scale bar, 20 μm. (**B**) Quantification of fluorescence intensity of *SAC51* translational or transcriptional reporter of WT (left) and *ovac* (right) from (A) (n =10 ~ 18, one-way ANOVA with Tukey's test). (**C**) Translational reporter fluorescence normalized to the mean of corresponding transcriptional reporter, with EC_{50} values estimated for WT (left) and *ovac* (right).

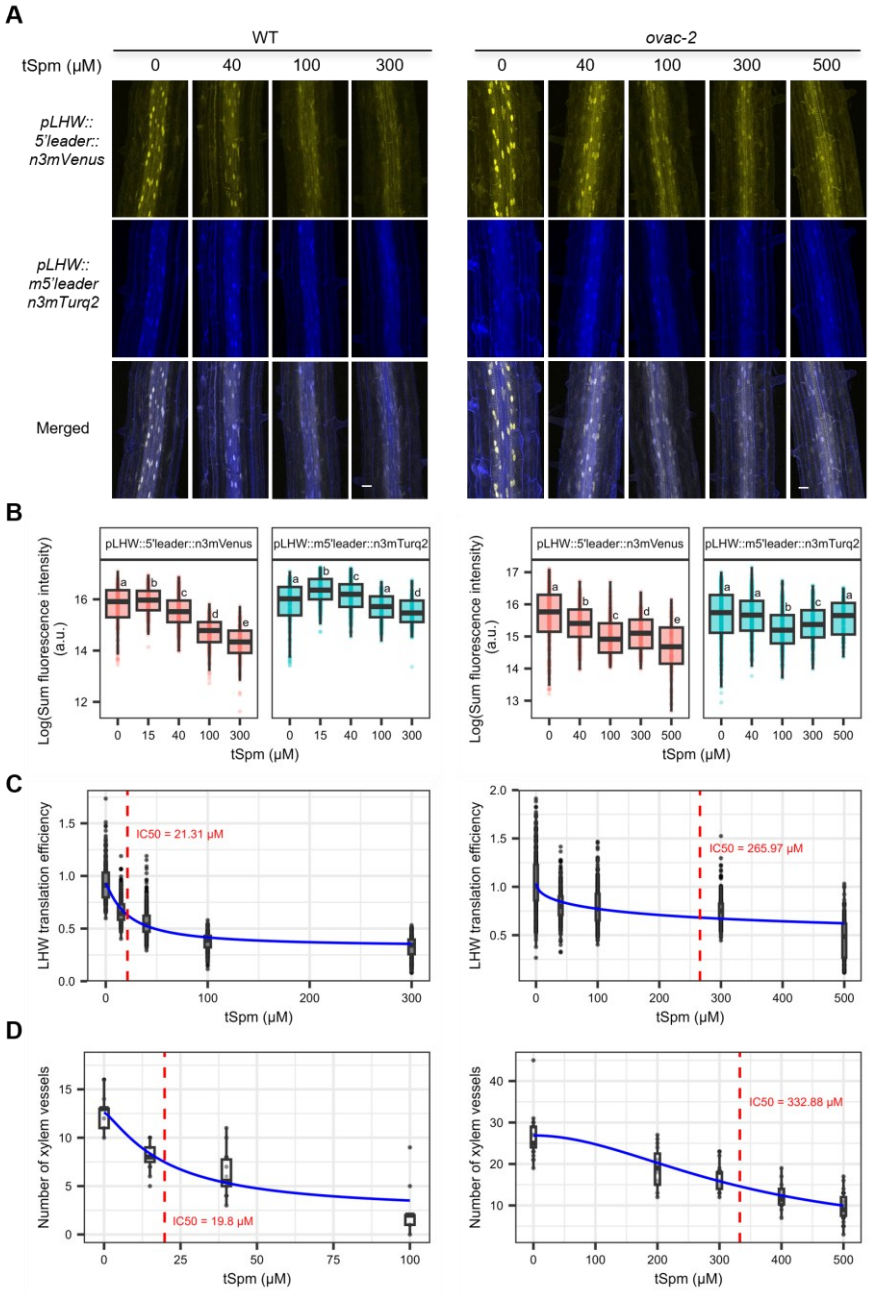


Fig. S17. Increased half-maximal inhibitory concentration (IC_{50}) for LHW translation and vessel differentiation in *ovac* compared to wild type.

(**A**) Maximal z-projected confocal image of *LHW* translational (top) and transcriptional (bottom) reporters in mature roots of 8-day-old WT (left) and *ovac* (right) treated with the indicated thermospermine (tSpm) concentrations (μM) for 24 hours. Scale bar, 20 μm. (**B**) Quantification of fluorescence intensity of *LHW* translational or transcriptional reporter of WT (left) and *ovac* (right) from (A) (n = 3 ~ 9, one-way ANOVA with Tukey's test). (**C**) Translational reporter fluorescence normalized to the corresponding transcriptional reporter, with IC_{50} values estimated for WT (left) and *ovac* (right). (n = 3 ~ 9). (**D**) Number of xylem vessels in root cross-sections from fig. S16A at the indicated tSpm concentrations, with IC_{50} values estimated for WT (left) and *ovac* (right) (n = 12 ~ 31).

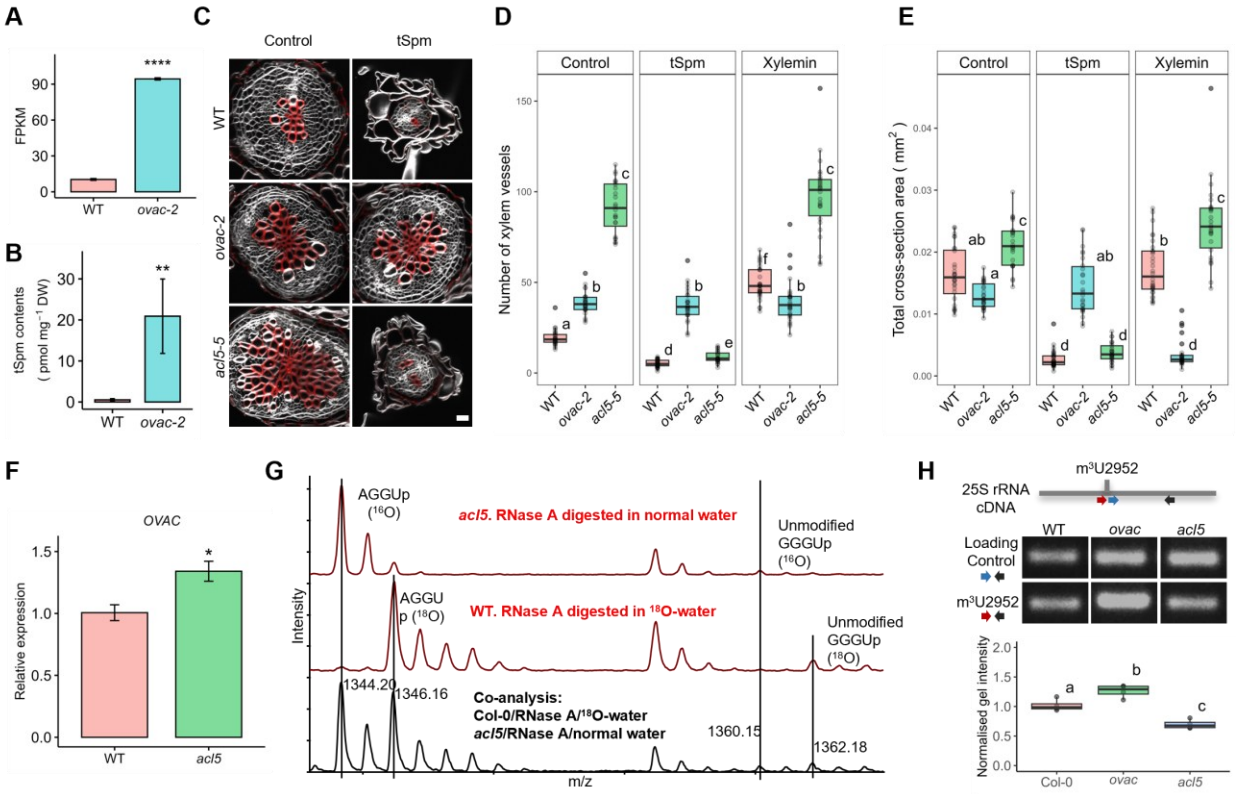


Fig. S18. Hyper-sensitivity of *ovac* to xylemin but not to thermospermine (tSpm).

(**A**) Transcript level of *ACL5* in 12-day-old seedlings of genotypes indicated. (**B**) Quantification of tSpm in 21-day-old roots of WT and *ovac-2* (n = 3, Wilcoxon rank-sum test). (**C**) Transverse sections of roots grown on media with or without 50 µM tSpm for 14 days (n = 24 ~ 33). Note that the controls are the same as those in Fig. 4A. Scale bar, 20 µm. (**D** and **E**) The number of xylem vessels and vascular area in the cross-sections shown in (C) (n = 24 ~ 33, Wilcoxon rank sum test with Bonferroni correction). (**F**) Transcript level of *OVAC* in 12-day-old seedlings of genotypes indicated. (**G**) m^3U2952 quantification in WT and *acl5* rRNA roots by Mass spectrometric analysis. (**H**) A schematic of the primers used to detect m^3U2952 (blue arrow, forward primer for loading control; red arrow, forward primer for m^3U2952 detection; black arrow, reverse primer). Gel images for the loading control and m^3U2952 detection, and normalized m^3U2952 band intensity relative to the loading control (n = 4, one-way ANOVA with Tukey's test). Error bars, means ± SE (n = 4, Student's T-test) in A and F.

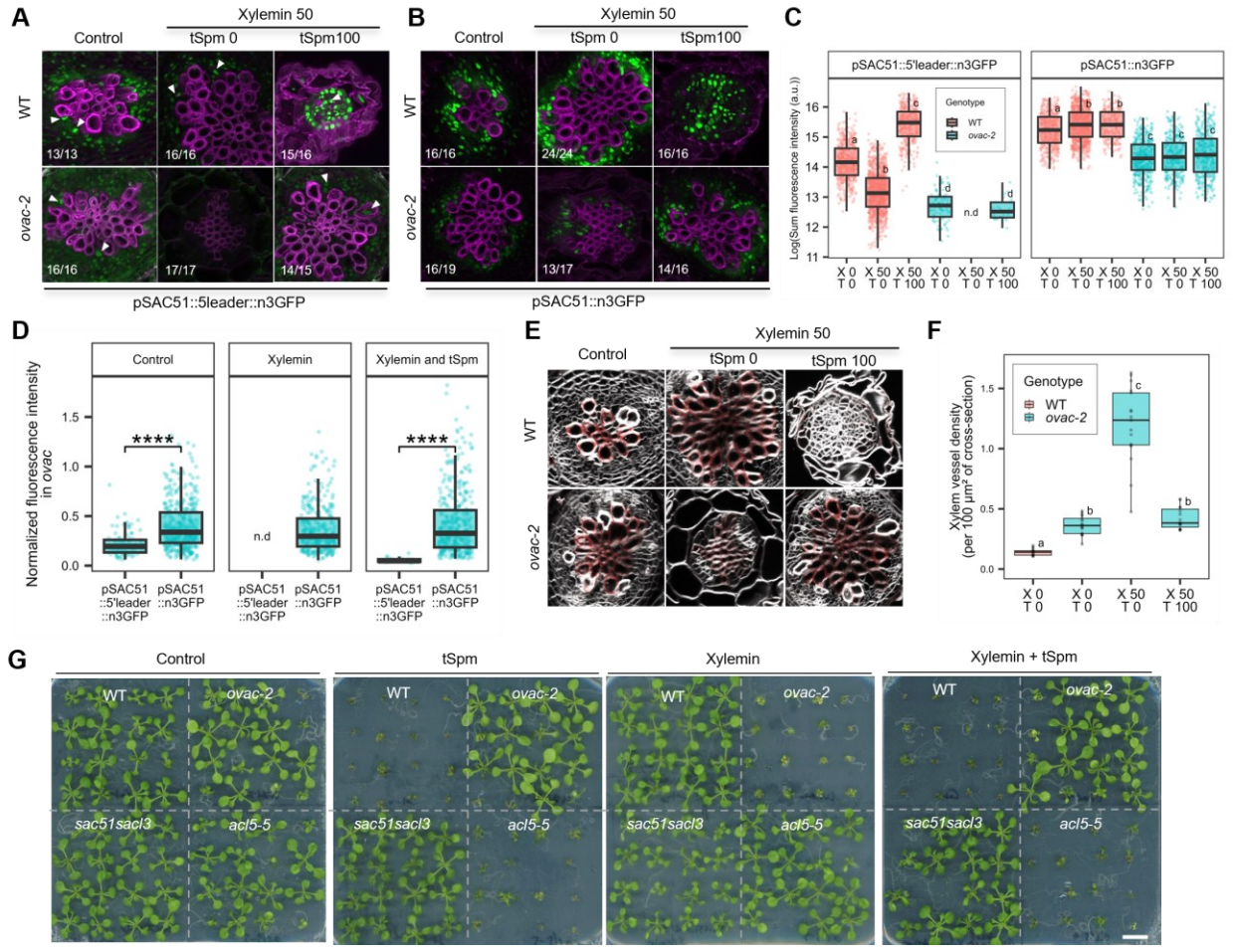


Fig. S19. Reduced *SAC51* translation in *ovac*.

(**A** and **B**) Maximal z-projected confocal image of *SAC51* translational (A) and transcriptional (B) reporters in cross-sections of WT and *ovac* roots grown on the media indicated for 14 days. White arrowheads highlight representative reporter expression in xylem cells. (**C**) Quantification of fluorescence intensity from (A and B) (n = 13~19, Wilcoxon rank sum test with Bonferroni correction). (**D**) Normalized fluorescence intensity of *SAC51* translational and transcriptional reporters in *ovac* by means of corresponding wild type in each condition shown in (C) (n = 13~19, Wilcoxon rank sum test with Bonferroni correction). (**E**) Representative cross-sections of roots of WT and *ovac-2* plants grown on media indicated for 14 days. (**F**) Quantification of xylem vessels per total vascular area. (n = 13~17, Wilcoxon rank sum test with Bonferroni correction). (**G**) Seedlings grown on media indicated for 14 days. 0, no treatment; 50, 50 µM; 100, 100 µM, Scale bar, 20 µm (A, B, and E), 1 cm (G). Numbers indicate phenotype frequency.

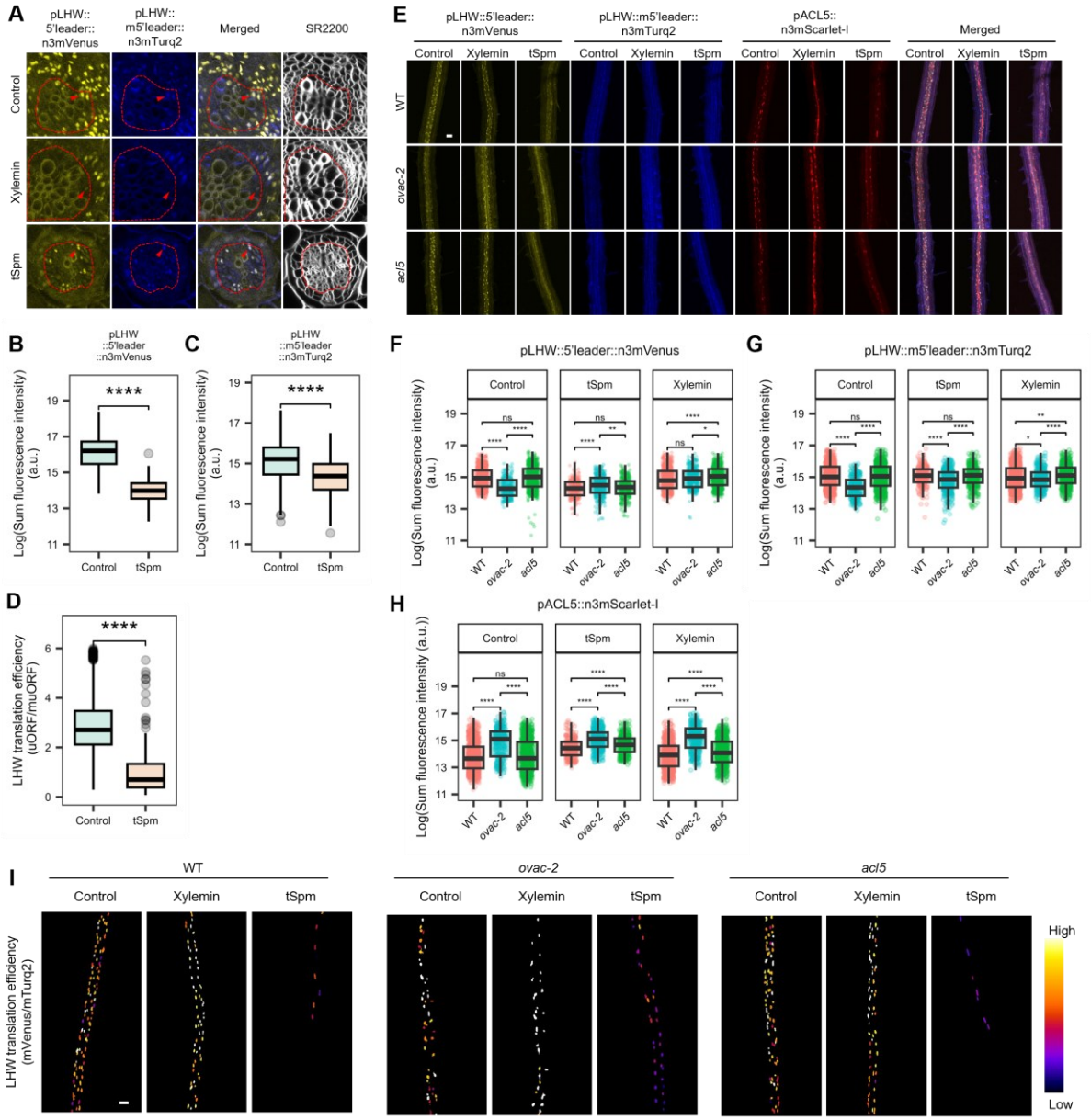


Fig. S20. Translational inhibition of *LHW* by thermospermine (tSpm) and m^{3}U2952.

(**A**) Confocal images of *LHW* translational and transcriptional reporters in transverse sections of wild-type roots grown on the media indicated for 14 days. The region within the red dotted lines marks the xylem tissue. Red arrowheads highlight representative nuclear expression of the reporters. (**B** to **D**) Quantification of *LHW* translational and transcriptional reporter expression and *LHW* translation efficiency from (A). Xylemin-treated samples are excluded due to low reporter transcription in xylem tissue. (**E**) Confocal images of *LHW* translational and transcriptional reporters, as well as the *ACL5* transcriptional reporter, in mature roots following 24-hour treatment with 50 µM tSpm or 50 µM xylemin. (**F** to **H**) Quantification of fluorescence intensity for the reporters in (E). (I) Look-Up-Table representation of *LHW* translation efficiency based on the images in (E).

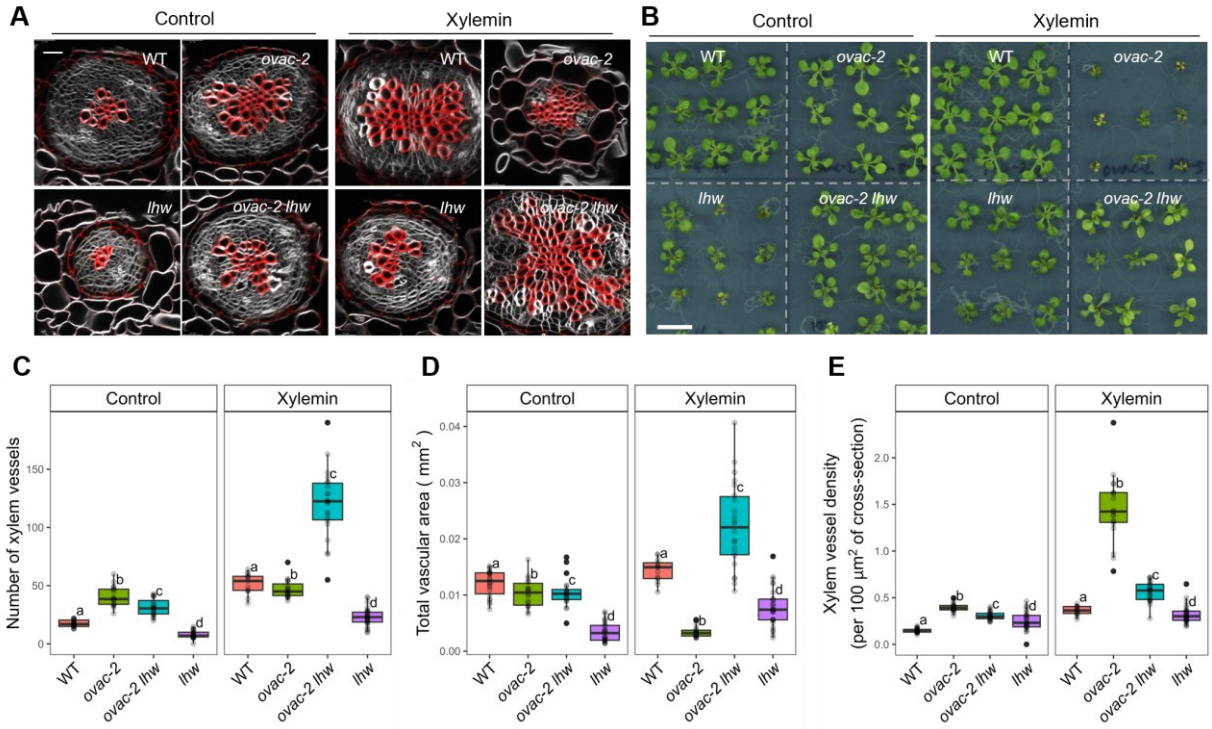


Fig. S21. Phenotypic recovery of xylemin-treated *ovac* by loss-of-function of *lhw*.

(**A**) Representative transverse sections of roots of WT, *ovac-2, lhw,* and *ovac-2 lhw* grown on media with mock or 50 µM xylemin for 14 days. Note that the control is the same as in Fig. S11l. Scale bar, 20 µm. (**B**) Images of seedlings shown in (A). Scale bar, 1 cm. (**C** to **E**) Quantification of the number of xylem vessels (**C**), vascular area (**D**), and the number of xylem vessels per vascular area (**E**) from (A). Statistical significance among genotypes in mock or xylemin-treated condition was determined using one-way ANOVA with Tukey's test (n =18 ~ 28).

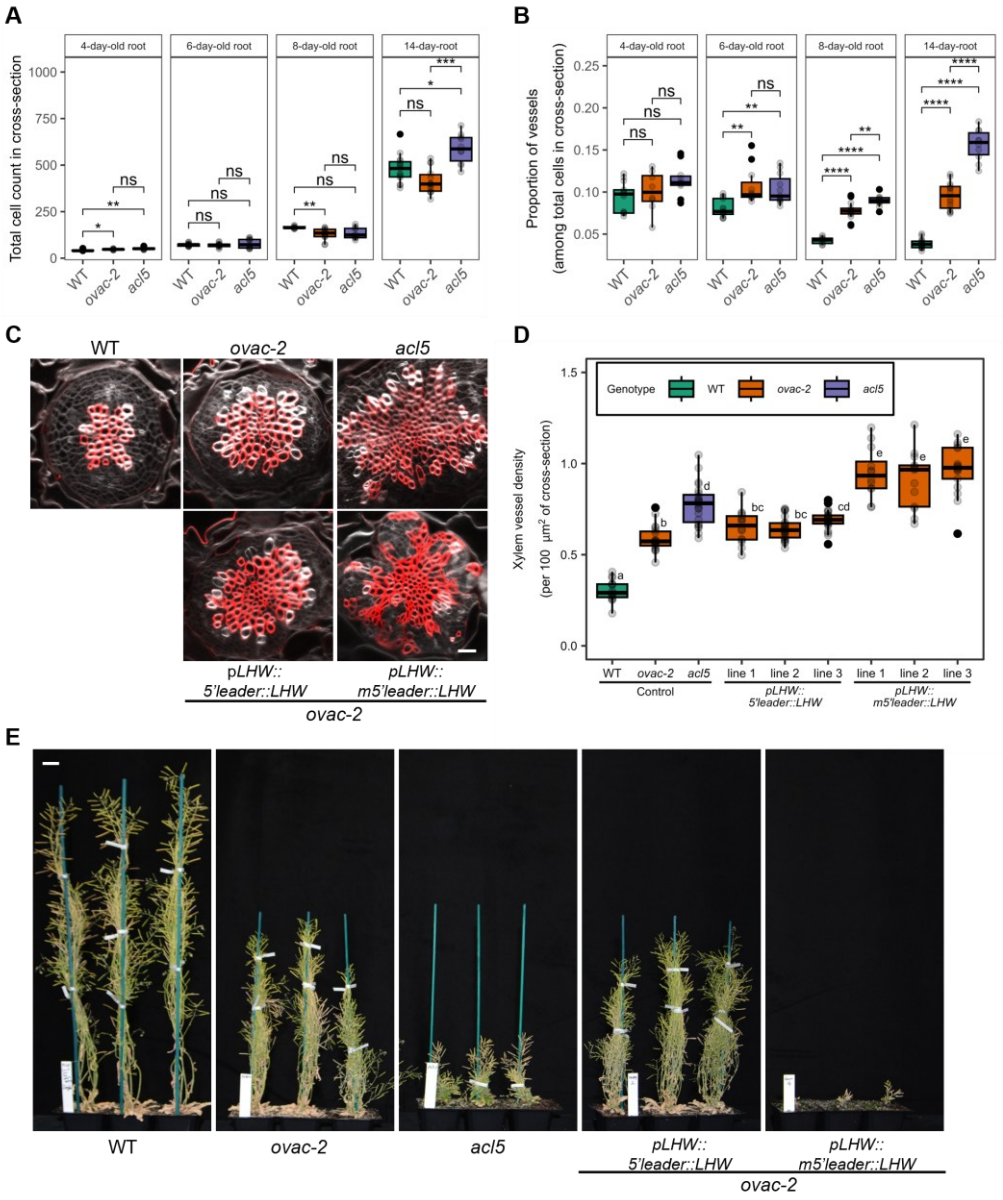


Fig. S22. Enhanced vessel differentiation by elevated LHW translation in *ovac*.

(**A**) A total number of cells in root cross-sections and (**B**) proportion of vessels among total number of cells from each genotype and developmental stage indicated. The same cross-sections in Fig. 1C and 4A were used for this quantification (n = 8 ~ 15, Wilcoxon rank-sum test for A, Student's t-test for B). (**C**) Representative confocal images of hypocotyl cross-sections (left) from 14-day-old C WT, *acl5*, *ovac-2*, and *ovac-2* expressing either p*LHW*::*5'leader*::*LHW* or p*LHW*::mutated *5'leader* (*m5'leader*)::*LHW*. Scale bar, 20 μm. (**D**) The graph (right) quantifies vessel numbers per total vascular area shown in (C) (n = 12 ~ 24, one-way ANOVA with Tukey's test). (**E**) Representative images of 42-day-old plants (n = 3). Scale bar, 2 cm.

Supplementary Data

Data S1. *Arabidopsis* 25S rRNA modifications identified in the current work, and their corresponding residues (modified or non-modified) in tomato (*27*), tobacco (*28*), human (*1*), fruit fly(*30*, *115*) and yeast (*2*). For the *Arabidopsis* residues, the levels of modification are indicated as percentages.

Data S2. Observed (MZ, obs.) versus expected theoretical (MZ, expt.) m/z-values of RNase A digested 25S rRNA sub-fragments prepared

Data S3. Polysome proteomics of *ovac-2* compared to wild type

Data S4. List of genes showing altered translation efficiency in comparison between *ovac-2* and Col-0. The translation of 15 genes is significantly upregulated and of 15 genes downregulated (EdgeR, FDR < 0.5, |logFC| >0.5)

Data S5. List of genes showing altered translation efficiency in wild type upon thermospermine treatment. The translation of 43 genes is significantly upregulated by thermospermine and of 179 genes is downregulated (EdgeR, FDR < 0.5, |logFC| >0.5)

Data S6. List of genes showing altered translation efficiency in comparison between tSpm-treated *ovac* vs mock-treated *ovac*. The translation of 21 genes is significantly upregulated by thermospermine and of 60 genes is downregulated (EdgeR, FDR < 0.5, |logFC| >0.5)

Data S7. List of genes showing altered translation efficiency in comparison between tSpm-treated *ovac* vs tSpm-treated wild type. The translation of 6 genes is significantly upregulated and of 13 genes is downregulated (EdgeR, FDR < 0.5, |logFC| >0.5)

Data S8. uORF-containing 26 genes showing altered translation efficiency in wild type but not in *ovac-2* following thermospermine treatment (EdgeR)

Data S9. Cryo-EM data collection and processing

Data S10. Plant materials used in this study

Data S11. Primers used in this study